NUMERICAL INVESTIGATION OF ENERGY DEPOSITION FOR SUPERSONIC FLOW OVER A 2-D DIAMOND-SHAPED AIRFOIL

BY YE ZHU

A thesis submitted to the

Graduate School—New Brunswick

Rutgers, The State University of New Jersey

in partial fulfillment of the requirements

for the degree of

Master of Science

Graduate Program in Mechanical and Aerospace Engineering

Written under the direction of

Doyle D. Knight

and approved by

_____

_____

_____

_____

New Brunswick, New Jersey

October, 2010

ABSTRACT OF THE THESIS

Numerical Investigation of Energy Deposition for Supersonic Flow over a 2-D Diamond-Shaped Airfoil

by Ye Zhu

Thesis Director: Doyle D. Knight

The research models inviscid compressible flow at Mach 2 over a two dimensional diamond-shaped airfoil. The objective is to study the interaction of the energy deposition added in the upstream flow on the airfoil. Theoretical results without energy deposition in the inlet boundary and numerical results with no filaments, infinitely long symmetric filament, symmetric pulsed filament, and asymmetric pulsed filament, for Mach number, temperature, pressure in the flow field domain, are obtained. An analysis is performed on the drag coefficient acting on the airfoil. FLUENT, Gambit, and C++ are used for the numerical simulation.

Keywords: supersonic flow, compressible, inviscid, 2-D airfoil, energy deposition, filament, shock wave, Prandtl-Meyer expansion, drag coefficient, CFD

Acknowledgements

I wish to express my deepest gratitude to my advisor, Professor Doyle Knight. Professor Knight has provided me with invaluable guidance and inspiration. His leadership and exceptional skills as an advisor had truly brought out the best in me. I would also like to extend my appreciation to members of my graduate committee, Professor Jerry Shan and Professor Tobias Rossman, for their careful evaluations of this thesis.

On the personal side, I was fortunate enough to cross paths with many wonderful people. I am sincerely grateful to all the good friends in the Mechanical and Aerospace Engineering Department. Kellie Anderson showed me that life is not only just about oneself, but also about consideration of others. Mona Golbabaie Asl, thanks for the encouragement, which helped me through tough times. You are always lucky, Mona. Jayeeta Ghosh and Aurora D. Costache showed me how to be a good mother. I will be in my future life. Michelle Lee, thanks for many happy times with you. You are not only my friend, but also like my elder sister. You always gave me good suggestions to deal with all my life. I hope you can graduate soon. Jiandong Meng and Jingru Zhang, both of you let me feel warm in USA. Iris Shi, Maggie Chen, Sharon Shun and Ida Feng, I am so glad I can know you here. We grew stronger together. I sincerely apologize for people I didn't mention. My thanks will always be with you.

I extend a very sweet thanks to my boyfriend, Longji Qi.

And to my best friends, Wei Shao, Tianxiao Chen, Lixia Gong, Jiacheng Shi. We didn't stay together now. But we keep touch with each other all the time. Our friendship forever!

I would like to conclude my acknowledgements with my family. I was loving you, am loving you, will love you, Papa, Mama and Gary.

Dedication

To my parents, Seven, and Wei Shao

Table of Contents

List of Tables

List of Figures

Chapter 1

Introduction

1.1 Motivation

Historically, Prandtl was the first person to create the science of flow control (1904). He delayed the boundary layer separation from the surface of a cylinder by the use of suction. And then, until World War II and the Cold War, in needs of aerodynamics of vehicles and weaponry, the techniques of flow control developed very quickly, which had applications in the military primarily. After the 1970s, the energy crisis broke out, and more and more agencies paid attention to flow control techniques, including national governments and private corporations. They spent substantial amounts of financial, physical and human resources for civilian air, sea, land vehicles and industrial applications [9].

Hypersonic and supersonic vehicles/missiles generate shock waves, which will increase the drag for aircraft. The drag increase will lead to increased fuel consumption. Thus, many challenges are faced with the science of flow control. These include increased drag [10] [11], sonic boom, and destructively high temperatures and pressures on their airframe and components [1], [12].

The energy deposition technique for flow control has attracted growing interest in recent years. Various kinds of discharges - laser, microwave, pulsing high voltage sparks (HVS), etc, - have been studied. Applications with microwave and laser facilities have made great progress in all the new aspects [13], [14], [15], which attracted serious attention connected with their applicability in aerodynamics [26]. Microwave discharge can be realized at a sufficient distance from the vehicle while its position, structure and plasma parameters can be varied quickly [27] [28]. Experimental research with beamed energy deposition in supersonic flow for flow control began more than 15 years ago. There are experimental and theoretical results to demonstrated the effectiveness of energy deposition in front of

a body in supersonic flow for drag reduction and local flow control [16], [17], [18], [19]. Nevertheless, some problems are also revealed during the investigations. It has been shown that the filaments (regions with high temperature and low density), which are oriented along the flow direction, can modify the flowfield [18], [20], [21]. However microwave discharges always have an intrinsic jitter. Laser breakdown, on the other hand, has a consistent shape of a sphere or slightly elongated ellipsoid [22]. It has been proposed to combine the advantages of both the microwave and laser (high precision of the energy deposition region inherent to the laser with the unique parameters of a microwave discharges) [23]. Actually, the laser-guided-microwave technique seems to be a flexible tool of high efficiency in supersonic/hypersonic flow control and shock modification [24].

Numerical modeling of microwave energy filaments in supersonic/hypersonic flows has also generated a great of attention in the past few years. Comparing and analyzing numerical and theoretical results, a reasonable model and explanation for nature can be obtained [30], [31].

1.2 Literature Review

Various energy deposition methods and types of apparatus have been investigated over the past several years with the purpose of reducing drag and/or controling flow on supersonic/hypersonic vehicles and increasing their efficiency of operation.

1.2.1 **Kremeyer** 2004

Kremeyer [1] performed an experimental study of an energy deposition method and apparatus developed over the past several years by PM & AM Research (Physics, Meterials and Applied Methematics Research). Kremeyer used an electric discharge. A laser generated the filaments which form an ionized path that can be used to inject large amounts of energy into the air (Figures 1.1 and 1.2). The numerical simulation points out the extremely high drag reduction in use of the technique (eliminating up to 96% of the drag), at efficiency of up to 6500% (saving 65 times more propulsive energy than the amount of energy deposited

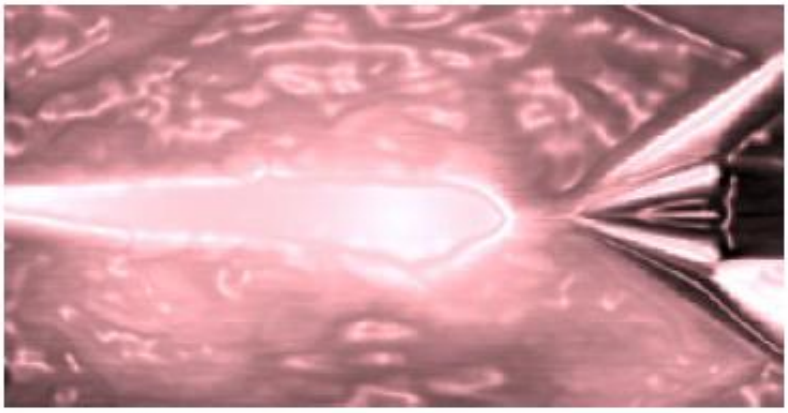

Figure 1.1: An extended path is heated ahead of a cone in supersonic flow. (PM & AM Research) [1]

ahead of the vehicle). Experimental results show that the drag, pressure and the temperature can be reduced. When the air is heated along the stagnation line, the amount of drag reduction is maximized.

1.2.2 **Georgievsky and Levin** 2004

Georgievsky and Levin [2] performed a numerical study of bow shock wave structure control by pulse-periodic energy input. They investigated the effect of pulsing energy sources on a supersonic flow and the bow shock wave structure dynamics for different shape bodies, which are located downstream. The unsteady Euler equations and a model of an "energy source" are used for the numerical simulations. The effect of a "cloud injection" for "choking" energy sources was found, and it was shown that energy sources of "shockless" type are preferable to simulate steady energy input. It was determined by the pulse-periodic energy input that an effective method for transition from the pulsing regime to the quasi-stationary regime is the energy source elongation. Figures 1.3, 1.4 and 1.5 show the supersonic flow over the different body shapes. In all the figures, the energy source size $Q_0 \Delta t = const$, and τ is duration for the pulse-periodic unsteady regimes with rectangular pulses of the period T.

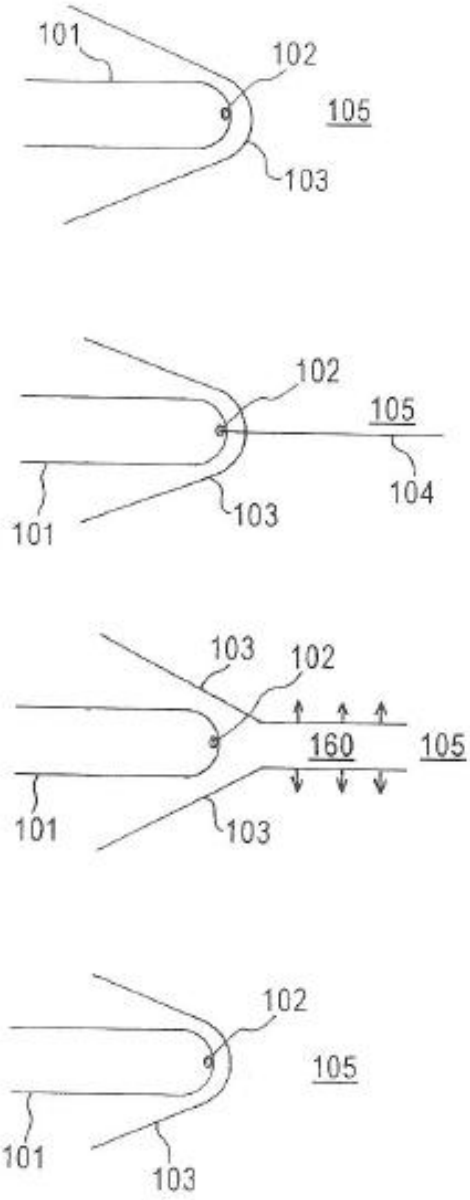

Figure 1.2: Air is heated along the stagnation line ahead of a vehicles bow shock (Kremeyer, USPTO 6,527,221 B1) [1]

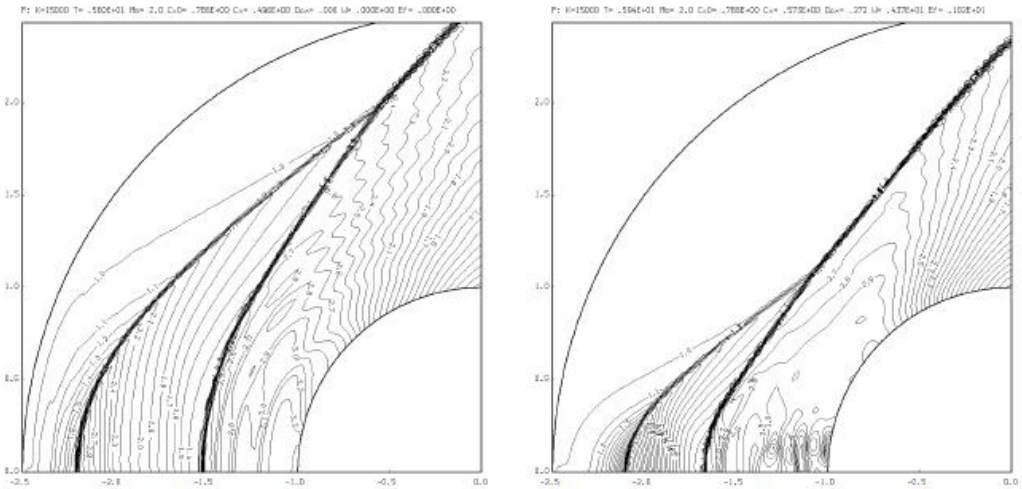

Figure 1.3: Quasi-stationary flow over a sphere in the presence of pulse-periodic energy sources upstream (static pressure p/p_∞ isolines): $M_\infty = 2$, $\gamma = 1.4$ [2]

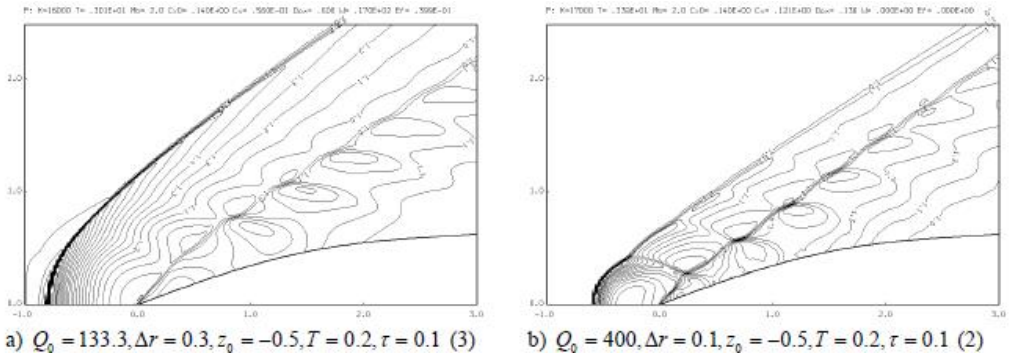

Figure 1.4: Quasi-stationary flow over an ogival-type body in the presence of pulse-periodic energy sources upstream (static pressure p/p_∞ isolines): $M_\infty = 2$, $\gamma = 1.4$ [2]

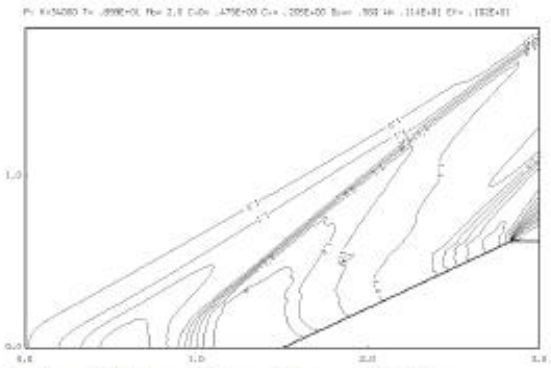

a) $Q_0 = 100, \Delta r = 0.1, \Delta z = 0.5, z_0 = 0.5$ (0)

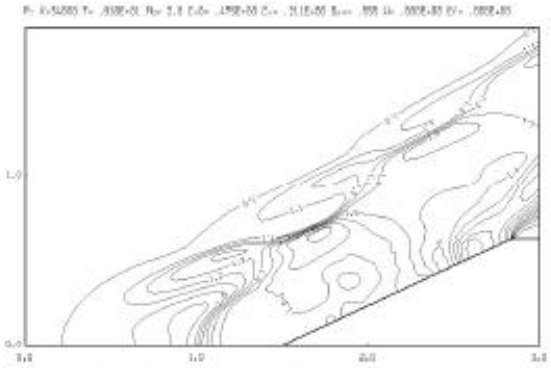

b) $Q_0 = 200, \Delta r = 0.1, \Delta z = 0.5, T = 0.4, \tau = 0.2$ (3)

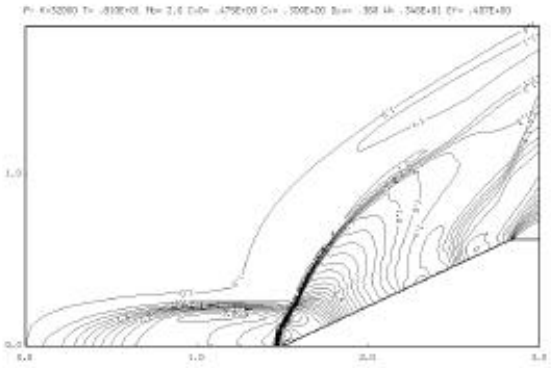

c) $Q_0 = 200, \Delta r = 0.1, \Delta z = 0.5, T = 1.6, \tau = 0.8$ (1)

Figure 1.5: Irregular flow over a 25-degree cone in the presence of pulse-periodic energy sources upstream (static pressure p/p_∞ isolines): $M_\infty = 2$, $\gamma = 1.4$ [2]

Parameters / Functions	α_p=0.3, Δl =0.8	M_∞=1.89, α_p=0.4, Δl=0.8	α_p=0.4, Δl =0.8	α_p=0.4, Δl =1.27
Δp_t	0.958	0.825	0.886	0.862
ΔF	0.927	0.853	0.879	0.925
Δx_w	1.36	0.79	1.03	1.70
V	0.47	0.23	0.33	0.34

Figure 1.6: Results for $M_\infty = 3$ [3].

1.2.3 Lashkov *et al* 2007

Lashkov *et al* [3] performed a combined numerical and experimental study of aerodynamic drag of a body when an energy release domain appears near the body. They provided numerical calculations on the basis of the Euler equations of a thin low-density channel C-shaped shock layer interaction a Mach 3 oncoming flow. Furthermore, they compared the results of numerical (Figure 1.6) results at $M_\infty = 1.89$. New flow structure effects concerning generation and dynamics of shock waves and contact discontinuities were obtained. Also, dynamics of the front drag force, stagnation parameters and bow shock wave coordinate were evaluated. In the experimental part, the experimental model was a sphere of 25 mm diameter. The sphere had an orifice of 1 mm diameter for gas injection of the upstream working flow (see Figure 1.7). The model consisted of a body 1 with a cavity inside it. The cavity was used as a forechamber for injecting gas. It was connected with an air feeding tube 3 and pressure measuring tube 4. The model was placed on a sting 2 with a pressure transducer located inside it. Microwave discharge and counter flow reinforced the influence of each other on drag reduction. Gas injection through the spike on the sphere did not allow the microwave discharge to upset gas moving in the recirculating zone. It diminishes the influence of the discharge on the drag increase of the sphere.

1.2.4 Lashkov *et al* 2008

Lashkov *et al* [4] performed an experimental study of modeling a new microwave focusing system. A supersonic diffuser was designed and manufactured for creating a working flow with Mach 3 in the wind tunnel (Figure 1.8). A microwave discharge was realized at a higher static pressure. A gas heater was built that raised the stagnation temperature in the working flow up to 600-650K. Results of the discharge showed that the bow shock

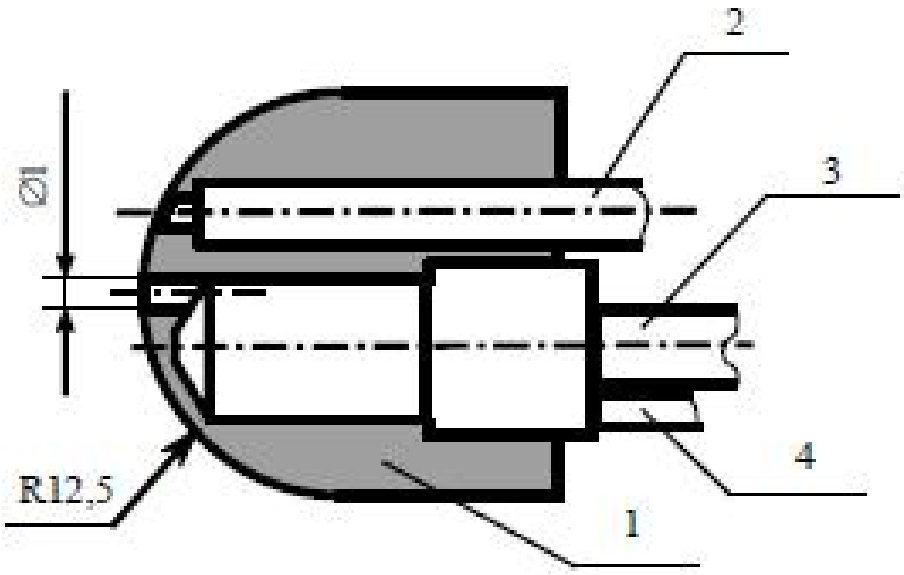

Figure 1.7: The model for investigation of drag under condition of counter flow [3].

wave stands about four times farther off the front surface of the blunt cylinder than under conventional streamlining. The new microwave focusing system and heating of the working gas gave an opportunity to investigate the interaction of a gas heated by microwave discharge with the shock layer on the body over a wide range in Mach number, microwave power and static pressure.

1.2.5 Schülein *et al* 2008

Schülein *et al* [5] performed an experimental and numerical study of shock wave transformation by laser-induced energy deposition. It was shown that the variations in the discharge location could lead to various flow patterns caused by combinations of impinging / reflected blast wave and the thermal spot. As expected, the scales of the interaction increased with higher pulse energy. This trend was also confirmed by increasing the energy of the second impulse in the double pulse regime, while the overall influence is generally comparable in single and double cases for the same total deposited energy. Furthermore, the short delays discussed do not change the interaction much. Further improvements for the numerical model of the source term are necessary for better prediction of the interaction. They identified the model sensitivity to the initial source shape. Experimental and numerical flow fields are shown in Figure 1.9 at the time instant corresponding to the start of the spot /

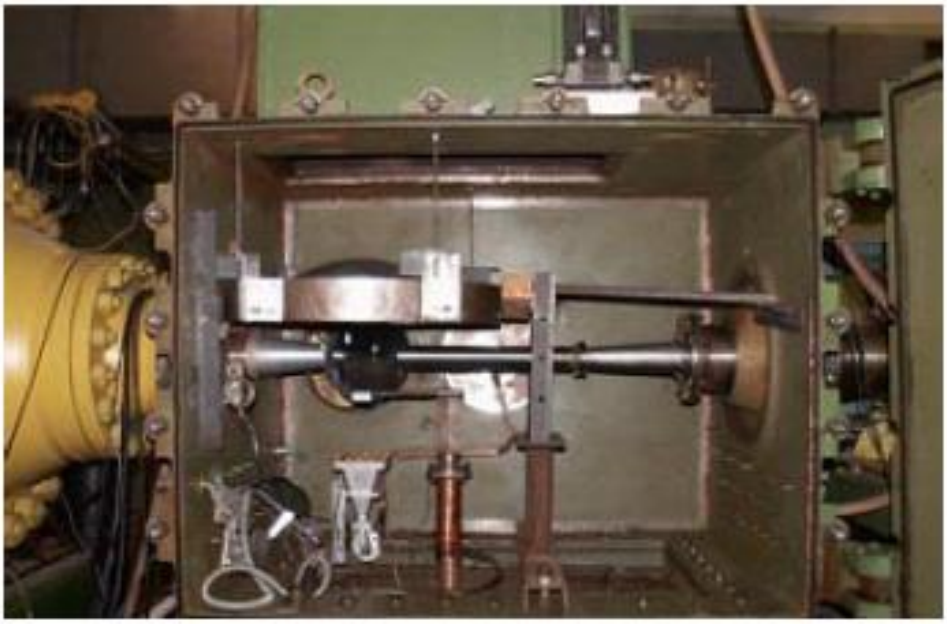

Figure 1.8: The test section with nozzle and diffuser for Mach number $M = 3$ [4].

bow shock interaction (the thermal spot only touches the shock) and at a later time instant.

1.2.6 Knight *et al* 2009*a*

Knight *et al* [32] performed a numerical study of the interaction of a microwave filament and a shock layer on the basis of the Euler equations. In the study, the filaments were regarded as the heated rarefied channels (heat layers). They evaluated the details of the mechanisms of the front body's surface drag force reduction, temporary drag force enhancement and lift/pitch force. A wide range of values of filament characteristics were used in the research: rarefaction factor, location relative to the body and filament sizes (including infinite length). The results shows that drag reduction for a symmetrical filament location is caused by the effect of the vortices on the front body's surface and is connected with the generation of the gas stream directed from the body. Temporary drag increase associated with the generation of a mass of compressed cooler gas near the body via the heated area boundary effect inside the shock layer (heat piston effect). It is shown that in the statistically stationary state in the case of asymmetric filament location the stagnation point forms in a different location compared to the case of the symmetrical filament location, its dynamics being of pulse

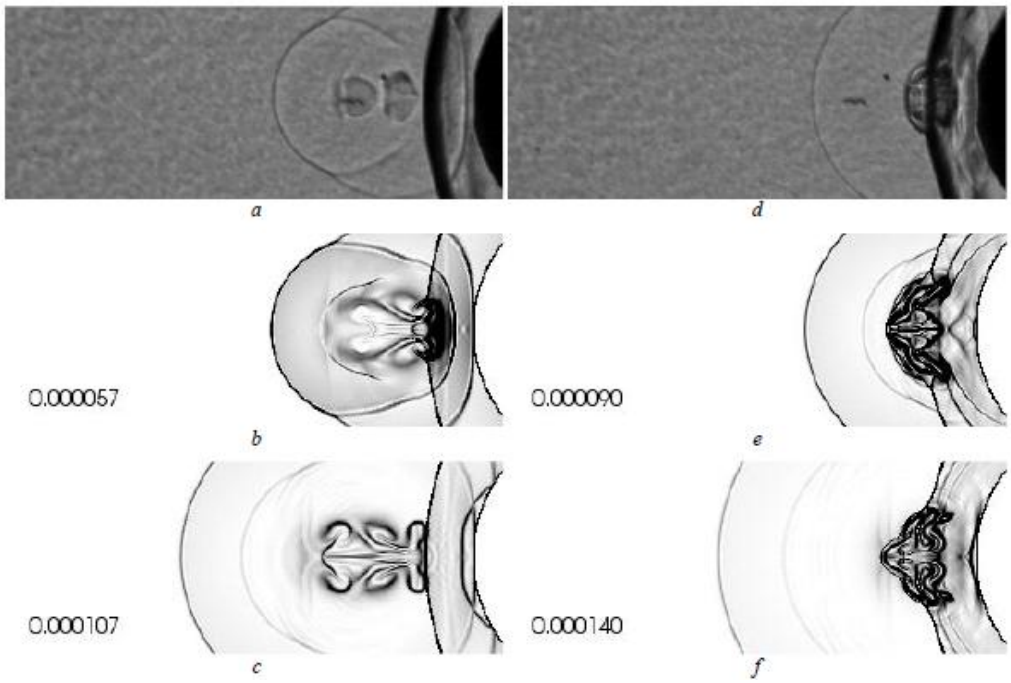

Figure 1.9: Flow structure in double-pulse with energy of both pulses equal to 333 mJ and 20 μs delay at the start of spot / bow shock interaction (left column) and during lensing effect (right column): a, d) experimental pictures for pulses distance 46 mm; b, e) corresponding pictures from simulation; c, f) simulation for pulse distance of 76 mm [5]

character reflecting pulse (stochastic) flow character in total. It is also shown that, in the case of zero attack of angle, the shift of the thermal source from the axis of symmetry leads to the origination of a pitch force, which is a function of a shift value from the symmetry axis of thermal layer and a degree of rarefaction in it.

1.2.7 Knight *et al* 2009*b*

Knight *et al* [6] performed a numerical study of a microwave-generated plasma with the supersonic flow past a hemisphere-cylinder shaped body. The computational domain is shown in Figure 1.10. The code in the study is fully three-dimensional and time-accurate. The thermochemistry model includes 23 species and 238 reactions. The computed and experimental surface pressure vs time on the centerline of the body surface for the hemisphere cylinder are shown in Figure 1.11a. The surface pressures between the computed and experimental results agree very well. The effect of the filtering on the computed centerline pressure is shown in Figure 1.11b. Furthermore, the filtering significantly reduces the magnitude of the computed pressure drop associated with the interaction of the microwave-generated plasma and the hemisphere cylinder. Significant nonequilibrium effects are observed throughout the interaction; in particular, the level of atomic oxygen remains high through the interaction of the plasma with the blunt body.

1.2.8 Mahapatra *et al* 2009

Mahapatra *et al* [7] performed an experimental study of the effect of counter flow plasma injection (Figure 1.12 shows a typical schlieren photograph obtained for a plasma jet) on the aerodynamic drag of a hemispherical blunt cylinder model in hypersonic shock tunnel at four different pressure ratios and varying supply power. The pressure ratio is $p = p_{0j}/p_{0f}$, with values of 15.3, 24.52, 72.5 and 96.67, where p_{0j} is the jet total pressure (taken as the cylinder supply pressure) and p_{0f} is the pitot pressure of the test flow and at different values of power (by varying the current of the supply unit). A schematic diagram of the experimental facility is given in Figure 1.13. It is demonstrated that at a higher pressure ratio there is a significant reduction of drag in the presence of the plasma. Furthermore, the reduction of drag is due to the combined effect of jet-bow shock interaction and the

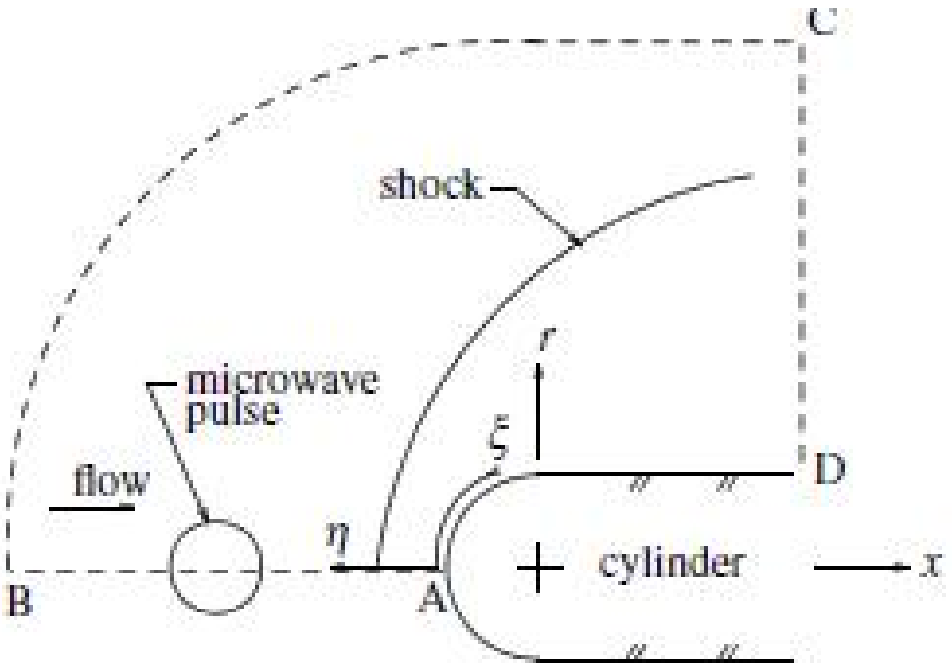

Figure 1.10: Computational domain [6]

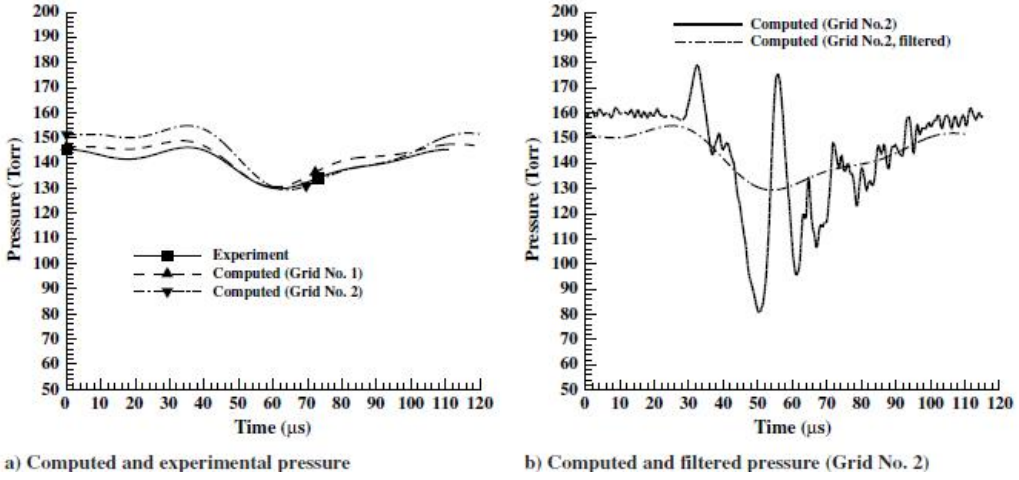

Figure 1.11: Computed and experimental pressure on hemisphere-cylinder centerline [6]

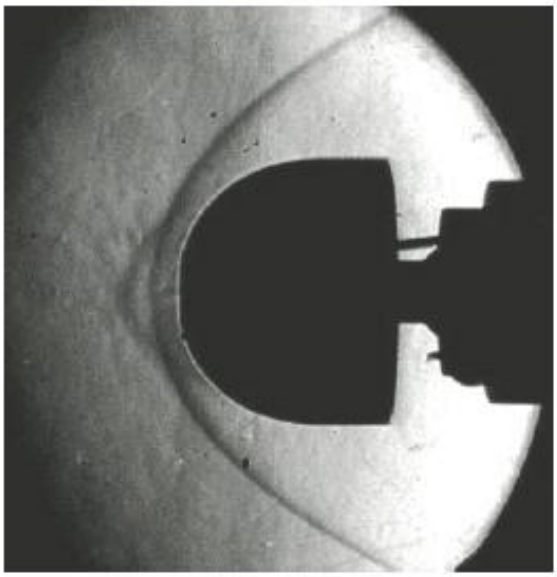

Figure 1.12: A typical schlieren photograph obtained for a plasma jet [7]

thermal effect of plasma jet.

1.2.9 Sasoh *et al* 2009

Sasoh *et al* [8] developed an experimental system to examine drag reduction performance with repetitive laser pulse irradiations. The results demonstrated that the time-averaged drag over the cylinder nose is reduced. The calculation of the accuracy of the measurement, in particular associated with the friction force between the cylinder body and the housing caused by the O-rings-shape (Figure 1.14), shows the O-rings-shape used in the experiments should make evaluation more accurate.

1.3 Statement of Objectives

The objective of this research is to perform a numerical simulation of a simplified model of an energy deposition filament, which has an effect on the flow structure over a two dimensional diamond-shaped airfoil. The flow is compressible and inviscid with Mach number 2. The plasma filament generated by a microwave discharge is simulated as a "thermal spot"(a region of high temperature and thus low density). The filament convects past the wedge-shaped body and alters the flow structure. The research will show the behavior of the

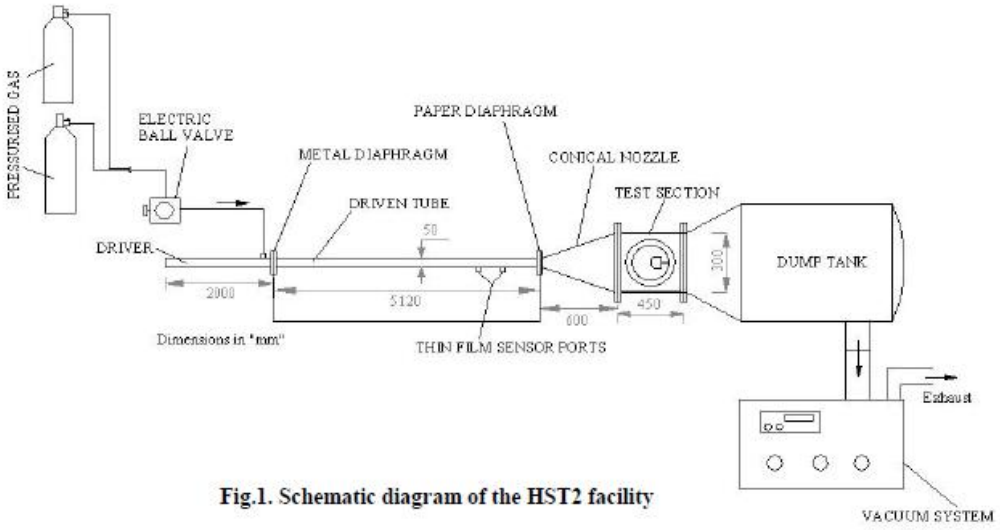

Figure 1.13: Experimental set-up [7]

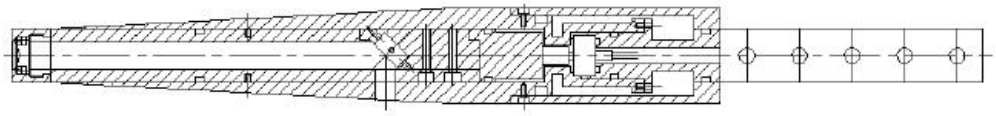

Figure 1.14: Test cylinder body and its housing for drag measurement [8]

upstream flow occuring near the airfoil. Furthermore, the effect of variation of filament height, energy deposition position in the inflow boundary and length of filament on the drag coefficient on the airfoil are investigated.

Chapter 2

Statement of Problem

2.1 Problem Description

Consider inviscid compressible freestream flow past a 2-D diamond-shaped symmetric airfoil with Mach number 2 at the inflow. The schematic of this research is shown in Figure 2.1. The properties of the freestream are in Table 2.1.

The energy deposition is added at the inflow boundary. The density of the energy deposition region is lower than the freestream. The ratio of the filament density to the freestream density is defined as α. In this case, α equals 0.5. Consequently the temperature of the energy deposition region is higher, i.e., double the upstream temperature, since the static pressure in the energy deposition region is assumed equal to the freestream static pressure.

In Figure 2.1, the width, the height, and the half angle of the airfoil are c, t and δ ($\delta = 10°$) respectively. The length and height of each pulsed filament are l and d, respectively. The distance from right/left point of each filament to the same point of the adjacent filament is L. The vertical distance from the center of the energy deposition to the center of the airfoil is h.

There are three dimensionless flow parameters in the case: the Mach number M_∞, the ratio of filament density to freestream density α, and the ratio of specific heats γ. In the study of the inviscid problem, four more dimensionless parameters are added: $\frac{d}{t}$, $\frac{l}{t}$, $\frac{L}{t}$, and $\frac{h}{t}$. All the dimensionless parameters of each type in the study are shown in Table 2.3 and the cases studied are shown in Table 2.2. From the dimensionless parameters, the values of the properties of the filament are obtained in Table 2.4 (The filament is assumed to be at equilibrium).

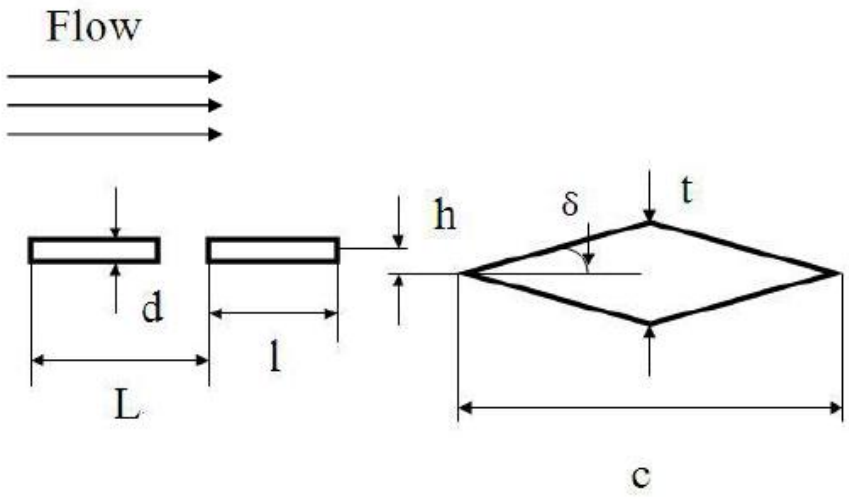

Figure 2.1: Schematic of the problem description

Table 2.1: Properties of the freestream

Properties	
Pressure P_∞	101325 Pascal
Temperature T_∞	300 K
Mach number M_∞	2.0
Angle of attack	0

Table 2.2: Dimensionless Parameters

Type	Description	Definition	Value
Flow	Mach number	M_∞	2.0
	Specific heats ratio	γ	1.4
Filamant	Density ratio	α	0.5
	Height	$\frac{d}{t}$	varies
	Length	$\frac{l}{t}$	varies
	Pulse (Period)	$\frac{L}{t}$	varies
	Symmetric or not	$\frac{h}{t}$	varies

Table 2.3: Study Case

Type	$\frac{d}{t}$	$\frac{l}{t}$	$\frac{L}{t}$	$\frac{h}{t}$
Symmetric	0.1 0.25 0.5 1.0	∞	n/a	0
	0.1 0.25 0.5 1.0	1	2	0
Asymmetric	0.1 0.25 0.5 1.0	1	2	0.25

Table 2.4: Properties of the filament

Properties	
Pressure P_f	101325 Pascal
Temperature T_f	600 K
Mach number M_f	1.414
Angle of attack	0

2.2 Formulation

2.2.1 Governing Equations

This flow is assumed to be inviscid and compressible. The mass, momentum, and energy conservation equations are described in Equations (2.1), (2.2) and (2.3), where the Einstein summation convention is used [33].

Conservation of Mass:

$$\frac{\partial \rho}{\partial t} + \frac{\partial \rho u_j}{\partial x_j} = 0 \tag{2.1}$$

Conservation of Momentum:

$$\frac{\partial \rho u_i}{\partial t} + \frac{\partial \rho u_i u_j}{\partial x_j} = -\frac{\partial p}{\partial x_i} \tag{2.2}$$

Conservation of Energy

$$\frac{\partial \rho e}{\partial t} + \frac{\partial (\rho e + p) u_j}{\partial x_j} = 0 \tag{2.3}$$

The total energy per unit mass is given by

$$e = c_v T + \frac{1}{2} u_j u_j \tag{2.4}$$

The total enthalpy is

$$H = h + \frac{1}{2} u_i u_i \tag{2.5}$$

where h is the static enthalpy, defined as

$$h = c_V T + \frac{p}{\rho} \tag{2.6}$$

2.2.2 Nondimensionalization

All the equations in section 2.2.1 are nondimensionlized by employing the following transformations:

$$u_i^* = \frac{u_i}{U_{ref}}$$

$$x_i^* = \frac{x_i}{L_{ref}}$$

$$\text{time}^* = \frac{\text{time}}{L_{ref}/U_{ref}}$$

$$p^* = \frac{p}{\rho_{ref} \cdot U_{ref}^2}$$

$$T^* = \frac{T}{T_{ref}}$$

$$\rho^* = \frac{\rho}{\rho_{ref}}$$

$$e^* = \frac{e}{U_{ref}^2}$$

The airfoil thickness (t) and the variables of the freestream are chosen as characteristic values:

$$U_{ref} = U_\infty$$

$$L_{ref} = t$$

$$\rho_{ref} = \rho_\infty$$

$$T_{ref} = T_\infty$$

Then,

$$u_i^* = \frac{u_i}{U_\infty} \tag{2.7}$$

$$x_i^* = \frac{x_i}{L_\infty} \tag{2.8}$$

$$\text{time}^* = \frac{\text{time}}{L_\infty / U_\infty} \tag{2.9}$$

$$p^* = \frac{p}{\rho_\infty \cdot U_\infty^2} \tag{2.10}$$

$$T^* = \frac{T}{T_\infty} \tag{2.11}$$

$$\rho^* = \frac{\rho}{\rho_\infty} \tag{2.12}$$

$$e^* = \frac{e}{U_\infty^2} \tag{2.13}$$

The dimensionless variables are denoted with a superscript $*$ above.

2.2.3 Governing Equations in Dimensionless Form

Equations (2.7), (2.8), (2.9), (2.10), (2.11), (2.12) and (2.13) are substituted into Equations (2.1), (2.2) and (2.3). The governing equations in dimensionless form are as follows:

Conservation of Mass:

$$\frac{\partial \rho^*}{\partial t^*} + \frac{\partial \rho^* u_j^*}{\partial x_j^*} = 0 \tag{2.14}$$

Conservation of Momentum:

$$\frac{\partial \rho^* u_i^*}{\partial t^*} + \frac{\partial \rho^* u_i^* u_j^*}{\partial x_j^*} = -\frac{\partial p^*}{\partial x_i^*} \tag{2.15}$$

Conservation of Energy

$$\frac{\partial \rho^* e^*}{\partial t^*} + \frac{\partial (\rho^* e^* + p^*) u_j^*}{\partial x_j^*} = 0 \tag{2.16}$$

And the total enthalpy becomes

$$H^* = h^* + \frac{1}{2} u_i^* u_i^* \tag{2.17}$$

where h^* becomes

$$h^* = \frac{p^*}{\rho^*} \tag{2.18}$$

2.2.4 Boundary Conditions in Dimensionless Form

At the inflow boundary, the filament travels with the same speed as the freestream and the pressure is the same as the freestream pressure. Because

$$\rho = \frac{p}{RT}$$

$$\frac{\rho_f}{\rho_\infty} = \alpha = 0.5$$

Thus

$$T_f = 2T_\infty$$

And because

$$M = \frac{U}{\sqrt{\gamma \frac{p}{\rho}}}$$

Thus

$$M_f = \sqrt{\alpha} M_\infty$$

The boundary conditions are nondimensionalized by using the dimensionless variables

- Upstream flow Mach number

$$M_\infty^* = \frac{M_\infty}{M_\infty} = 1$$

- Filament Mach number

$$M_f^* = \frac{M_f}{M_\infty} = \sqrt{\alpha}$$

- Upstream flow pressure

$$p_\infty^* = \frac{p}{\rho_\infty U_\infty^2} = \frac{1}{\gamma M_\infty^2}$$

- Filament pressure

$$p_f^* = p_\infty^*$$

- Upstream flow temperature

$$T_\infty^* = \frac{T_\infty}{T_\infty} = 1$$

- Filament temperature

$$T_f^* = 2T_\infty^* = 2$$

2.2.5 Governing Equations in Vector Form

The system of governing equations for a single-component fluid, written to describe the mean flow properties, is cast in integral Cartesian form for an arbitrary control volume V with differential surface area $d\boldsymbol{A}$ as follows:

$$\frac{\partial}{\partial t}\int_V \boldsymbol{Q} dV + \oint \boldsymbol{F} \cdot d\boldsymbol{A} = 0 \tag{2.19}$$

where the vectors $\boldsymbol{Q}$ and $\boldsymbol{F}$ are defined as

$$\boldsymbol{Q} = \left\{ \begin{array}{c} \rho \\ \rho u \\ \rho v \\ e \end{array} \right\} \tag{2.20}$$

$$\boldsymbol{F} \cdot d\boldsymbol{A} = \left\{ \begin{array}{c} \rho \vec{\boldsymbol{v}} \cdot \vec{\boldsymbol{n}} \\ \rho u \vec{\boldsymbol{v}} \cdot \vec{\boldsymbol{n}} + n_x p \\ \rho v \vec{\boldsymbol{v}} \cdot \vec{\boldsymbol{n}} + n_y p \\ (e+p) \vec{\boldsymbol{v}} \cdot \vec{\boldsymbol{n}} \end{array} \right\} dA \tag{2.21}$$

where

$$d\boldsymbol{A} = \vec{\boldsymbol{n}} dA$$

Here ρ, $\boldsymbol{v}$, e, and p are the density, velocity, total energy per unit mass, and pressure of the fluid, respectively.

Total energy e is related to the total enthalpy H by

$$e = H - p/\rho \tag{2.22}$$

where H is defined by Equation (2.5).

Chapter 3

Numerical Method

The numerical model calculates the solution of coupled non-linear partial differential equations governing continuity, momentum and energy conservation. Solution of this nonlinear problem is further discussed by the addition of the drag coefficient.

A finite volume technique is used along with a uniform grid arrangement. The governing equations of continuity, momentum, and energy must be solved simultaneously, i.e, all the equations coupled together. The selected spatial and temporal discretization for each equation in the coupled set of governing equations is linearized explicitly [34].

3.1 The Finite Volume Method

The finite volume method is used to solve the continuity, momentum and energy equations. The physical domain can be separated into numerous sections without overlapping. All these numerous sections are called control volumes. Each control volume contains a cell centered node, which represents pressure, temperature or Mach number. Control volumes are constructed, so only one node is centered within every control volume. The variables in every two neighbouring control volumes are assumed linear.

Commercial finite volume codes like FLUENT are available for the finite volume method. For this project, the energy deposition requires flexibility to modify. UDF (User-defined function, which allows to customize FLUENT and can significantly enhance its capabilities) can be used to solve the current problem in the boundary conditions. The programming code for UDF is C++.

3.2 Convective Flux

3.2.1 Roe Flux-Difference Splitting Scheme

The inviscid flux vector F is evaluated by a standard upwind, flux-difference splitting. This approach acknowledges that the flux vector F contains characteristic information propagating through the domain with speed and direction according to the eigenvalues of the system. By splitting F into parts, where each part contains information traveling in a particular direction (i.e., characteristic information), and upwind differencing the split fluxes in a manner consistent with their corresponding eigenvalues, the following expression can be obtained for the discrete flux at each face:

$$F = \frac{1}{2}(F_R + F_L) - \frac{1}{2}\Gamma|\hat{A}|\delta Q \tag{3.1}$$

Here δQ is the spatial difference $Q_R - Q_L$. The fluxes $F_R = F(Q_R)$ and $F_L = F(Q_L)$ are computed using the (reconstructed) solution vectors Q_R and Q_L on the "right" and "left" side of the face. Γ is the preconditioning matrix in the FLUENT for preconditioned system. The matrix $|\hat{A}|$ is defined by

$$|\hat{A}| = M|\Lambda|M^{-1} \tag{3.2}$$

where Λ is the diagonal matrix of eigenvalues and M is the matrix that diagonalizes A, where A is the inviscid flux Jacobian $\partial F/\partial Q$.

For the non-preconditioned system (and an Ideal Gas) Equation (3.1) reduces to Roe's flux-difference splitting when Roe-averaged values are used to evaluate $\Gamma|\hat{A}|$. At present, arithmetic averaging of states Q_R and Q_L is used.

In its current form, Equation (3.1) can be viewed as a second-order linear combination plus an added matrix dissipation. The added matrix dissipation term can be responsible for producing an upwinding of the convected variables, and of pressure and flux velocity in supersonic flow.

3.3 Discretization

A control volume-based technique is used to convert a general scalar transport equation to an algebraic equation that can be solved numerically. This control volume technique consists of integrating the transport equation about the each control volume, yielding a discrete equation expresses the conservation law on a control volume basis.

Discretization of the governing equations can be illustrated most easily by considering the unsteady conservation for transport of a scalar quantity ϕ. This is demonstrated by the following equation written in integral form for an arbitrary control volume V as follows:

$$\int_V \frac{\partial \rho\phi}{\partial t} dV + \oint \rho\phi\vec{v} \cdot d\vec{A} = \oint \gamma_\phi \bigtriangledown \phi \cdot d\vec{A} + \int_V S_\phi dV \tag{3.3}$$

where

$$\rho = \text{density}$$

$$\vec{v} = \text{velocity vector} = u\hat{i} + v\hat{j} \text{ in 2D}$$

$$d\vec{A} = \text{surface area vector}$$

$$\gamma_\phi = \text{diffusion coefficient for } \phi$$

$$\nabla\phi = (\partial\phi/\partial x)\hat{i} + (\partial\phi/\partial y)\hat{j} \text{ in 2D}$$

$$S_\phi = \text{sourse of } \phi \text{ per unit volume}$$

Equation (3.3) is applied to each control volume, or cell, in the computational domain.

3.3.1 Spatial Discretization Scheme

Values of the scalar ϕ at the cell centers are discretized. However, face values ϕ_f are required for the convection terms in Equation (3.3) and must be interpolated from the cell center values. This is accomplished using an upwind scheme.

Upwinding means that the face value ϕ_f is derived from quantities in the cell upstream, or "upwind", relative to the direction of the normal velocity v_n in Equation (3.3).

In this problem, second-order accuracy is needed. Quantities at cell faces are computed using a multidimensional linear reconstruction approach. In this approach, higher-order accuracy is achieved at cell faces through a Taylor series expansion of the cell-centered solution about the cell centroid. Thus when second-order upwinding is selected, the face value ϕ_f is computed using the following expression:

$$\phi_{f,SOU} = \phi + \bigtriangledown\phi \cdot \vec{r} \tag{3.4}$$

where ϕ and $\bigtriangledown\phi$ are the cell-centered value and its gradient in the upstream cell, and $\vec{r}$ is the displacement vector from the the upstream cell centroid to the face centroid. This formulation requires the determination of the gradient $\bigtriangledown\phi$ in each cell. Finally, the gradient $\bigtriangledown\phi$ is limited so that no new maxima or minima are introduced.

3.3.2 Temporal Discretization Scheme

In the explicit scheme a multi-stage, time-stepping algorithm is used to discretize the time derivative in Equation (2.19).

The solution is advanced from iteration n to iteration $n+1$ with an m-stage Runge-Kutta scheme, given by

$$\boldsymbol{Q}^0 = \boldsymbol{Q}^n$$

$$\triangle\boldsymbol{Q}^i = -\alpha_i \triangle t \Gamma^{-1} \boldsymbol{R}^{i-1}$$

$$\boldsymbol{Q}^{n+1} = \boldsymbol{Q}^m$$

where $\Delta\boldsymbol{Q}^i \equiv \boldsymbol{Q}^i - \boldsymbol{Q}^n$ and $i = 1, 2, \ldots, m$ is the stage counter for the m-stage scheme. α_i is the multi-stage coefficient for the i^{th} stage. The residual $\boldsymbol{R}^i$ is computed from the intermediate solution $\boldsymbol{Q}^i$ and, for Equation 2.19, is given by

$$\mathbf{R}^i = \sum^{N_{\text{faces}}} \boldsymbol{F}(\boldsymbol{Q}^i) \cdot d\boldsymbol{A} \tag{3.5}$$

For transient simulations, the governing equations must be discretized in both space and time. The spatial discretization for the time-dependent equation is identical the steady-state case. Temporal discretization involves the integration of every term in the differential equations over a time step $\triangle t$. The integration of the transient terms is the straight forward, as shown below:

$$\frac{\partial \phi}{\partial t} = F(\phi) \tag{3.6}$$

where the function F incorporates any spatial discretization. If the time derivative is discretized using forward differences, the first-order accurate temporal discretization is given by

$$\frac{\phi^{n+1} - \phi^n}{\triangle t} = F(\phi^n) \tag{3.7}$$

and the second-order discretization is given by

$$\frac{3\phi^{n+1} - 4\phi^n + \phi^{n-1}}{2 \triangle t} = F(\phi^n) \tag{3.8}$$

where

$$\phi = \text{a scalar quantity}$$

$$n+1 = \text{value at the next time level}, t + \triangle t$$

$$n = \text{value at the current time level}, t$$

$$n-1 = \text{value at the previous time level}, t - \triangle t$$

Unsteady shock waves are generated in this research, so an explicit fourstage Runge-Kutta method is chosen (see above).

The time step $\triangle t$ is restricted to the stability limit of the Courant-Friedrich-Lewy condition. In order to be time-accurate, all cells in the domain must use the same time step. For stability, this time step must be the minimum of all the local time steps in the domain. This method is also referred to as "global time stepping". To maintain time accuracy of the solution the explicit time stepping employs the same time step in each cell of the domain (global time step).

3.4 Numerical Grid Generation

Grid sizing is chosen based on solution accuracy and computational effort. Grid density in increased until it does not significantly affect the solution. This procedure will ensure independence between grid sizing and solution accuracy.

The grid generation code is Gambit. The physical domain is divided into nine zones. Figure 3.4 shows this structured algebraic configuration. Figure 3.3 is the total meshed domain generated by Gambit. In Figure 3.4, AL and LK are defined as inlet flow boudaries. AB, BC, CD, DE, EF, FG, GH, HI, IJ, and JK are defined as outlet flow boudaries. There are 70074 nodes in the meshed domain figure. In boundaries MN, NO, OP and PM (airfoil zone), there are 324 mixed wall (boundary condition type in FLUENT) faces altogether. In the outlet flow boundaries, mixed pressure-far-field (boundary condition type in FLUENT) faces are numbered 1074 totally. Mixed pressure-far-field faces are counted 150 in the inlet flow boundaries. There are 69300 quadrilateral cells in the whole mesh domain except airfoil, which is described in Figures 3.2, 3.3 and 3.4.

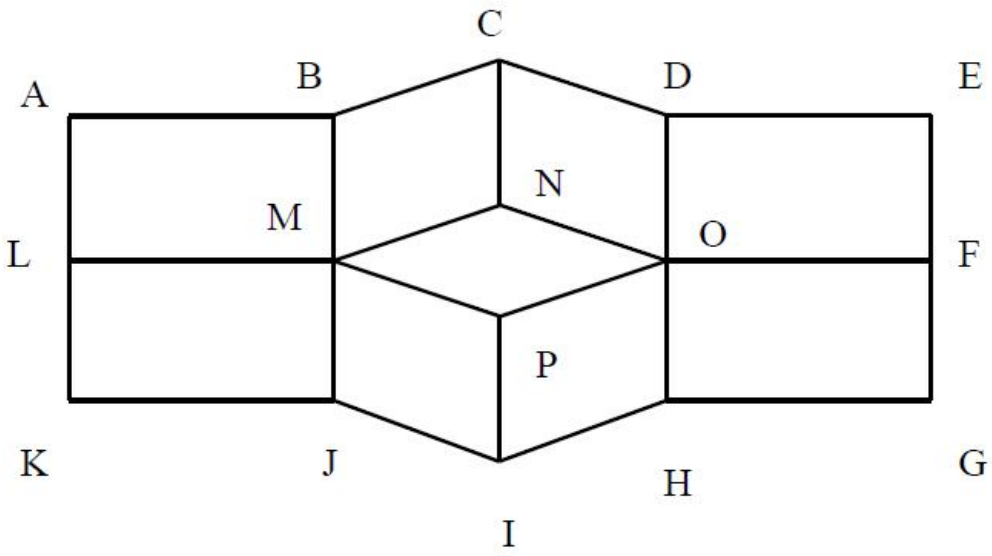

Figure 3.1: Geometrical configuration of the problem description

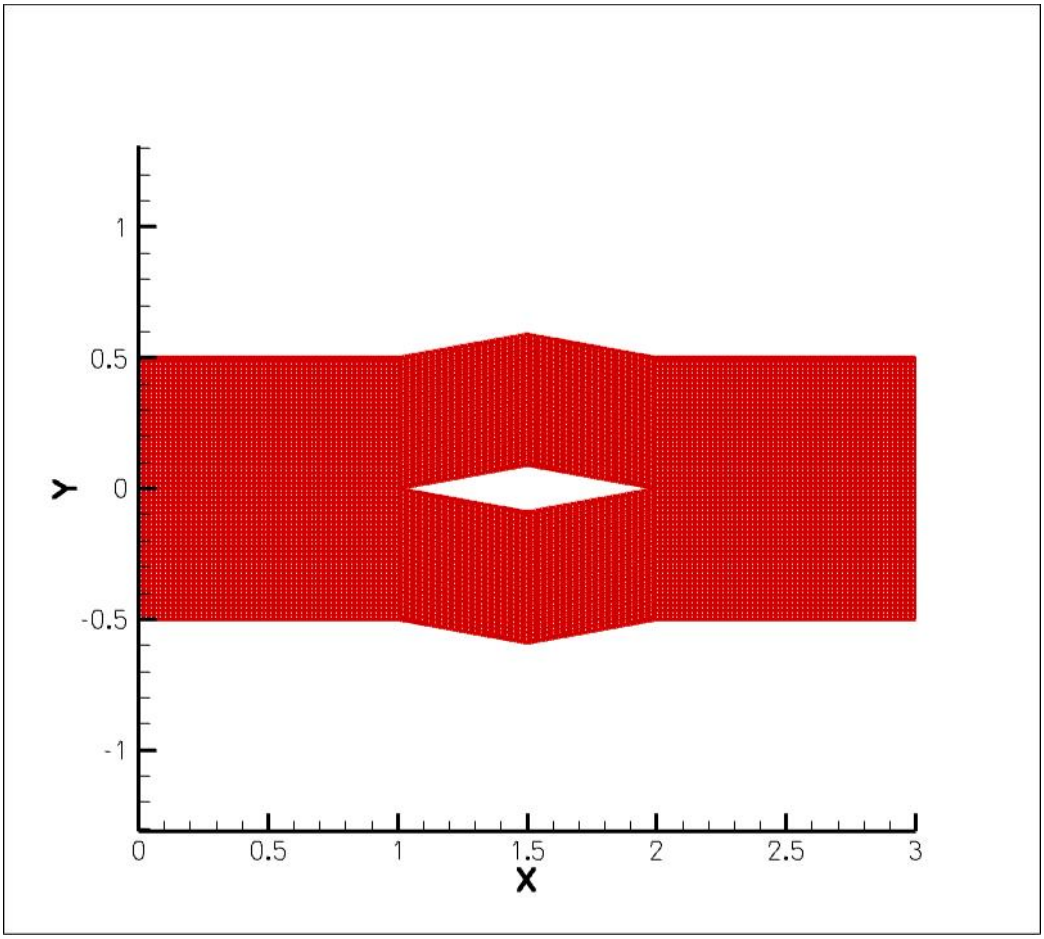

Figure 3.2: The meshed domain of MPIJ

3.5 Calculation Procedure at Boundaries

In this case, the calculation procedures in each inflow or outflow boundary are the same. This boundary condition is a non-reflecting boundary condition based on the introduction of Riemann invariants (i.e., characteristic variables) for a one-dimensional flow normal to the boundary. For flow there are two Riemann invariants, corresponding to incoming and outgoing waves:

$$R_\infty = v_{n\infty} - \frac{2c_\infty}{\gamma - 1} \tag{3.9}$$

$$R_i = v_{ni} + \frac{2c_i}{\gamma - 1} \tag{3.10}$$

where v_n is the velocity magnitude normal to the boundary, c is the local speed of sound

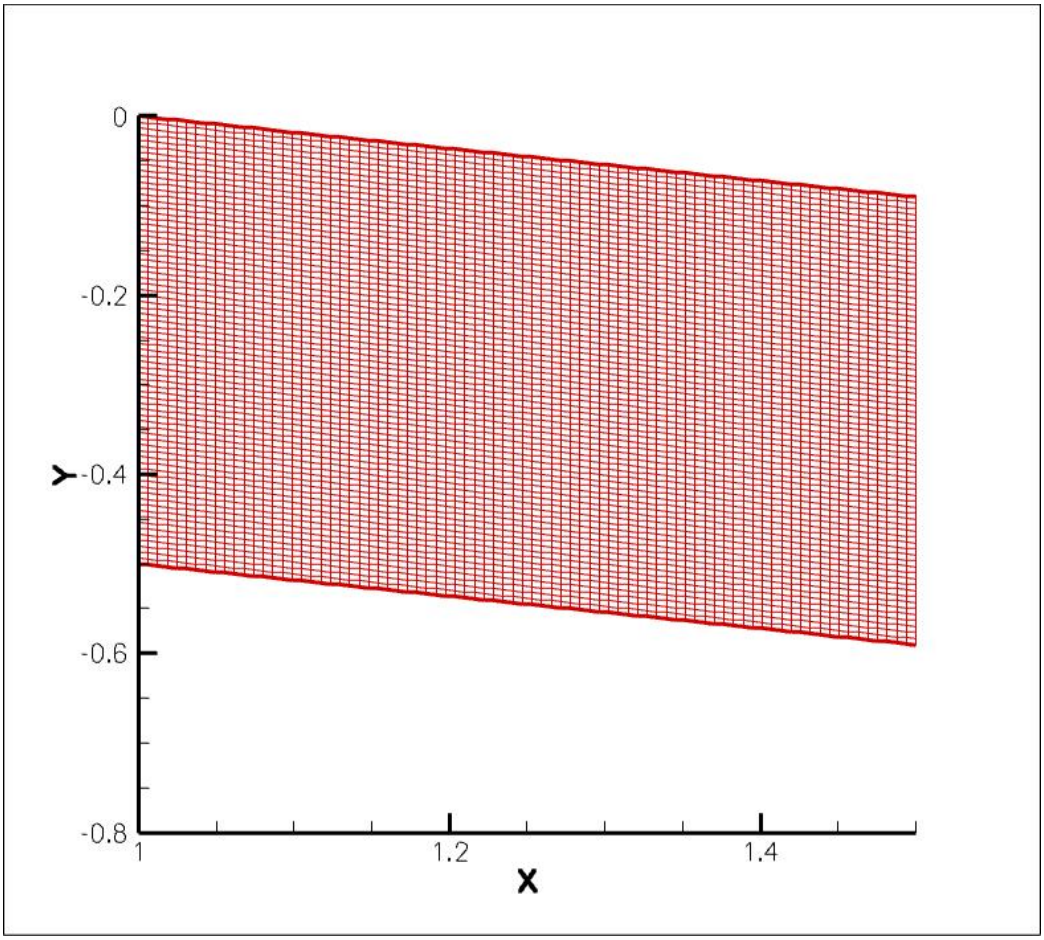

Figure 3.3: The meshed domain of MPIJ

and γ is the ratio of specific heats (ideal gas). The subscript ∞ refers to conditions being applied at infinity (the boundary conditions), and the subscript i refers to conditions in the interior of the domain (i.e., in the cell adjacent to the boundary face). These two invariants can added and subtracted to give the following two equations:

$$v_n = \frac{1}{2}(R_i + R_\infty) \tag{3.11}$$

$$c = \frac{\gamma - 1}{4}(R_i - R_\infty) \tag{3.12}$$

where v_n and c become the values of normal velocity and sound speed applied on the boundary. At a face through which flow exits, the tangential velocity components and entropy are extrapolated from the interior; at an inflow face, these are specified as having

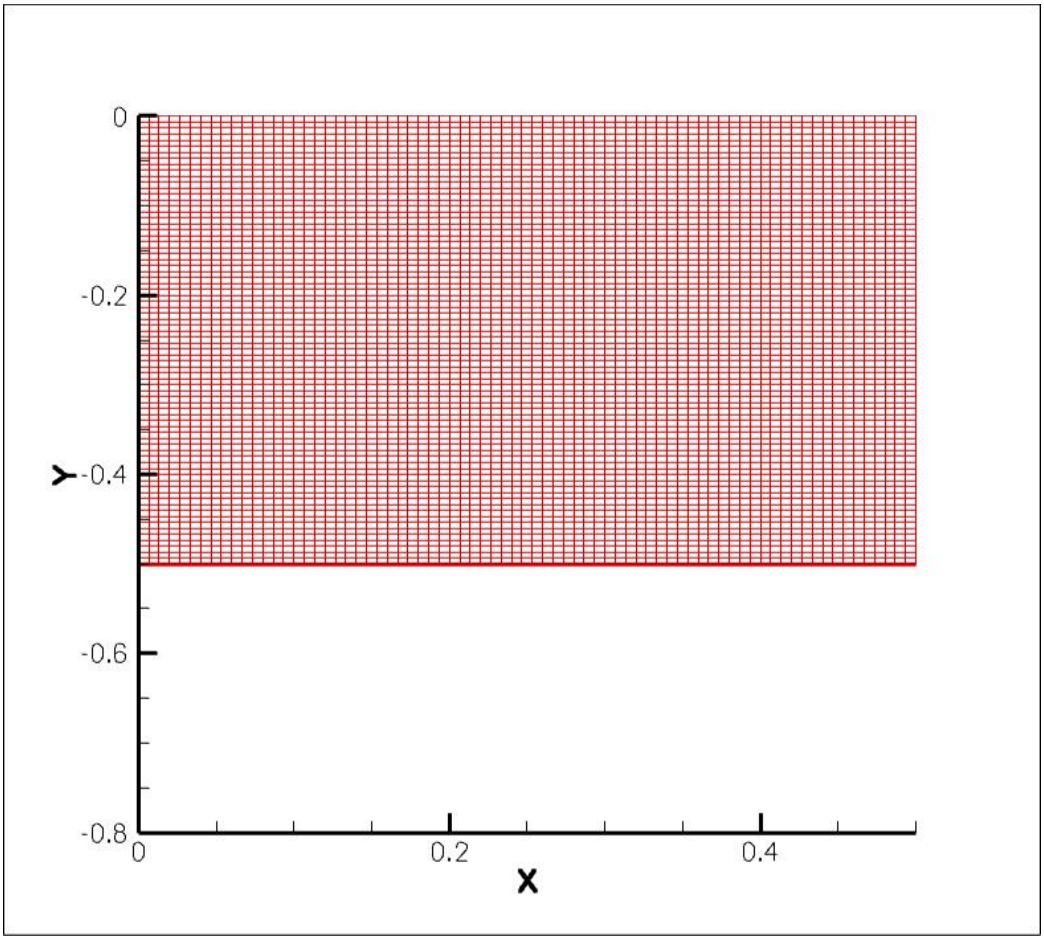

Figure 3.4: The meshed domain of LMJK

free-stream values. Using the values for v_n, c, tangential velocity components, and entropy, the values of density, velocity, temperature, and pressure at the boundary face can be calculated.

During the calculation, the filament is added in the inlet flow boundaries. The code to generate the filament was developed in this case. And UDF (User Defined Function in FLUENT) was used to deal with the filament addition. The original filament generation code was written in C++.

3.6 Code Validation

To make sure the correctness and accuracy of numerical results, the simplest method is to compare results with the theoretical results. For convenience, an illustrated example is the

case with no filament at the inlet boundary. The numerical solutions are shown in Figure 3.5

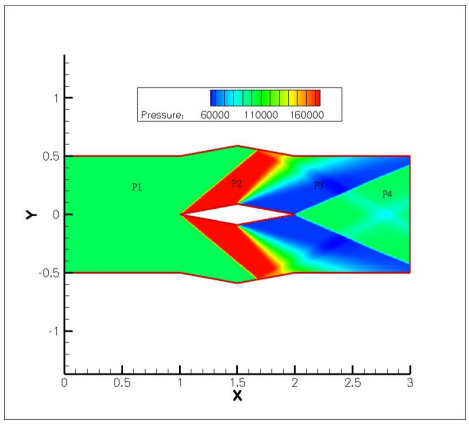

(a) Pressure contour of numerical solution without filament

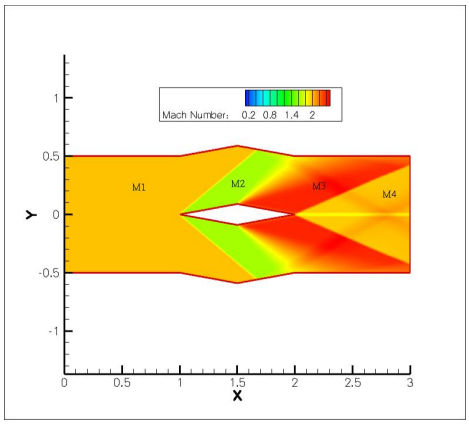

(b) Mach Number contour of numerical solution without filament

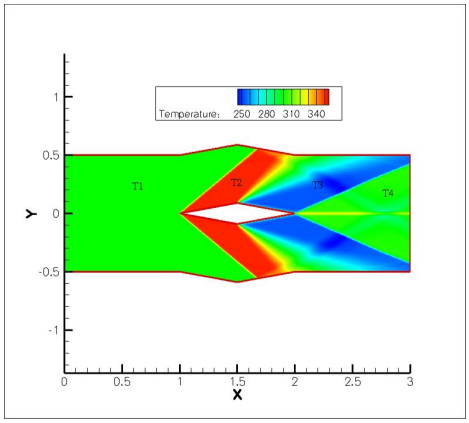

(c) Temperature contour of numerical solution without filament

Figure 3.5: Contours of numerical solution with no energy deposition in the flow inlet boundary

As for the theoretical results, some general results can be predicted. In the no energy deposition case, the first oblique shock wave would be generated in the Point M. Prandtl Meyer expansion is to appear in Point N and P. At last, the second oblique shock wave occurs in Point O (M, N, P and O can be seen in Figure 3.4).

The variables with subscript 1 are parameters for the upstream flow before shock wave. The variables with subscript 2 are for the downstream after shock wave. β is the angle of

the shock wave, and angle θ is flow deflection angle.

The oblique shock relations can be summarized below [35], [36]:

$$\frac{\rho_2}{\rho_1} = \frac{(\gamma+1)M_1^2 \sin^2\beta}{(\gamma-1)M_1^2 \sin^2\beta + 2} \tag{3.13}$$

$$\frac{p_2}{p_1} = 1 + \frac{2\gamma}{\gamma+1}(M_1^2 \sin^2\beta - 1) \tag{3.14}$$

$$\frac{T_2}{T_1} = [1 + \frac{2\gamma}{\gamma+1}(M_1^2 \sin^2\beta - 1)][\frac{(\gamma-1)M_1^2 \sin^2\beta + 2}{(\gamma+1)M_1^2 \sin^2\beta}] \tag{3.15}$$

$$M_2^2 \sin^2(\beta-\theta) = \frac{(\gamma-1)M_1^2 \sin^2\beta + 2}{2\gamma M_1^2 \sin^2\beta - (\gamma-1)} \tag{3.16}$$

$$\cot\theta = \tan\beta[\frac{(\gamma+1)M_1^2}{2(M_1^2 \sin^2\beta - 1)} - 1] \tag{3.17}$$

The angle υ is the Prandtl-Meyer function,

where

$$\upsilon(M) = \sqrt{\frac{\gamma+1}{\gamma-1}} \arctan\sqrt{\frac{\gamma-1}{\gamma+1}(M^2-1)} - \arctan\sqrt{M^2-1} \tag{3.18}$$

The expression may be integrated between two states before and after expansion to yield

$$\theta_w = \upsilon(M_2) - \upsilon(M_1) \tag{3.19}$$

θ_w is a positive amount by which the flow is turned by the Prandtl-Meyer expansion.

Given the upstream Mach number M_1 and θ_w, the downstream Mach number M_2 can be obtained from Equation 3.19. Since the expansion is isentropic, the downstream static temperature, presure and density can be obtained from Equations (3.20), (3.21) and (3.22), respectively.

$$T_O = T[1 + \frac{(\gamma-1)}{2}M^2] \tag{3.20}$$

$$p_O = p[1 + \frac{\gamma - 1}{2} M^2]^{\gamma/(\gamma-1)} \tag{3.21}$$

$$\rho_O = \rho[1 + \frac{\gamma - 1}{2} M^2]^{1/(\gamma-1)} \tag{3.22}$$

The variables with subcript O are the parameters in the stagnation point.

A sketch of the theoretical solution is shown in Figure 3.6.

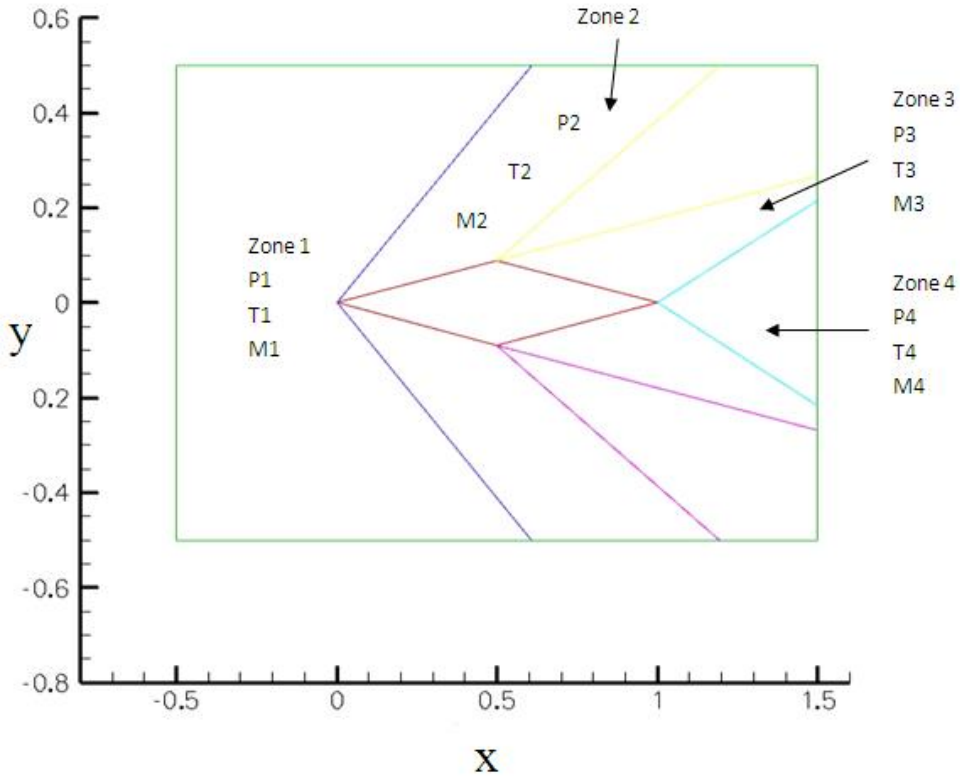

Figure 3.6: Theoretical solution with no energy deposition

The theoretical solution and the numerical solution are shown in Tables 3.1 and 3.2.

When compared with the results of Table 3.1 and 3.2, the theoretical solution and numerical solution show close agreement. This indicates that the computed results have enough accuracy and correctness. In region 2, the static pressure, static temperature and Mach number are within 1% of the theoretical values. In region 3, the static pressure, static temperature and Mach number are within 1.2% of the theoretical values. In region 4, the static pressure, static temerature and Mach number are within 1% of the theoretical values.

Table 3.1: Theoretical solution

Mach number	Pressure	Temperature
$M_1 = 2$	$P_1 = 101325Pa$	$T_1 = 300K$
$M_2 = 1.641$	$P_2 = 172919.061Pa$	$T_2 = 351.045K$
$M_3 = 2.371$	$P_3 = 55854.375Pa$	$T_3 = 254.178K$
$M_4 = 1.974$	$P_4 = 101619.711Pa$	$T_4 = 303.454K$
$\frac{M_2}{M_1} = 0.821$	$\frac{P_2}{P_1} = 1.707$	$\frac{T_2}{T_1} = 1.170$
$\frac{M_3}{M_1} = 1.186$	$\frac{P_3}{P_1} = 0.551$	$\frac{T_3}{T_1} = 0.847$
$\frac{M_4}{M_1} = 0.987$	$\frac{P_4}{P_1} = 1.003$	$\frac{T_4}{T_1} = 1.012$

Table 3.2: Numerical solution

Mach number	Pressure	Temperature
$M_1 = 2$	$P_1 = 101325Pa$	$T_1 = 300K$
$M_2 = 1.637$	$P_2 = 174666.031Pa$	$T_2 = 352.122K$
$M_3 = 2.390$	$P_3 = 55135.952Pa$	$T_3 = 254.562K$
$M_4 = 1.971$	$P_4 = 102630.117Pa$	$T_4 = 302.421K$
$\frac{M_2}{M_1} = 0.819$	$\frac{P_2}{P_1} = 1.724$	$\frac{T_2}{T_1} = 1.174$
$\frac{M_3}{M_1} = 1.195$	$\frac{P_3}{P_1} = 0.544$	$\frac{T_3}{T_1} = 0.849$
$\frac{M_4}{M_1} = 0.986$	$\frac{P_4}{P_1} = 1.013$	$\frac{T_4}{T_1} = 1.008$

Chapter 4

Results

4.1 Results for the Numerical Simulation without Energy Deposition in the Inlet Boundary

4.1.1 Parameters of Flow Field Analysis

In this type of case, the whole flowfield in the domain is studied. No filament was added in the simulation. Figures 4.1, 4.2 and 4.3 show Mach number, pressure and temperature variations with time beginning with a uniform flow initial condition throughout the flowfield. It can be seen that the first shock wave, Prandtl-Meyer expansion, and the second shock wave are formed. The enlarged density contours with instantaneous streamlines and numerical schlieren are shown in Figures 4.4 and 4.5.

In the contour figures, Mach number, pressure, temperature vary significantly due to the shock wave and expansion. With the observation in the contours, we can conclude that:

1. The first oblique shock is formed at the front point of the diamond-shaped airfoil body with the flow.
2. The expansion fan is formed over the corner of the diamond-shaped airfoil.
3. The second oblique shock is formed at the end point of the diamond-shaped airfoil.
4. The Mach number decreases after the shock wave and increases through the expansion.
5. Pressure and temperature are just the contrary, i.e., increasing after the shock, and then decreasing in the expansion.
6. The numerical results of Mach number, pressure, temperature agree with the theoretical results (Chapter 3.6).

7. In the numerical schlieren contour, there are an obvious "X"-shaped and bar-shaped white colour shadow. They represent weak waves reflected from the upper and lower boundaries. However, it is evident that these waves do not impinge upon the airfoil, and therefore do not affect the calculation of the drag coefficient.

4.1.2 Drag Coefficient Analysis

The airfoil drag coefficient is an important performance index. According to the nondimensionlized numerical simulation in this research, the drag coefficient is analyzed. Figure 4.6 shows a schematic of the drag force on the airfoil. As a first step of analysis, the accuracy of the drag coefficient prediction is analyzed. The variables p_2 and p_3 are the pressures after the first shock wave and after the expansion on the airfoil, respectively (Figure 3.6). According to the analysis above (Chapter 4.1.1), p_2 is greater than p_3, thus generating a drag force. In FLUENT, the calculation method for drag coefficient is Equation (4.1), which is the same method used in the theoretical result.

$$\begin{aligned} C_d &= \frac{\text{drag force}}{\frac{1}{2}\rho_\infty U_\infty^2 c} \\ &= \frac{p_2(\frac{t}{2})*2 - p_3(\frac{t}{2})*2}{\frac{1}{2}\rho_\infty U_\infty^2 c} \\ &= \frac{(p_2 - p_3)t}{\frac{1}{2}\rho_\infty U_\infty^2 c} \\ &= \frac{p_\infty(\frac{p_2}{p_\infty} - \frac{p_3}{p_\infty})t}{\frac{1}{2}\rho_\infty U_\infty^2 c} \\ &= \frac{2}{\gamma M_\infty^2}\frac{t}{c}(\frac{p_2}{p_\infty} - \frac{p_3}{p_\infty}) \end{aligned} \tag{4.1}$$

The theoretical drag coefficient is shown in Table 4.1, and Figure 4.7. Figure 4.7 indicates that drag coefficient decreases with increasing Mach number. The calculated result for Mach = 2 flow using the FLUENT code is:

$$\text{drag coefficient} = 0.0742$$

The accuracy of the numerical results for drag coefficient (Mach 2, without filament):

$$(0.0742 - 0.0728)/0.0728 = 0.019 \tag{4.2}$$

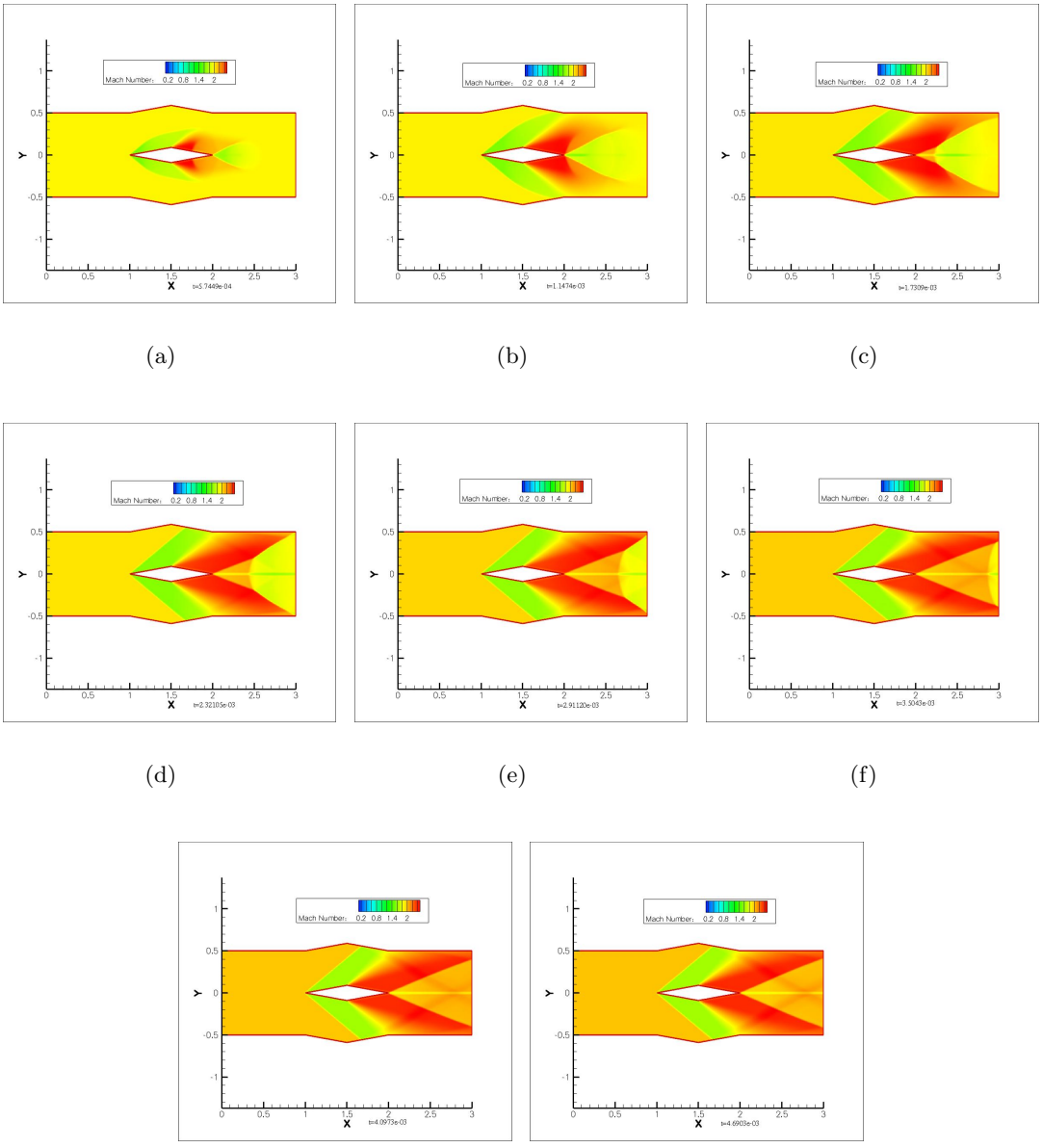

(a) (b) (c)

(d) (e) (f)

(g) (h)

Figure 4.1: Eight Mach number contours for process of simulation case without energy deposition

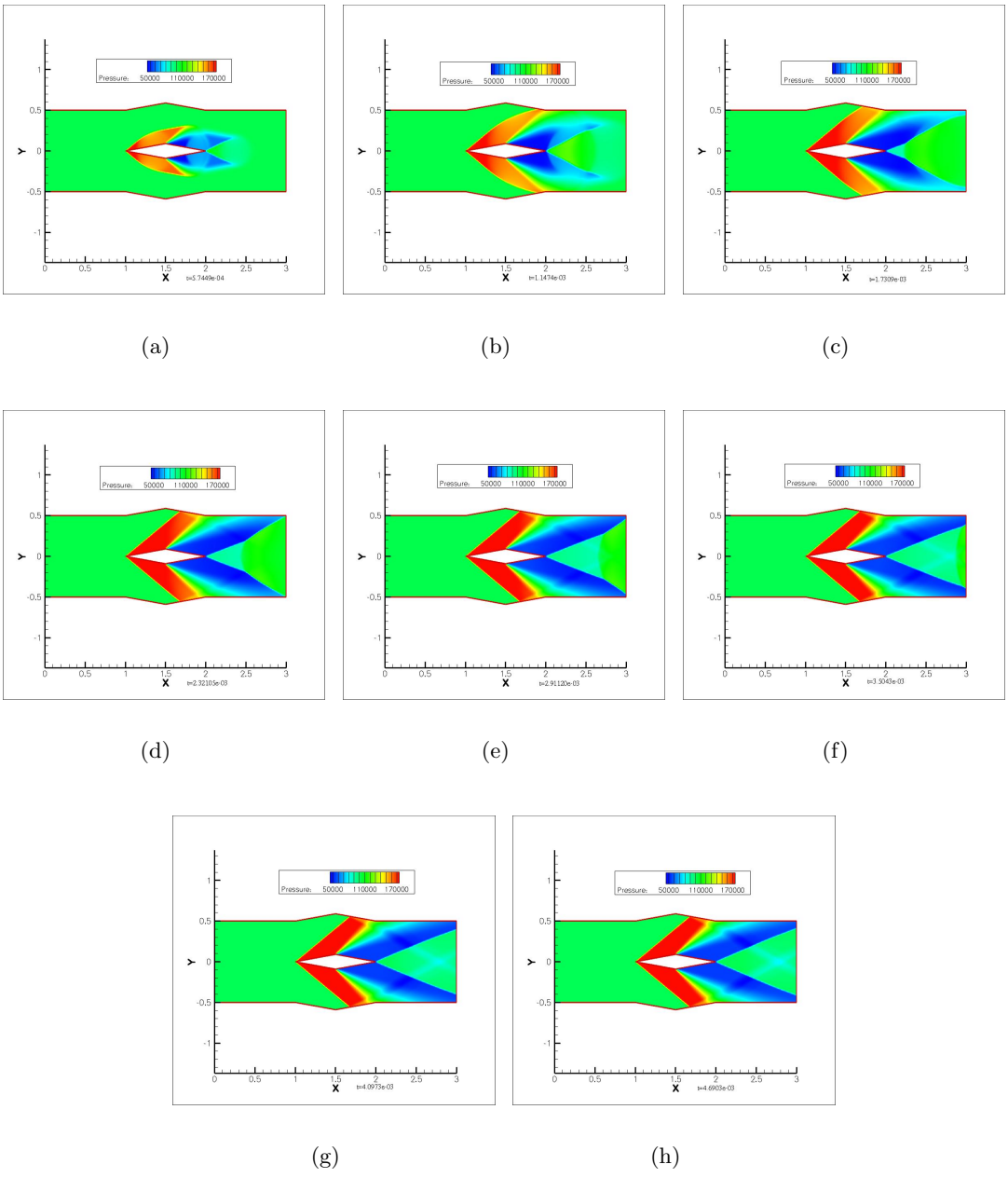

(a) (b) (c)

(d) (e) (f)

(g) (h)

Figure 4.2: Eight pressure contours for process of simulation case without energy deposition

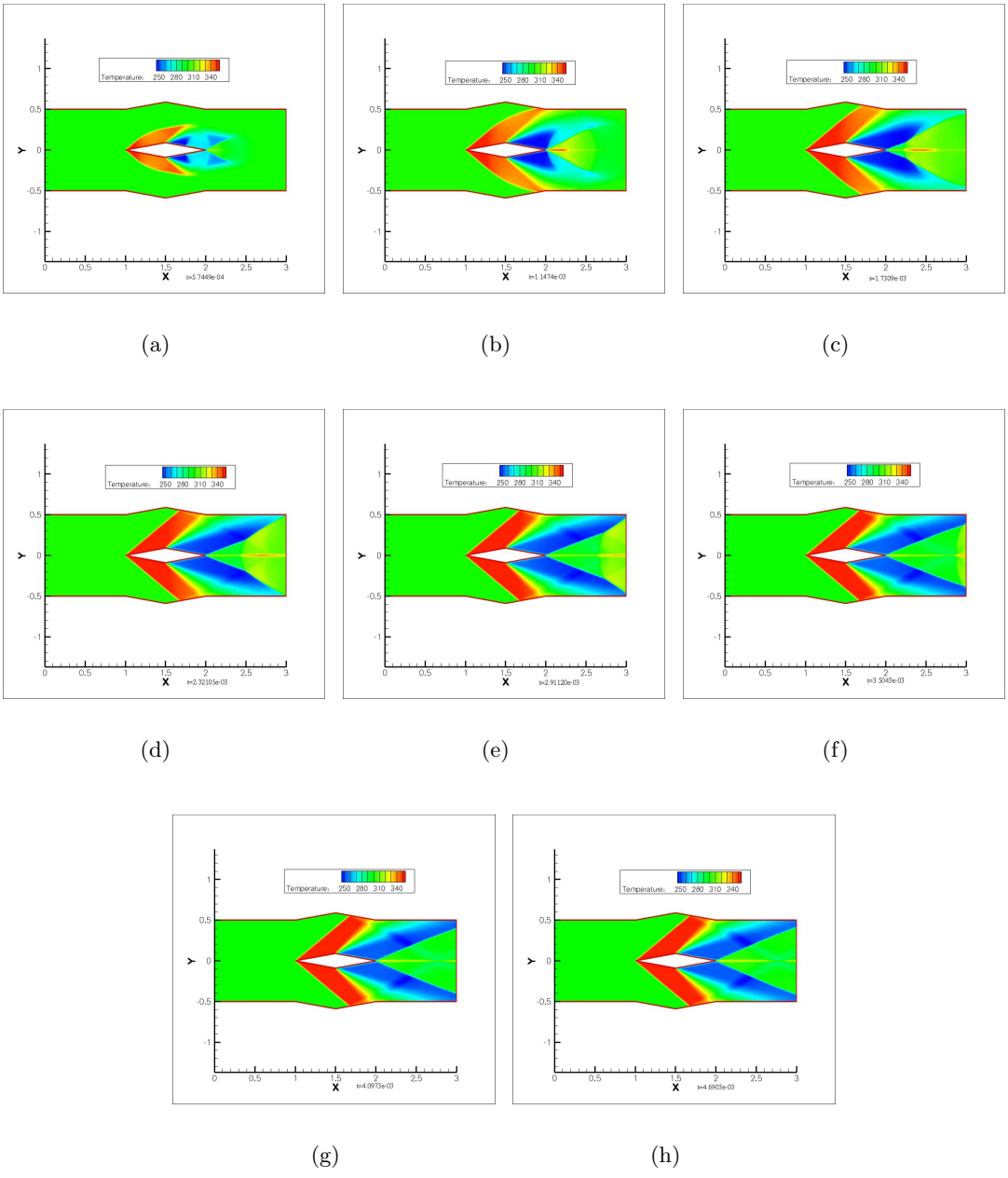

(a) (b) (c)

(d) (e) (f)

(g) (h)

Figure 4.3: Eight temperature contours for process of simulation case without energy deposition

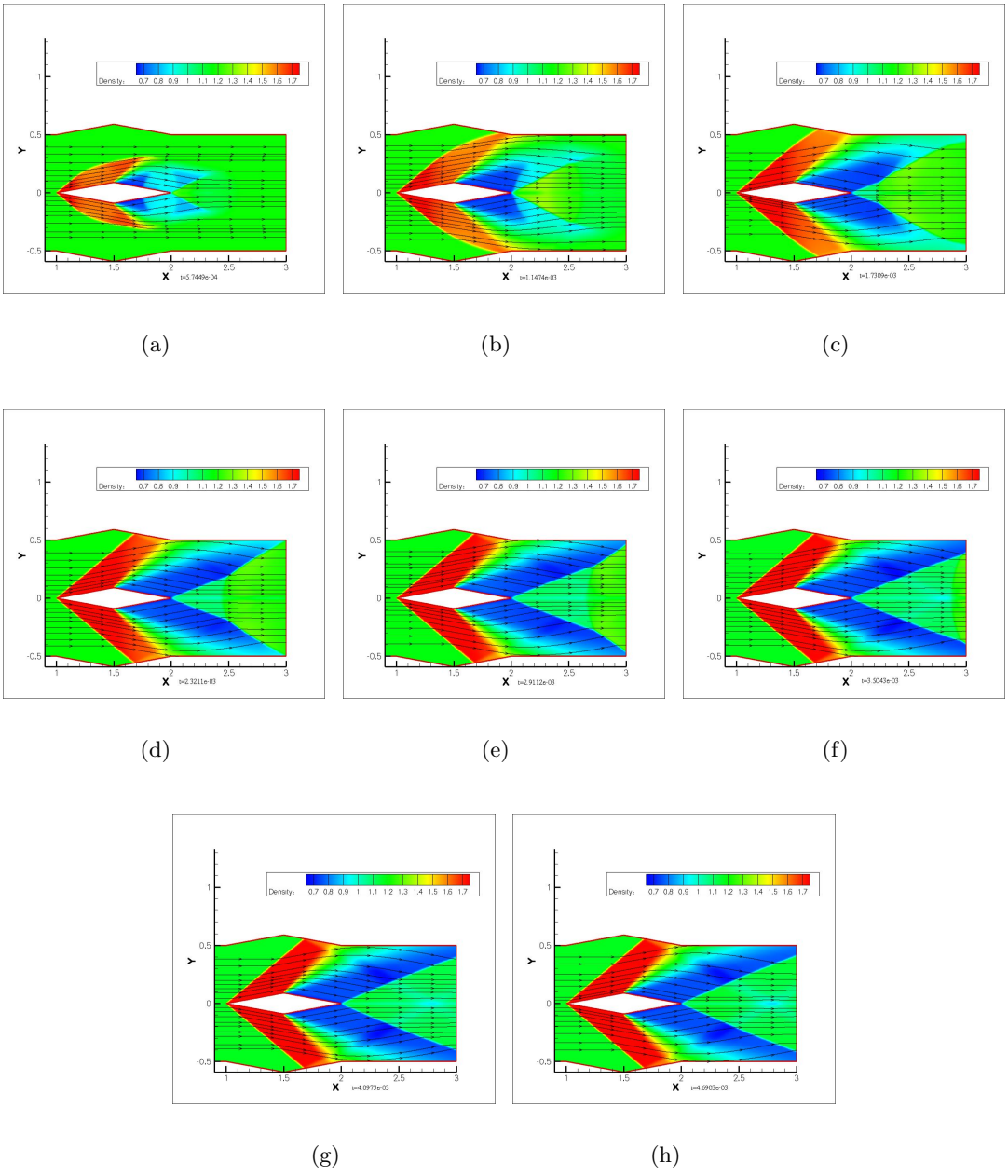

(a) (b) (c)

(d) (e) (f)

(g) (h)

Figure 4.4: Eight enlarged density contours for process of simulation case without energy deposition

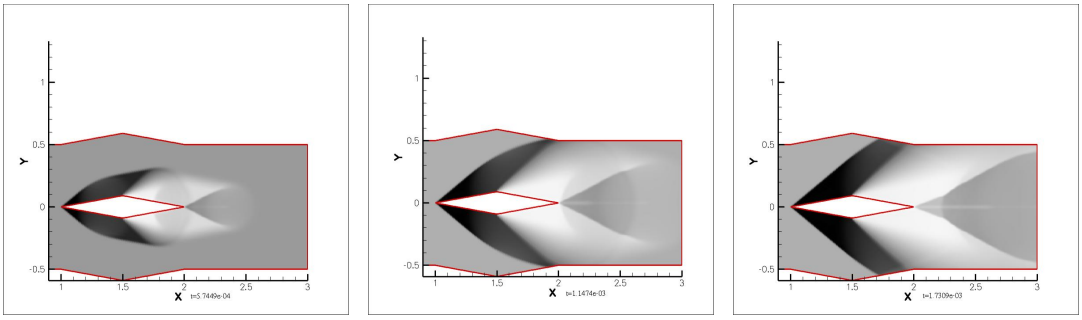

(a) (b) (c)

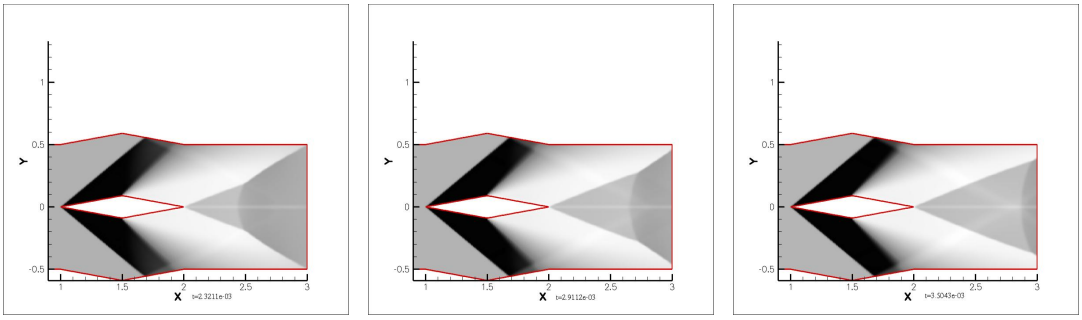

(d) (e) (f)

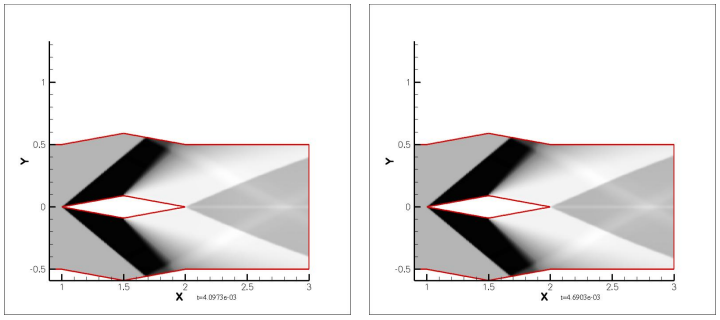

(g) (h)

Figure 4.5: Eight enlarged numerical schlieren contours for process of simulation case without energy deposition

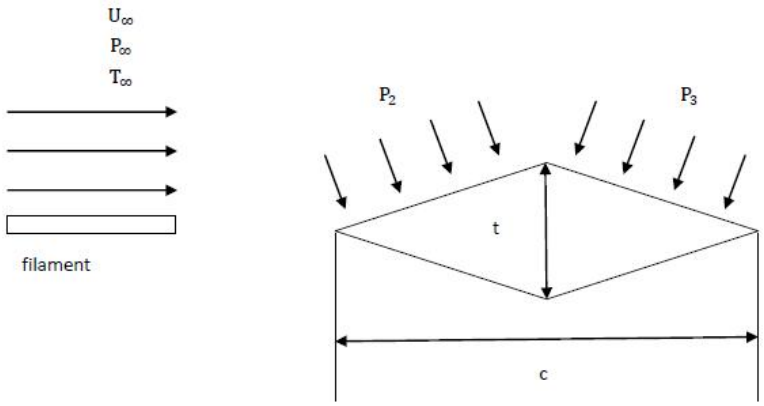

Figure 4.6: Schematic sketch of drag force distribution on the airfoil

Table 4.1: Theoretical results of drag coefficient

Mach number	drag coefficient
1.44	0.1376
1.45	0.1331
1.47	0.1265
1.5	0.1192
1.55	0.1102
1.60	0.1032
1.65	0.0975
1.70	0.0926
1.75	0.0883
1.80	0.0845
1.85	0.0812
1.90	0.0781
1.95	0.0753
2.00	0.0728
2.05	0.0704
2.10	0.0683

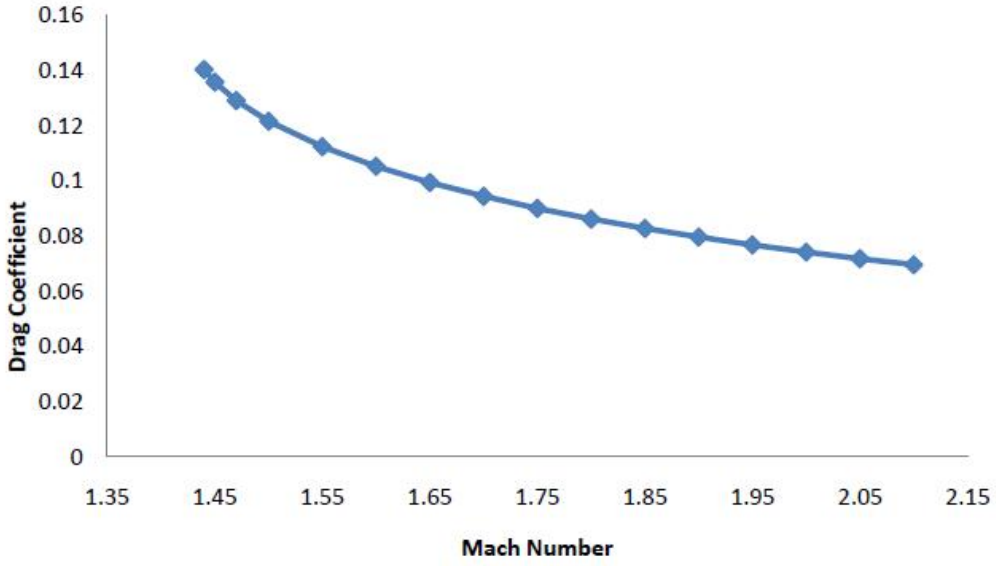

Figure 4.7: Theoretical drag coefficient (no filament)

From Equation (4.2), the accuracy of numerical calculation is within 2%. This is considered acceptable for this research since energy deposition would need to achieve an order of magnitude larger change on drag coefficient to be considered effective. In other words, we are looking to see if we can achieve drag coefficient reduction of 20% of more by the pulsed filament.

In the cases with filaments added, the same numerical methods and the grid are used with the case without filaments. The drag coefficient in the cases with filaments is estimated to be accurate within 2%.

4.2 Infinitely Long Symmetric Filament

4.2.1 Parameters of Flow Field Analysis

Table 4.2: Infinitely Long Symmetric Filament

Type Description	$\frac{d}{t}$	$\frac{l}{t}$	$\frac{L}{t}$	$\frac{h}{t}$
infinitely long symmetric filament	0.10 0.25 0.50 1.00	∞	n/a	0

The results presented in this section are the four cases with infinitely long symmetric symmetric filament of different heights ($\frac{d}{t} = 0.10, 0.25, 0.50, 1.00$). The evolution of the flow is examined by the Mach number, pressure, temperature, density field along with numerical schlieren images (Figures 4.8 to 4.27).

4.2.2 Case 1 ($\frac{d}{t} = 0.10$)

Figures 4.8 to 4.12 show the main regions of the flow development in time, which are similar to Figures 4.1 to 4.5:

1. The first shock is formed at the front point of the diamond-shaped airfoil body with the flow.
2. The expansion fan is formed over the corner of the diamond-shaped airfoil.
3. The second shock is formed at the end point of the diamond-shaped airfoil.
4. Mach number will decrease after the shock wave and increases through the expansion.
5. Pressure and temperature are just on the contrary, increasing after the shock, and then decreasing in the expansion.

The infinitely long symmetric filament with $\frac{d}{t} = 0.10$ can be seen in Figures 4.8 to 4.12 except in Figure 4.9. The filament passes over the diamond-shaped airfoil as can be observed clearly in Figure 4.12. And the changes in the regions of filament can be concluded:

1. Mach number will decrease after the shock wave and increases through the expansion in the filament region.
2. Pressure and temperature are just on the contrary, increasing after the shock, and then decreasing in the expansion in the filament.
3. The progressive contact formed where two flows of different density and temperature meet.

Overall, the filament has a very small effect on the flowfield compared to the no filament case. Tecplot is used to get all the figures in this thesis. Tecplot generates all the figures

with colour continuing. So it's the reason why there is pregresive contact formed between the filament and freestream flow. In the case $\frac{d}{t} = 0.10$ case, the filament is too thin to see the center part of filament, thus, the temperature of the filament looks lower than $600K$. And colour bar is more helpful to find the temperature of the filament.

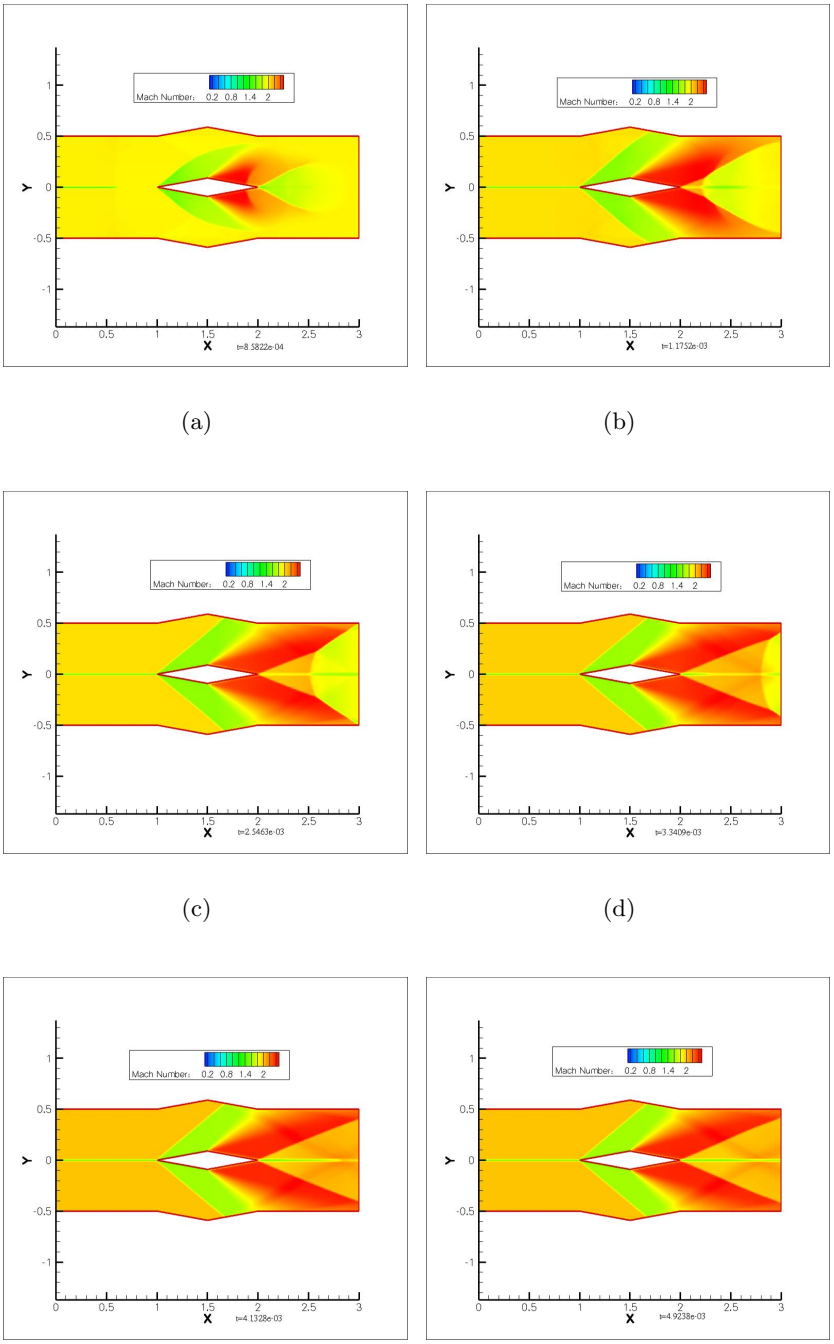

(a) (b)

(c) (d)

(e) (f)

Figure 4.8: Six Mach number contours for the flow simulation with the infinitely long symmetric filament ($\frac{d}{t} = 0.10$)

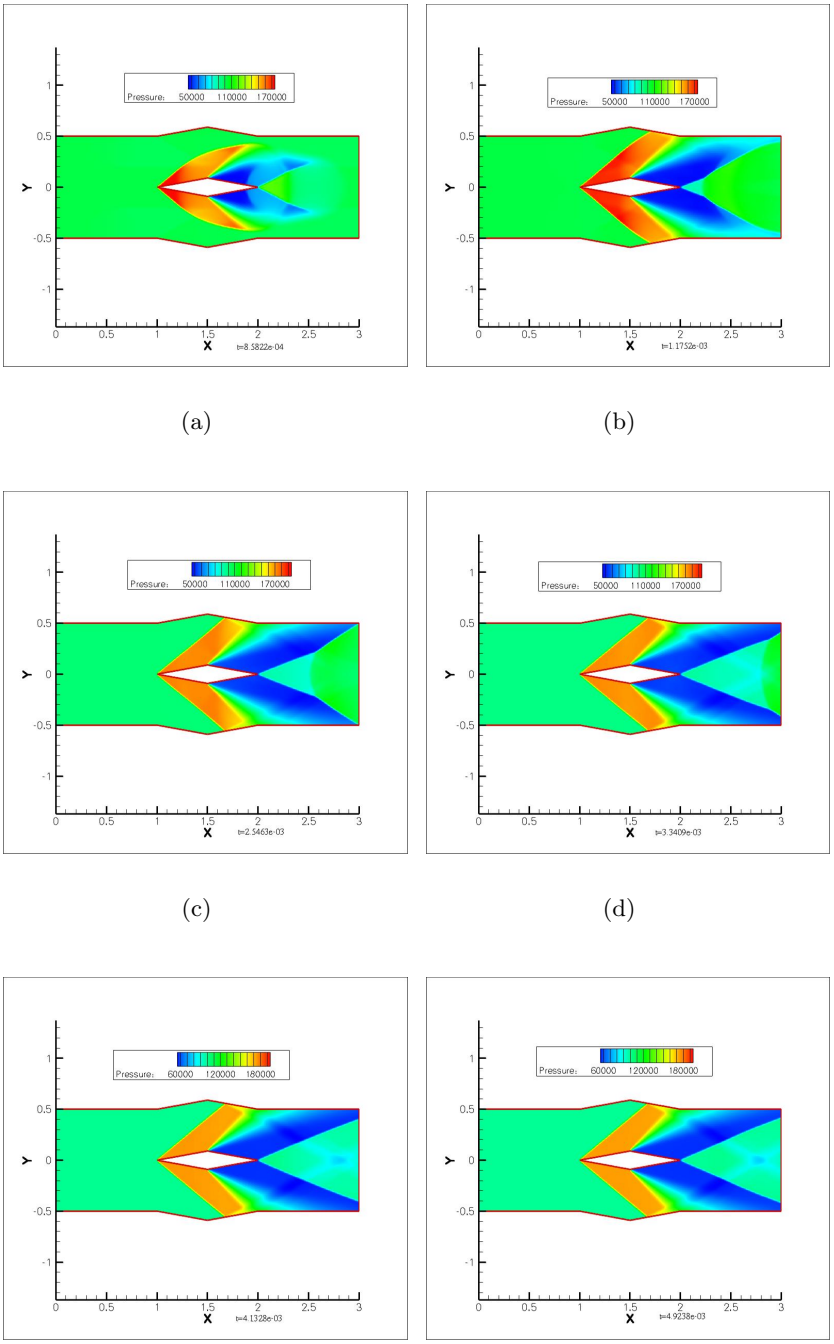

(a) (b)

(c) (d)

(e) (f)

Figure 4.9: Six pressure contours for the flow simulation with the infinitely long symmetric filament ($\frac{d}{t} = 0.10$)

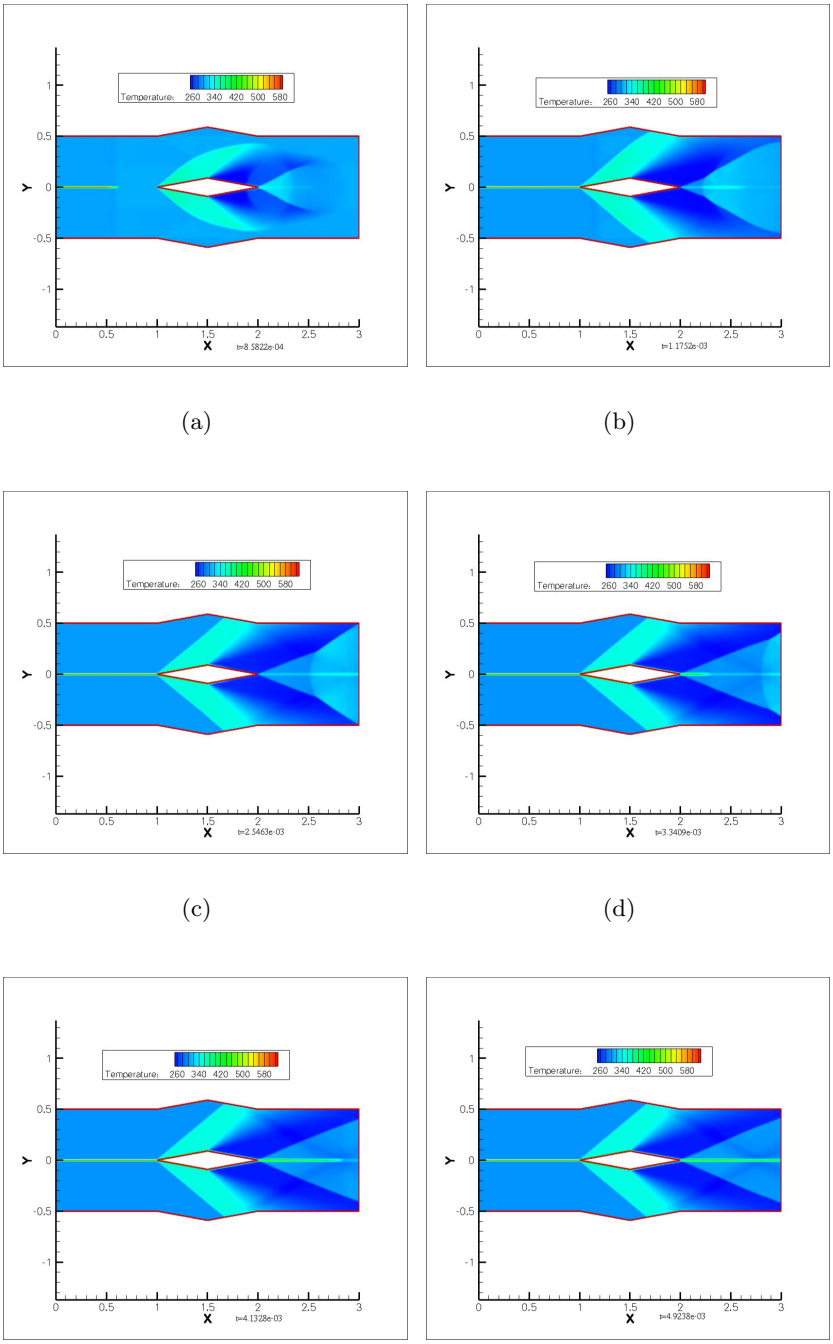

(a) (b)

(c) (d)

(e) (f)

Figure 4.10: Six temperature contours for the flow simulation with the infinitely long symmetric filament ($\frac{d}{t} = 0.10$)

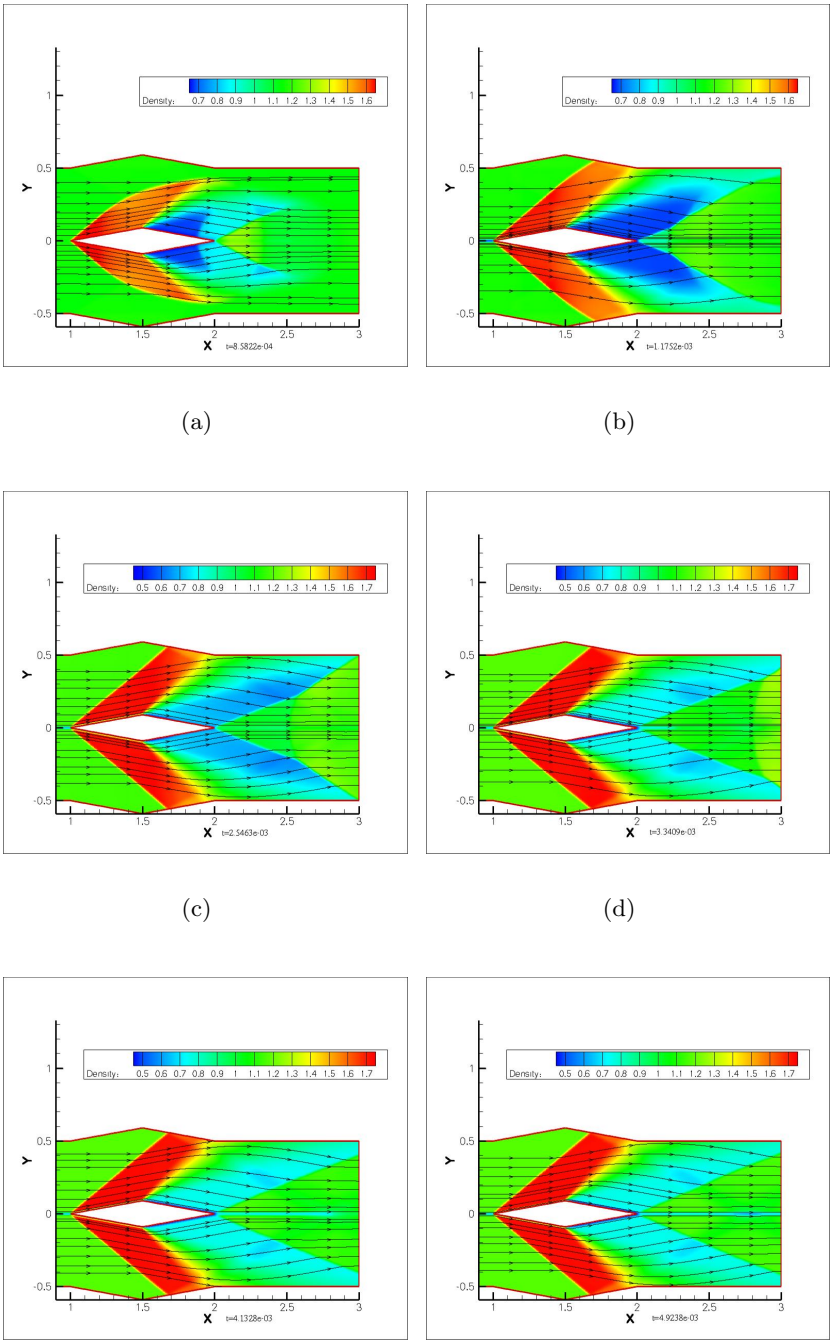

(a) (b)

(c) (d)

(e) (f)

Figure 4.11: Six enlarged density contours for the flow simulation with the infinitely long symmetric filament ($\frac{d}{t} = 0.10$)

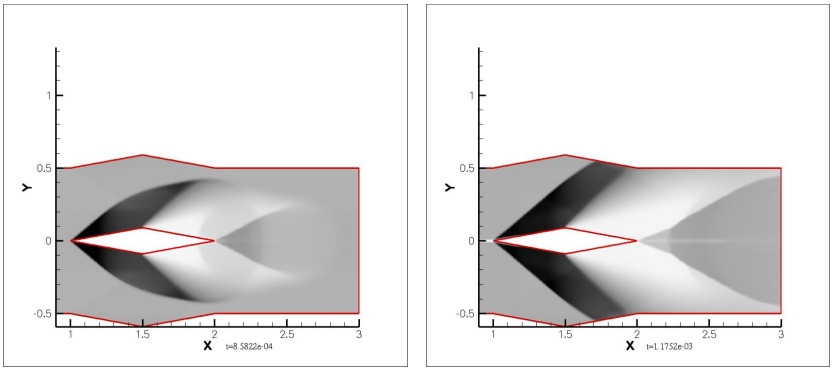

(a) (b)

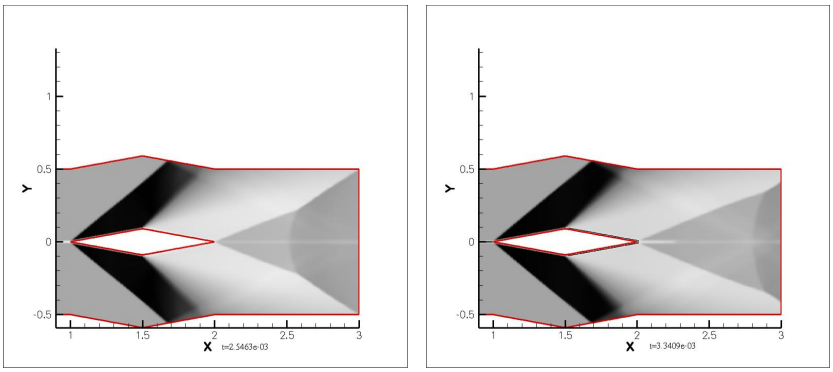

(c) (d)

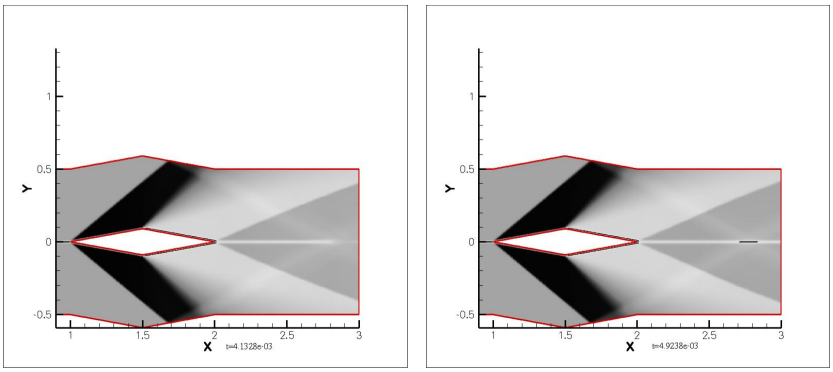

(e) (f)

Figure 4.12: Six enlarged density contours for the flow simulation with the infinitely long symmetric filament ($\frac{d}{t} = 0.10$)

4.2.3 Case 2 ($\frac{d}{t} = 0.25$)

In Figures 4.13 to 4.17, the results with infinitely long symmetric filament with $\frac{d}{t} = 0.25$ are described. The analysis of main regions of flow and filament can be concluded to be similar to Chapter 4.2.2. The filament is broader in this case, so the phenomenon is more evident. The filament height increases across the expansion (point N and P in Figure 3.4) and decreases across the trailing edge shock (point O in Figure 3.4).

4.2.4 Case 3 ($\frac{d}{t} = 0.50$)

In Figures 4.18 to 4.22, the results with infinitely long symmetric filament with $\frac{d}{t} = 0.50$ are described. The conclusion obtained in Chapter 4.2.2 and Chapter 4.2.3 are verified again here. In Figure 4.22, the first oblique shock wave almost changing to the normal shock in the filament region is observed. From NACA 1135, for $M_f = 1.414$ (Table 2.4) and $\delta = 10°$, there is no attached shock possible. Thus, a normal shock has formed near the leading edge of the diamond-shaped airfoil. Actually, the "normal shock" would be a detached shock, but appears to be "attached" shock due to the finite size of the grid cells.

In temperature contours, the temperature bar is more clear to explain the colour change of the filament (the temperature is $600K$, but diffirence of the colour).

4.2.5 Case 4 ($\frac{d}{t} = 1.00$)

Because $\frac{d}{t} = 1.00$, the infinitely long symmetric filament is widest in this section and the results in figures are most clear. The conclusion for the interaction of infinitely long symmetric filament with the 2-D diamond-shaped airfoil as follows:

1. The first shock is formed at the front point of the diamond-shaped airfoil body with the flow.

2. The expansion fan is formed over the corner of the diamond-shaped airfoil.

3. The second shock is formed at the end point of the diamond-shaped airfoil.

4. The Mach number decreases after the shock wave and increases through the expansion both in the flow and filament region.

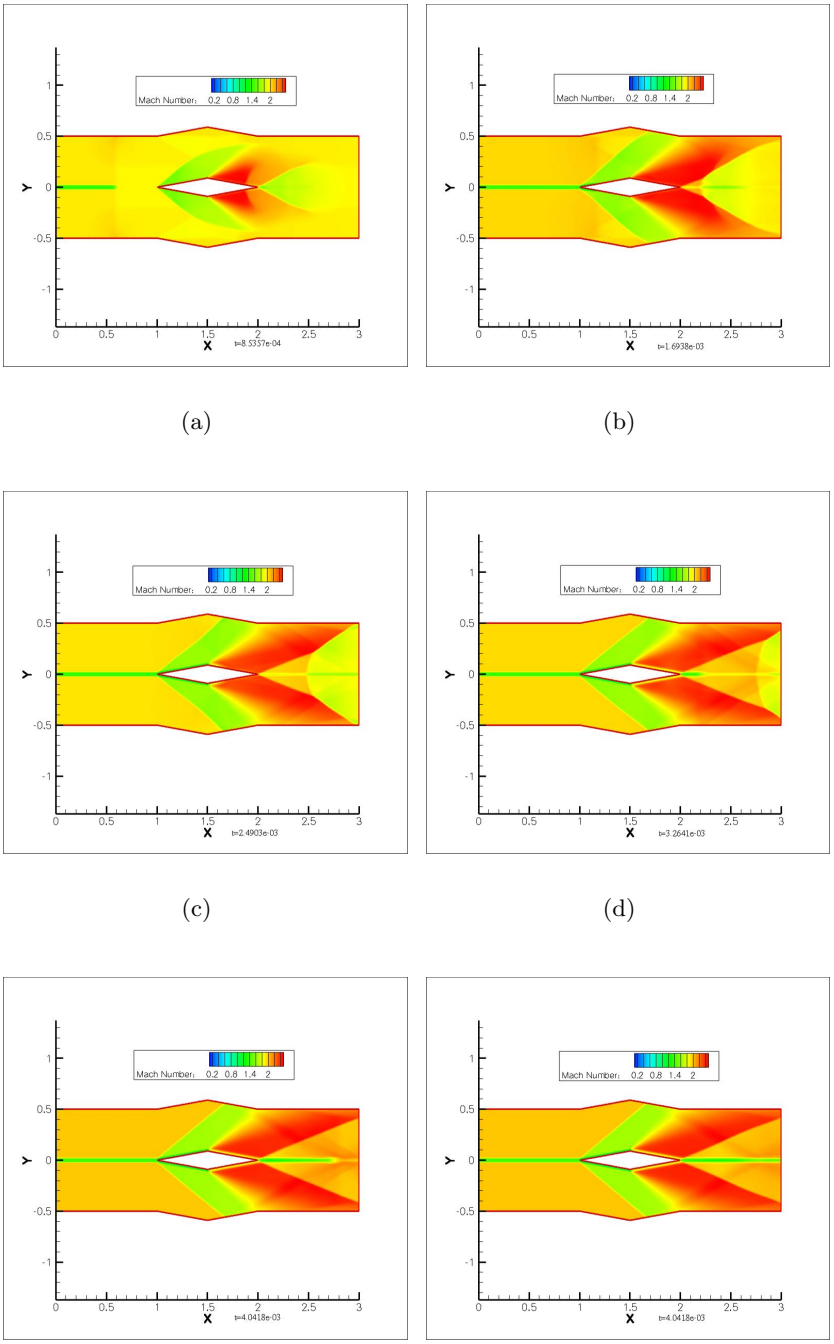

(a) (b)

(c) (d)

(e) (f)

Figure 4.13: Six Mach number contours for the flow simulation with the infinitely long symmetric filament ($\frac{d}{t} = 0.25$)

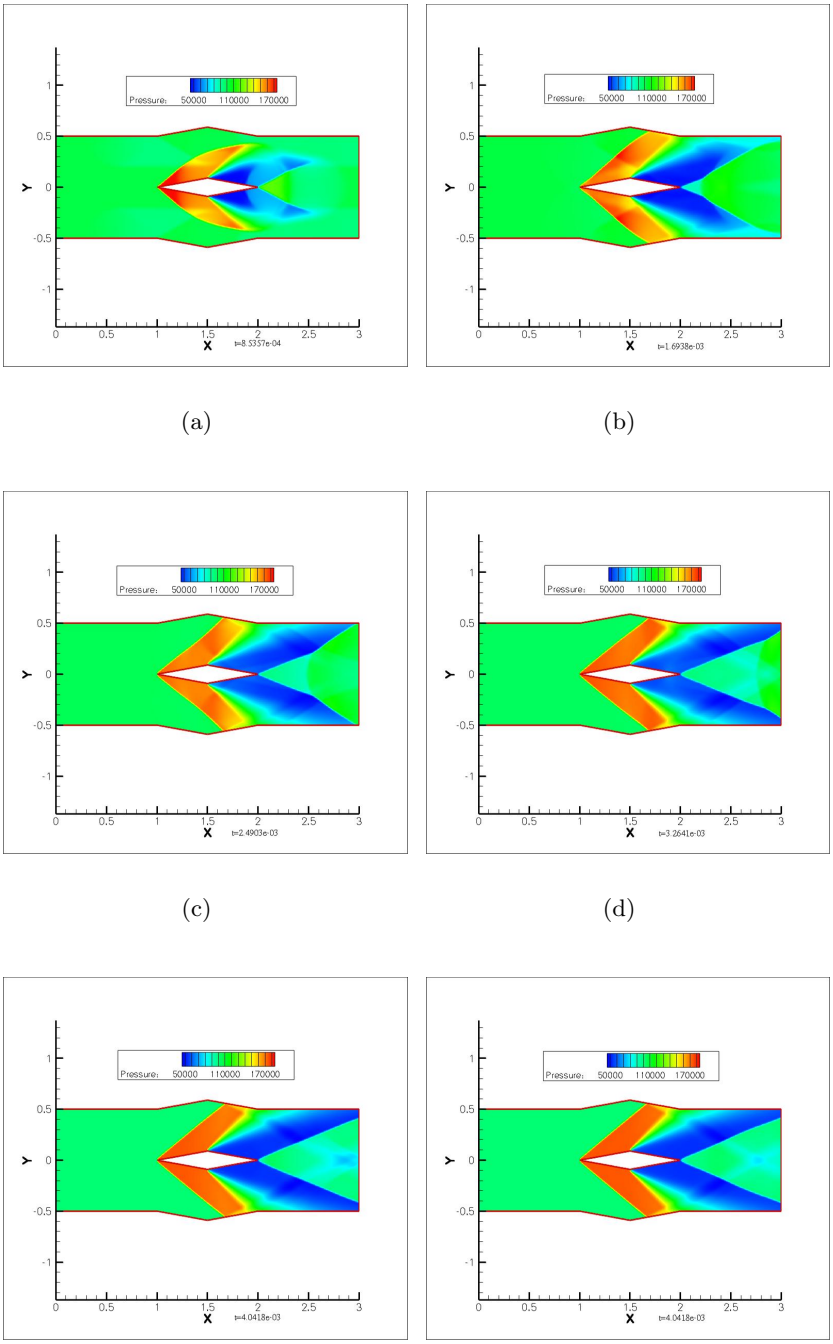

(a) (b)

(c) (d)

(e) (f)

Figure 4.14: Six pressure contours for the flow simulation with the infinitely long symmetric filament ($\frac{d}{t} = 0.25$)

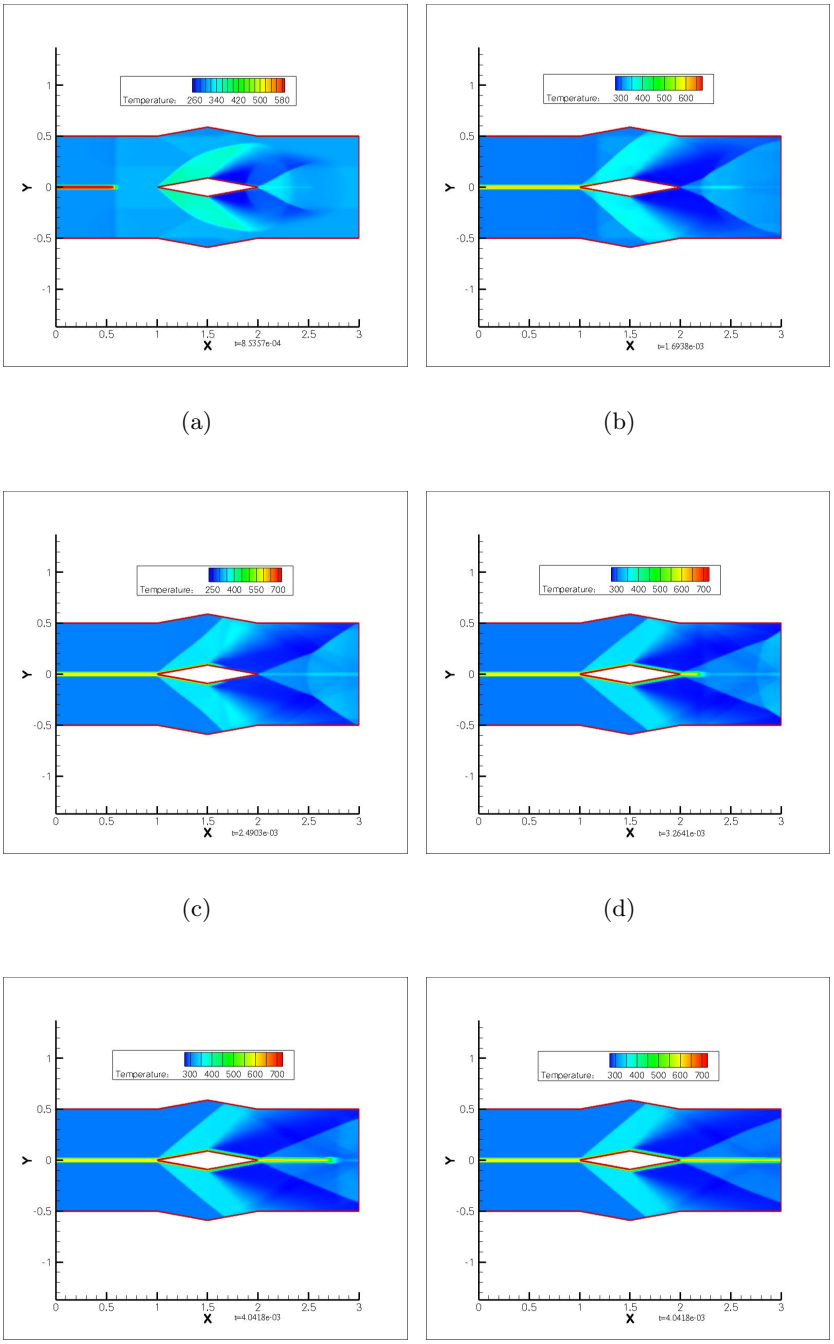

Figure 4.15: Six temperature contours for the flow simulation with the infinitely long symmetric filament ($\frac{d}{t} = 0.25$)

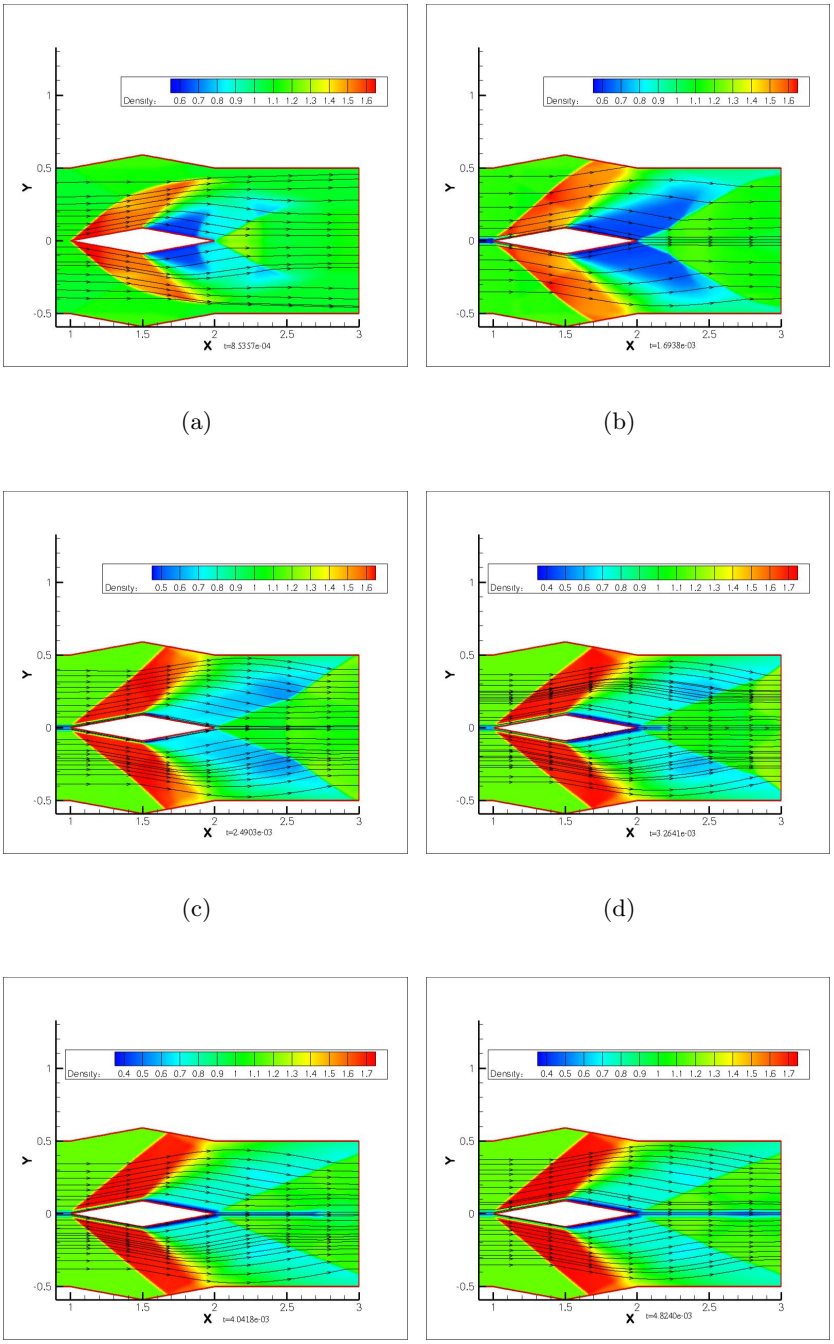

Figure 4.16: Six enlarged density contours for the flow simulation with the infinitely long symmetric filament ($\frac{d}{t} = 0.25$)

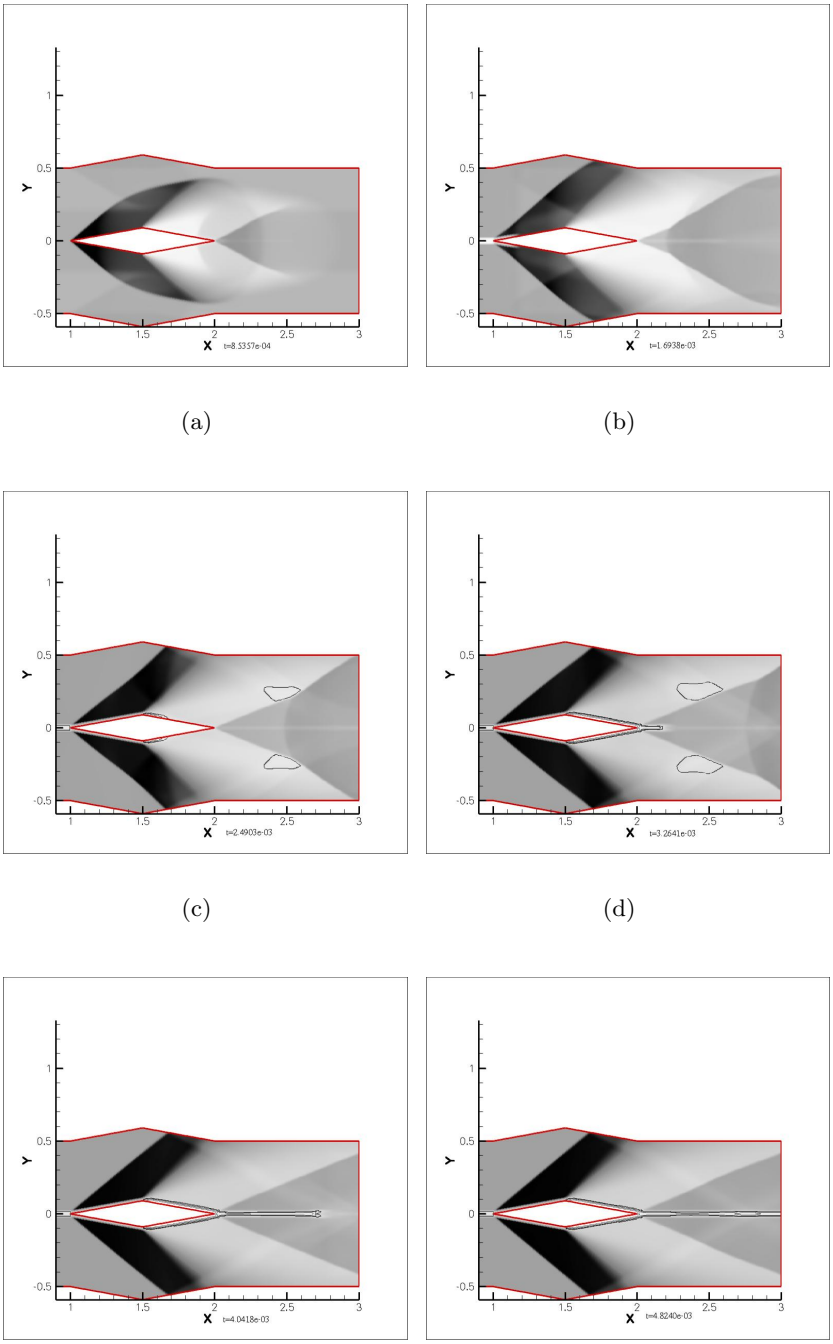

(a) (b)

(c) (d)

(e) (f)

Figure 4.17: Six enlarged numerical schlieren contours for the flow simulation with the infinitely long symmetric filament ($\frac{d}{t} = 0.25$)

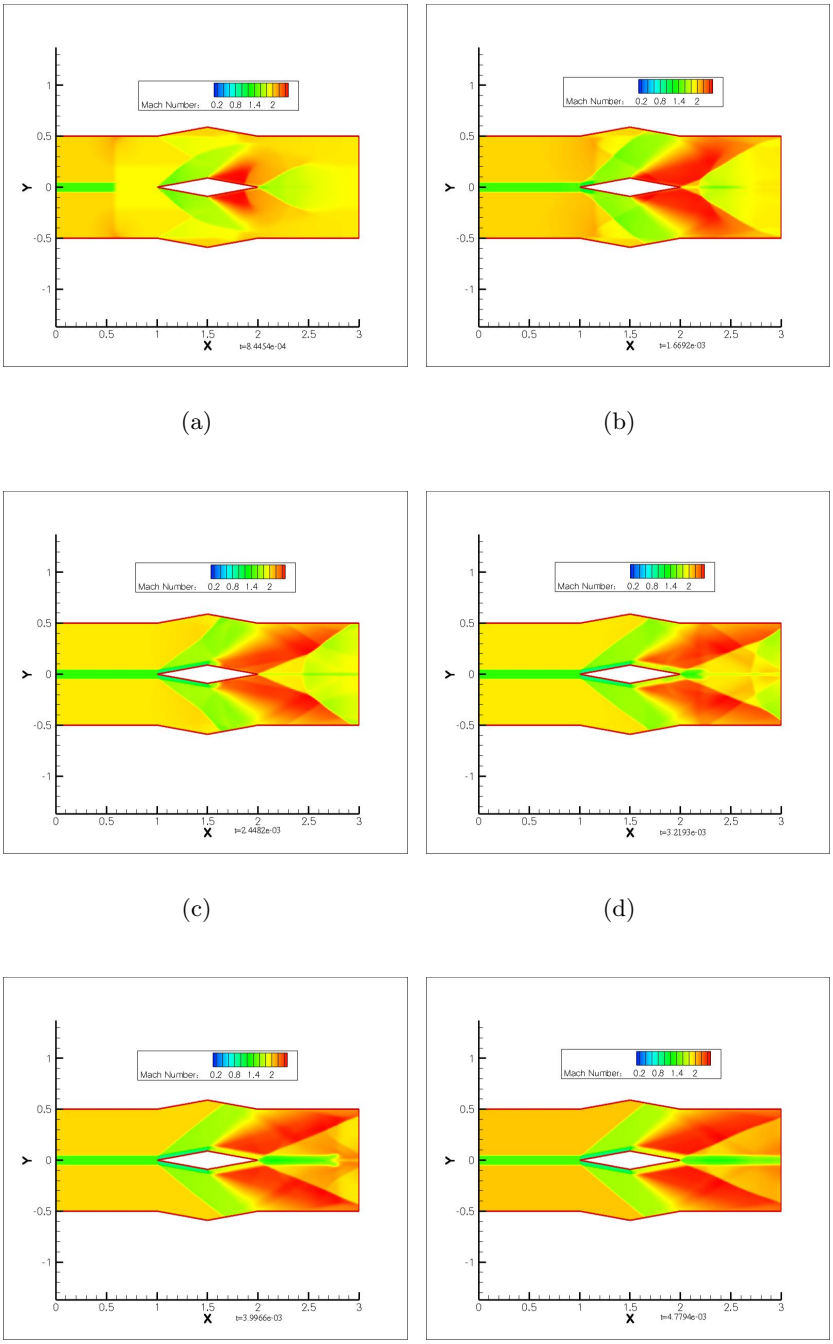

(a) (b)

(c) (d)

(e) (f)

Figure 4.18: Six Mach number contours for the flow simulation with the infinitely long symmetric filament ($\frac{d}{t} = 0.50$)

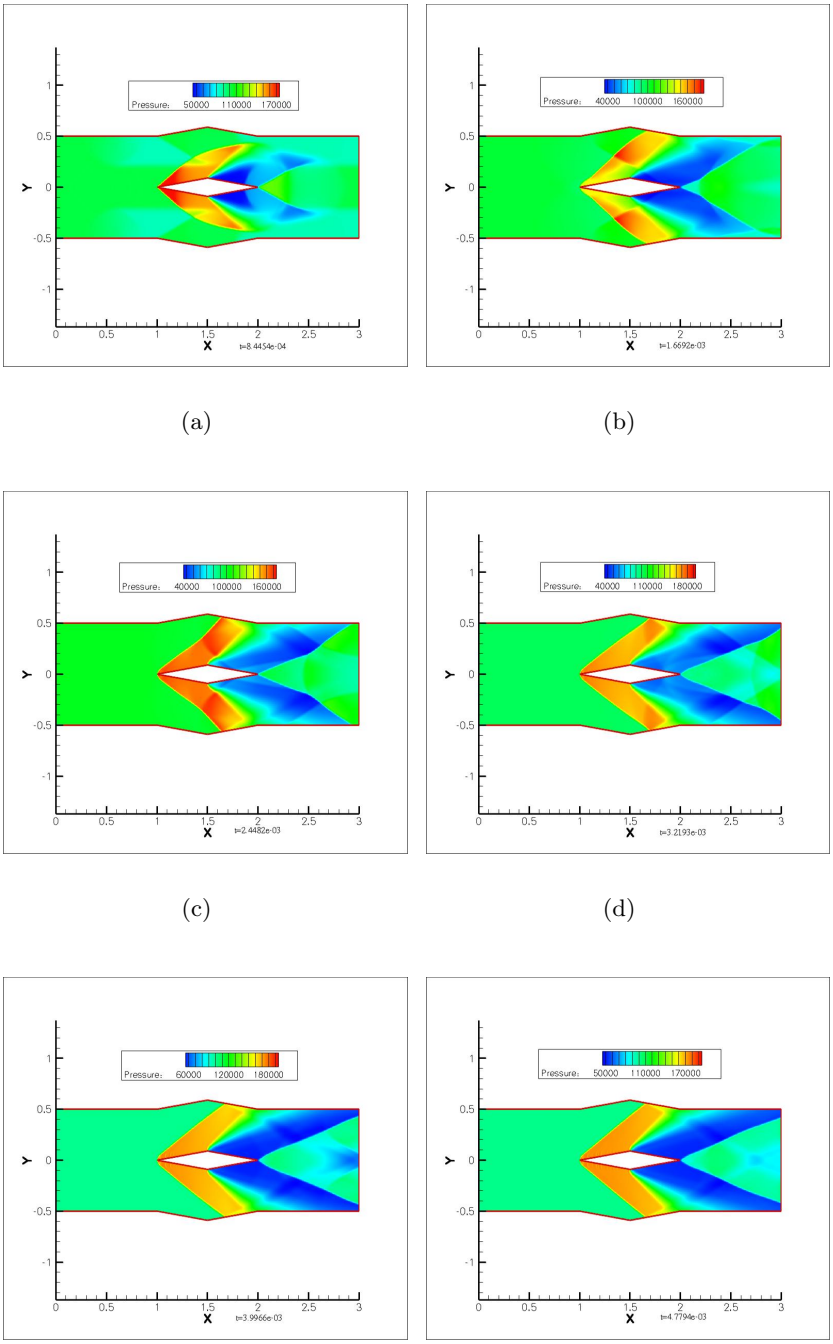

Figure 4.19: Six pressure contours for the flow simulation with the infinitely long symmetric filament ($\frac{d}{t} = 0.50$)

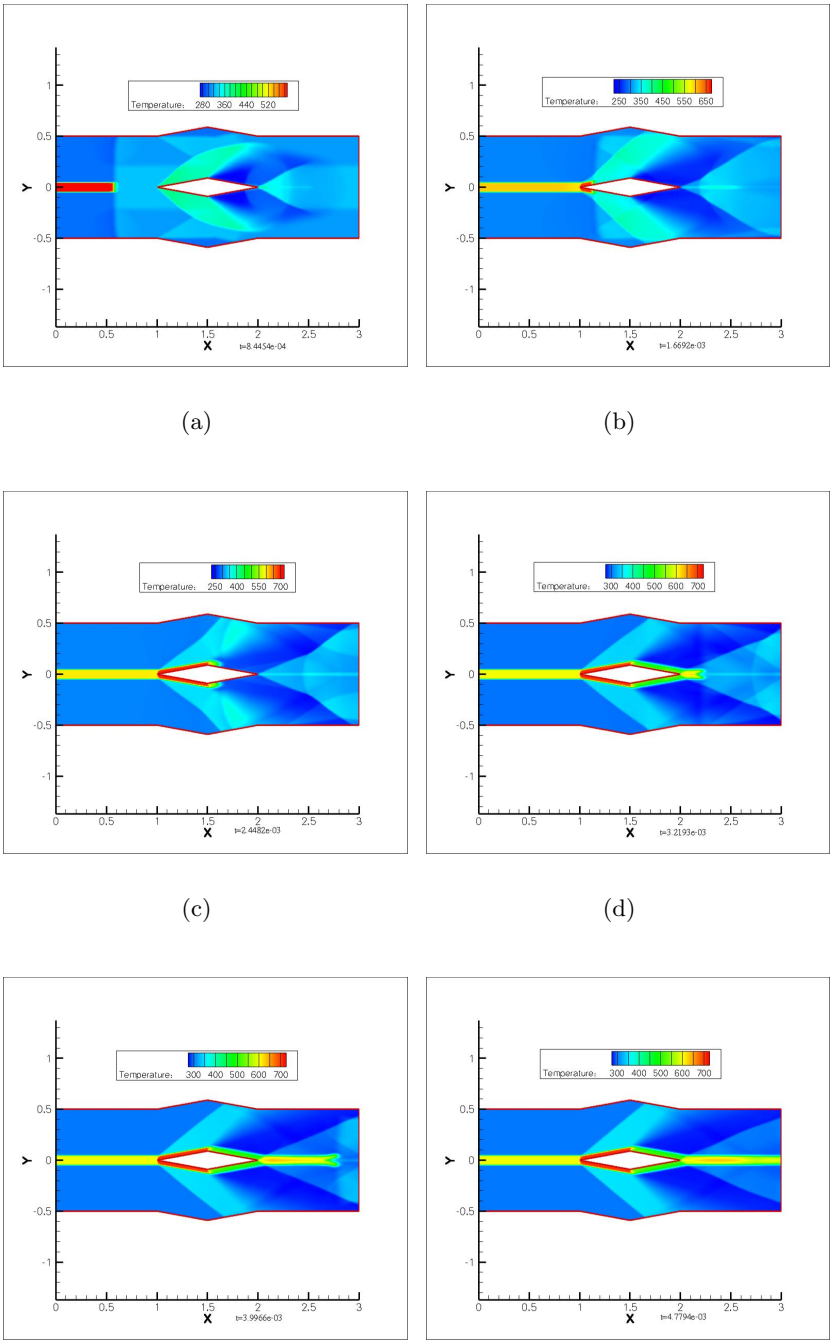

Figure 4.20: Six temperature contours for the flow simulation with the infinitely long symmetric filament ($\frac{d}{t} = 0.50$)

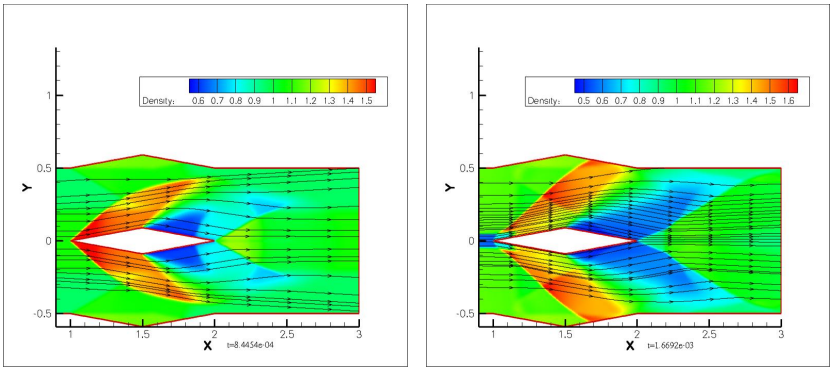

(a)

(b)

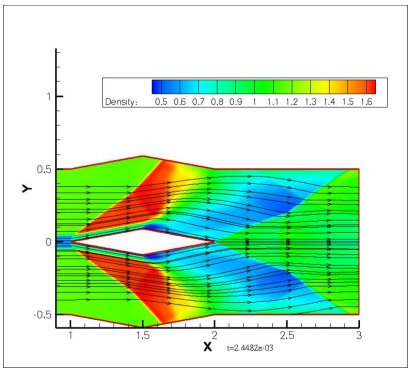

(c)

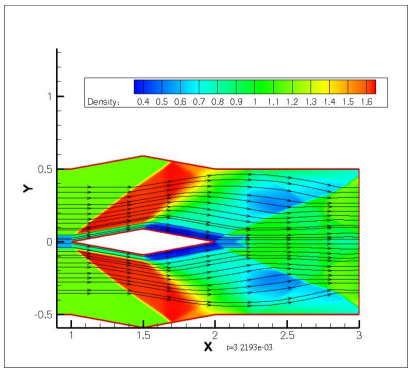

(d)

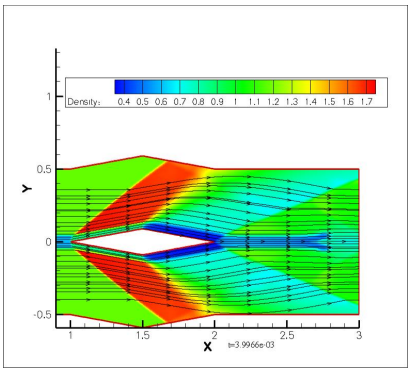

(e)

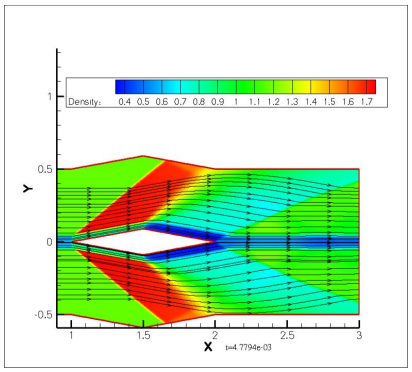

(f)

Figure 4.21: Six enlarged density contours for the flow simulation with the infinitely long symmetric filament ($\frac{d}{t} = 0.50$)

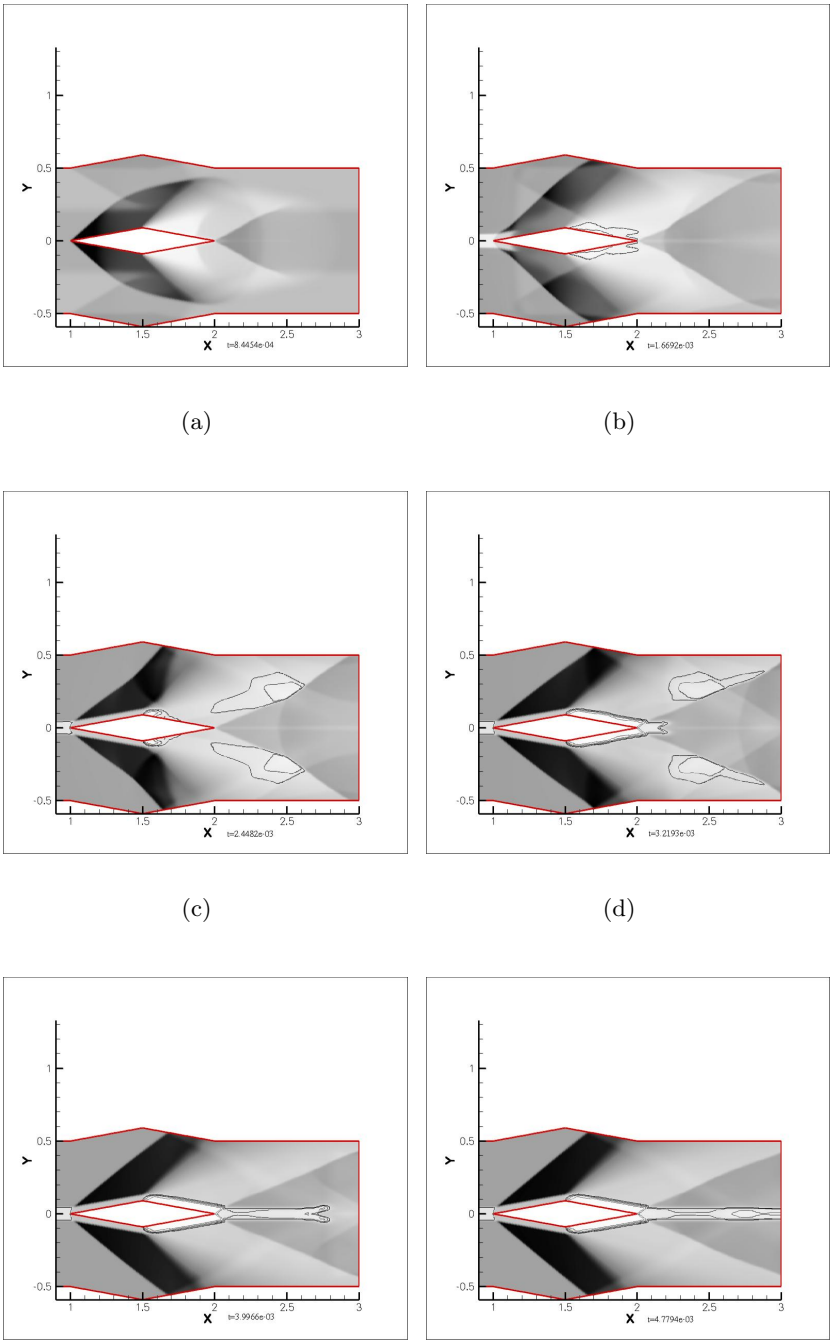

(a) (b)

(c) (d)

(e) (f)

Figure 4.22: Six enlarged numerical schilieren contours for the flow simulation with the infinitely long symmetric filament ($\frac{d}{t} = 0.50$)

5. Pressure and temperature are just on the contrary, increasing after the shock, and then decreasing in the expansion both in the flow and filament region.

6. The progressive contact formed where two flows of different density and temperature meet.

7. A concave formed gradually in the filament after the second weak shock formed because the stripping-shaped numerical error. The stripping-shaped numerical error is due to the reflection of the flow on the CD and IH boundaries.

8. An almost "normal shock" has formed near the leading edge of the diamond-shaped airfoil in the filament region. This is true for all four cases, but is apparent in the contours plots for the thicker filament only (the normal shock in the case with $\frac{d}{t} = 1.00$ is most apparent). Actually, the "normal shock" would be a detached shock, but appears to be "attached" shock due to the finite size of the grid cells.

9. The filament (in higher temperature and lower density region) makes the angle of the expansion fan bigger.

4.2.6 Drag Coefficient Analysis for Infinitely Long Symmetric Filament Added

FLUENT calculates the instantaneous drag coefficient on the airfoil. Figures 4.29 and 4.30 shows the computed results of the drag coefficient in all the four cases by the flowtime. It is observed that the drag coefficient tends to a stable value. Thus, the average value of all the drag coefficient data from 700 times to 1200 times can regarded as reasonable value for each case. Table 4.3 and Figure 4.28 show the computed results of the drag coefficient with four different types of infinitely long symmetric filaments. The table and the figure demonstrated that drag coefficient is reduced slightly within increasing filament heights; however, the variation is within the uncertainty of the numerical simulations and therefore the drag coefficient is effectively constant. The difference in average drag coefficient between the $\frac{d}{t} = 0.10$ and $\frac{d}{t} = 1.00$ cases is 3.8%.

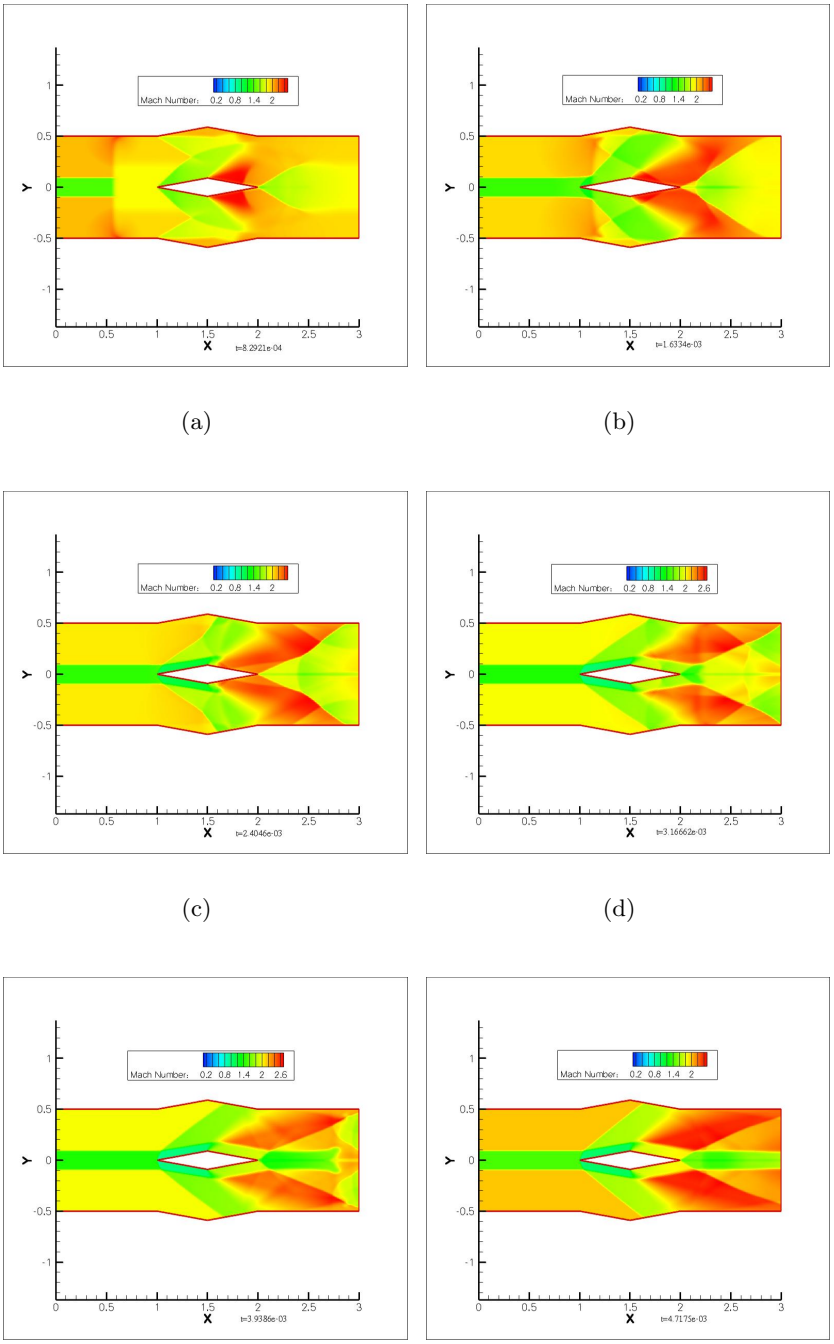

(a) (b)

(c) (d)

(e) (f)

Figure 4.23: Six Mach number contours for the flow simulation with the infinitely long symmetric filament ($\frac{d}{t} = 1.00$)

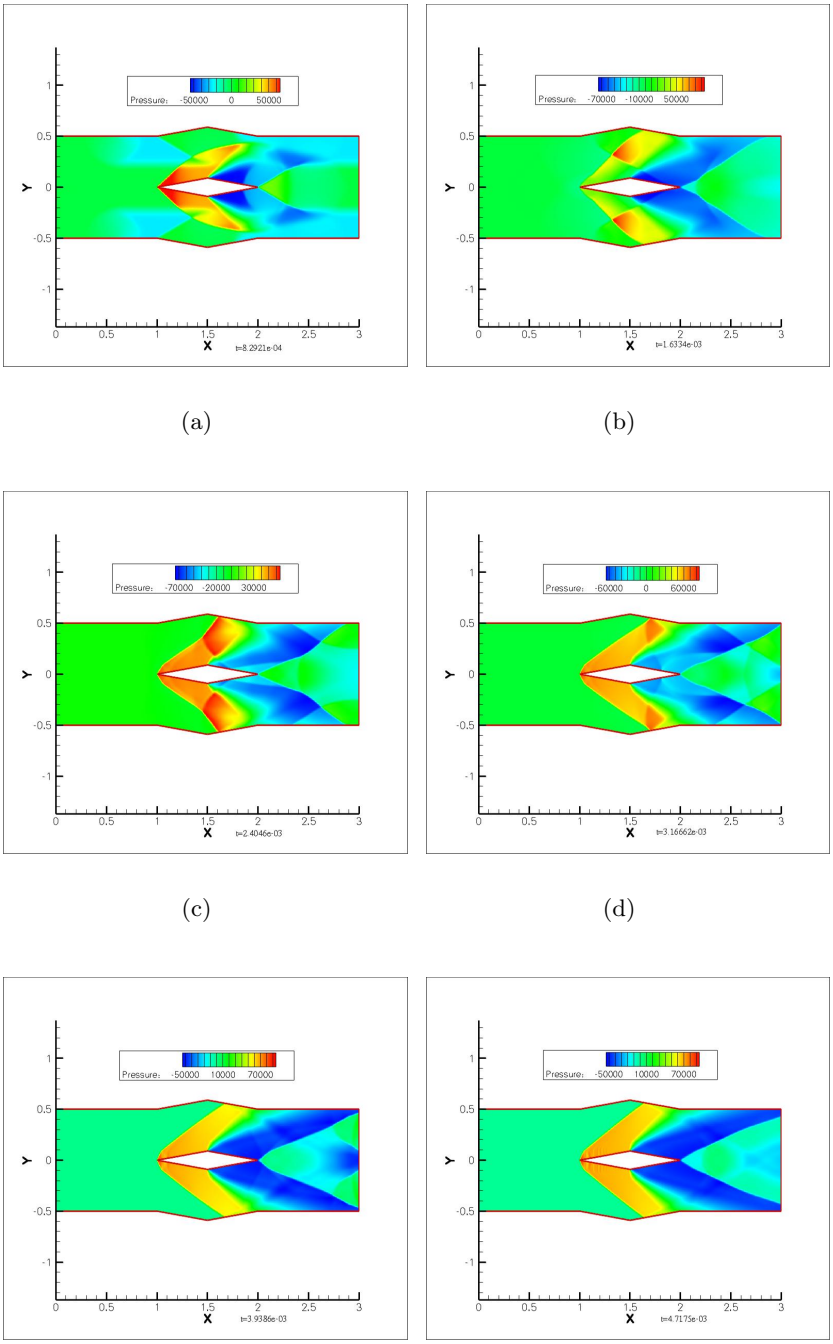

(a) (b)

(c) (d)

(e) (f)

Figure 4.24: Six pressure contours for the flow simulation with the infinitely long symmetric filament ($\frac{d}{t} = 1.00$)

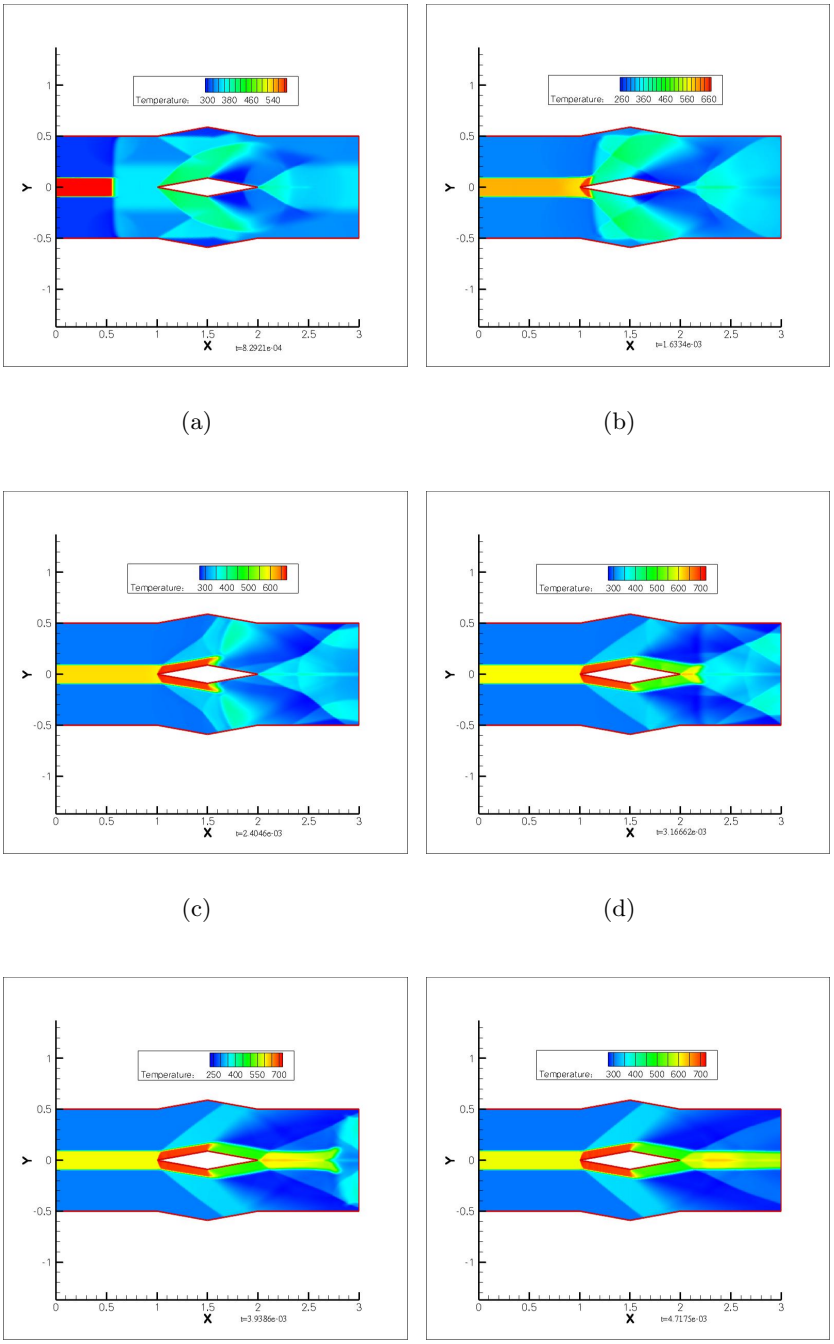

Figure 4.25: Six temperature contours for the flow simulation with the infinitely long symmetric filament ($\frac{d}{t} = 1.00$)

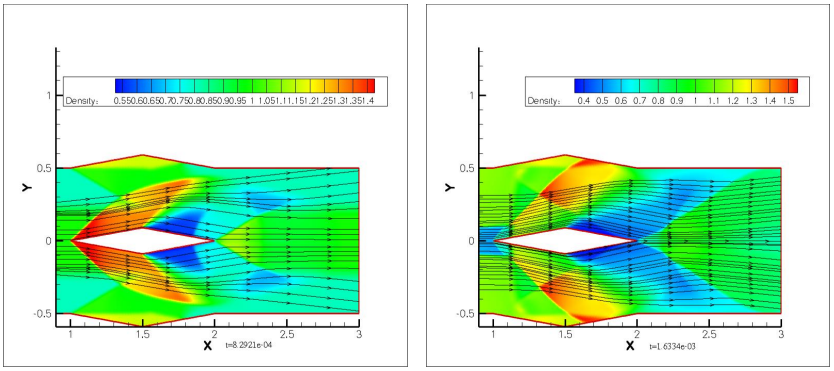

(a)

(b)

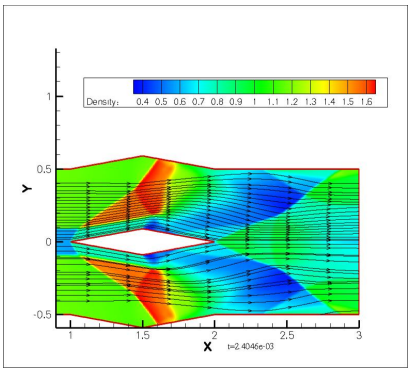

(c)

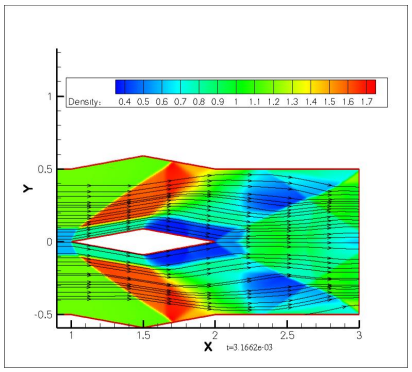

(d)

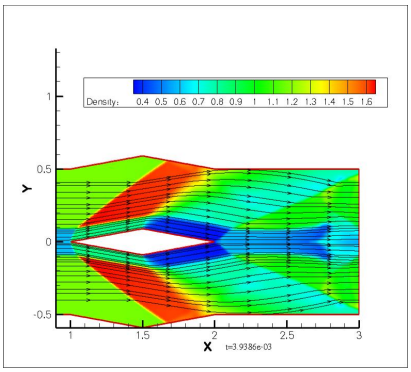

(e)

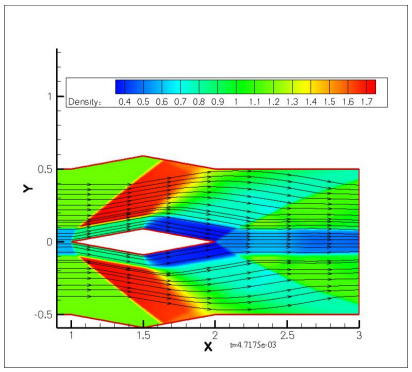

(f)

Figure 4.26: Six enlarged density contours for the flow simulation with the infinitely long symmetric filament ($\frac{d}{t} = 1.00$)

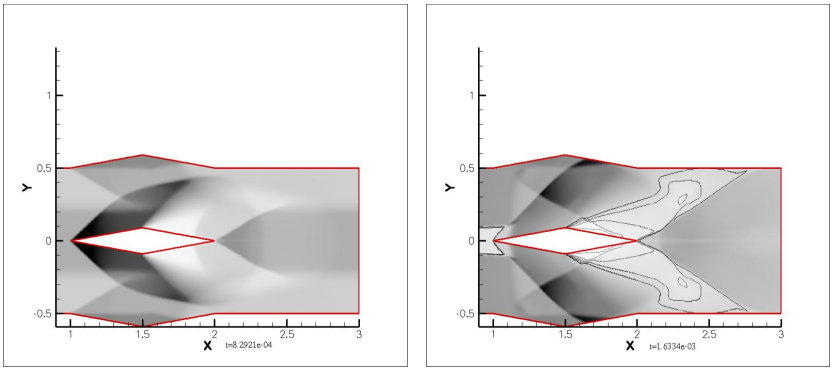

(a) (b)

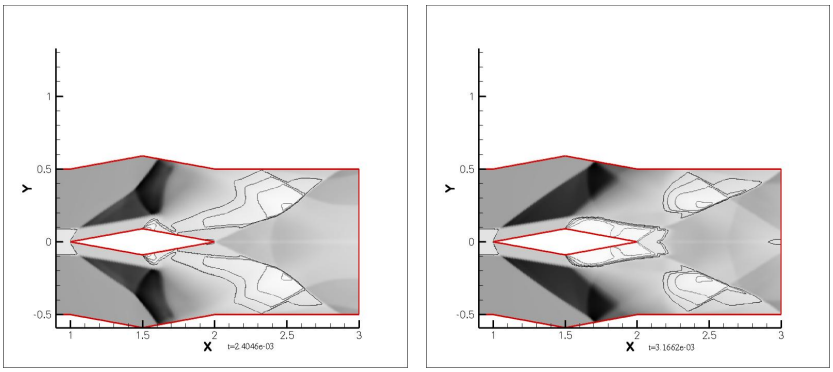

(c) (d)

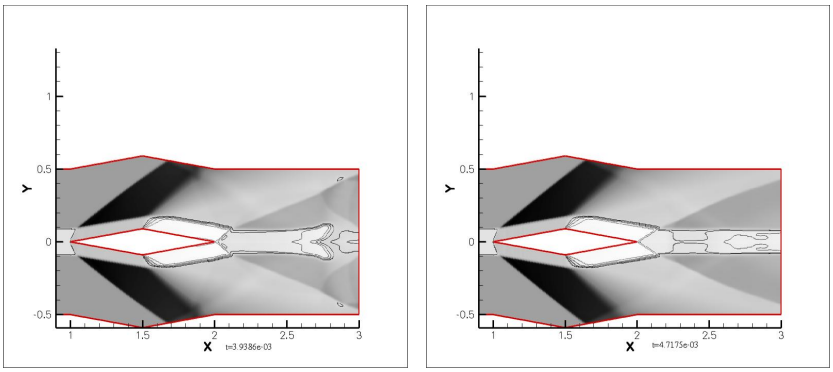

(e) (f)

Figure 4.27: Six enlarged numerical shilieren contours for the flow simulation with the infinitely long symmetric filament ($\frac{d}{t} = 1.00$)

Table 4.3: Average results of drag coefficient in the simulation with infinitely long filament

$\frac{d}{t}$	drag coefficient
0.10	0.0754
0.25	0.0749
0.50	0.0743
1.00	0.0725

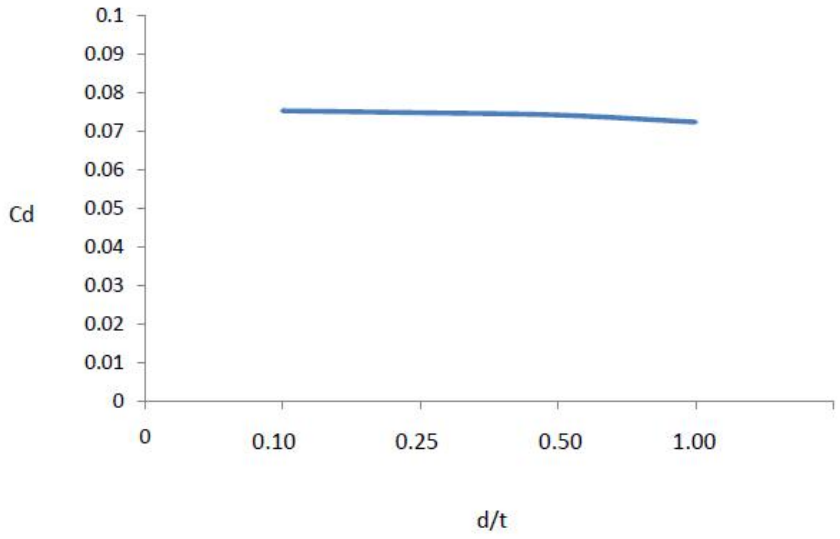

Figure 4.28: Computed average values of drag coefficient in the simulation with infinitely long symmetric filament

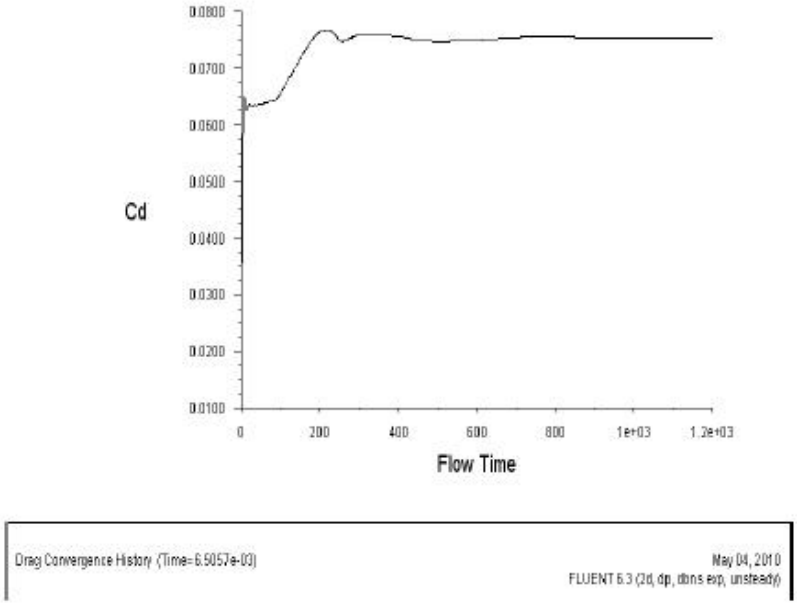

(a) $\frac{d}{t} = 0.10$

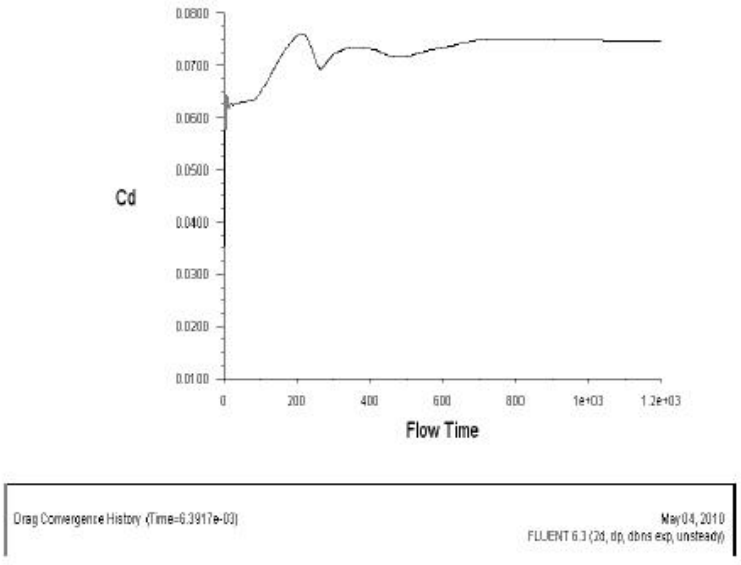

(b) $\frac{d}{t} = 0.25$

Figure 4.29: Computed drag coefficient with flow time (infinitely long symmetric filament) 1

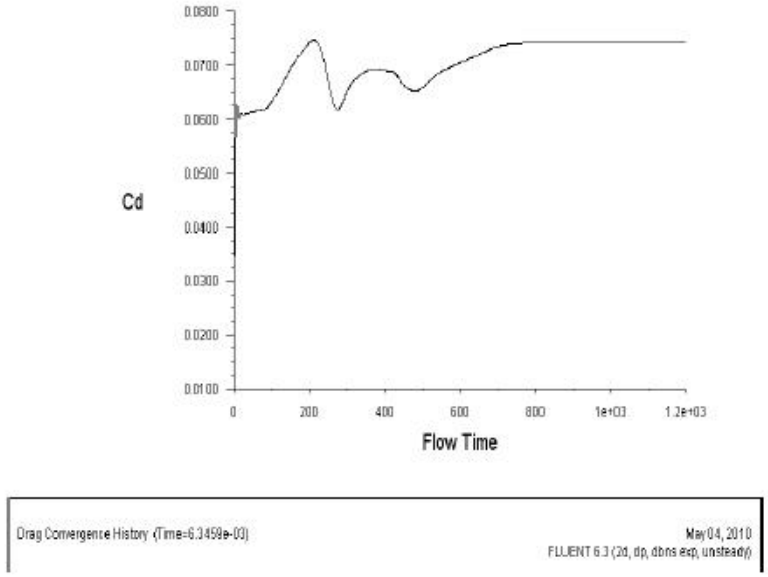

(a) $\frac{d}{t} = 0.50$

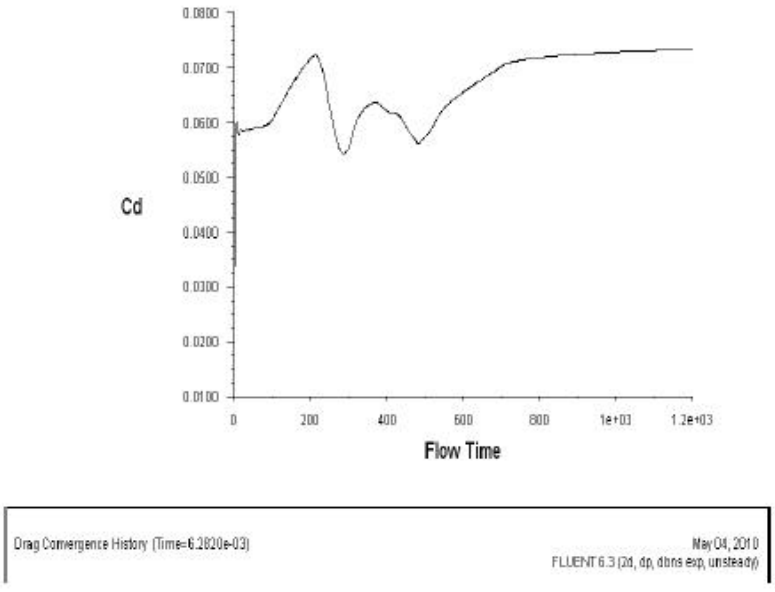

(b) $\frac{d}{t} = 1.00$

Figure 4.30: Computed drag coefficient with flow time (infinitely long symmetric filament) 2

4.3 Symmetric Pulsed Filament

4.3.1 Parameters of Flow Field Analysis

Table 4.4: Symmetric Pulsed Filament

Type Description	$\frac{d}{t}$	$\frac{l}{t}$	$\frac{L}{t}$	$\frac{h}{t}$
pulsed filament (symmetric)	0.10 0.25 0.50 1.00	1	2	0

The length of each filament and the distance between consecutive filaments is constant. The position of the filament relative to the airfoil is symmetric.

Figure 4.31 to 4.50 are the Mach number, pressure, temperature, enlarged density contours with numerical schlieren images for these four different diameter pulsed filament cases.

4.3.2 Case 1 ($\frac{d}{t} = 0.10$)

The results presented in this section is the first case of the studying the interaction of a symmetric pulsed filament. Figures 4.31 to 4.35 shows the process of the first shock, expansion fan and the second shock formed and the change of the pressure, Mach number, density in the flow region. The symmetric pulsed filament with $\frac{d}{t} = 0.10$ is formed and there is progressional contact between the flow and the filament.

4.3.3 Case 2 ($\frac{d}{t} = 0.25$)

In this section, the symmetric pulsed filament is wider, so we can observe something more clearly. In the second weak shock region, the shape of filament changed from rectangle to bullet-shaped.

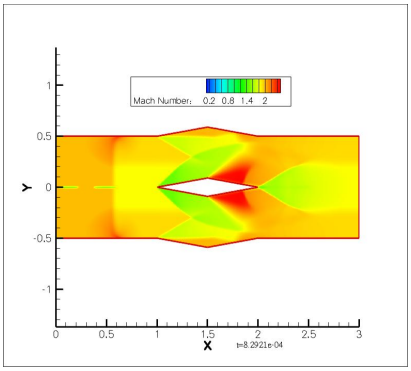

(a) in the 150 time steps

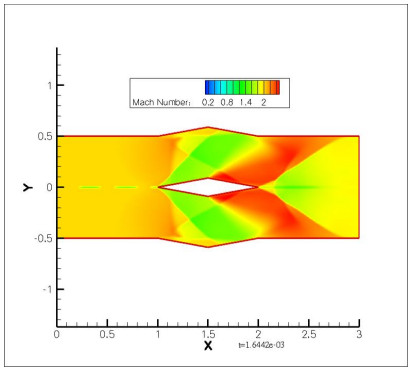

(b) in the 300 time steps

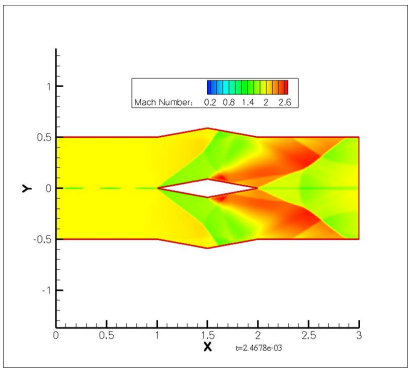

(c) in the 450 time steps

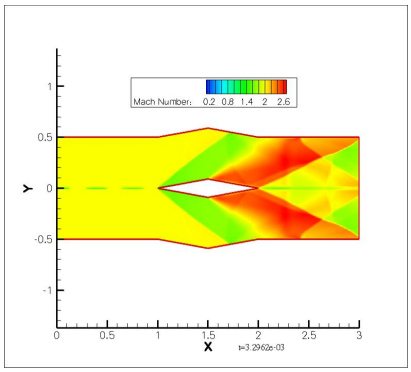

(d) in the 600 time steps

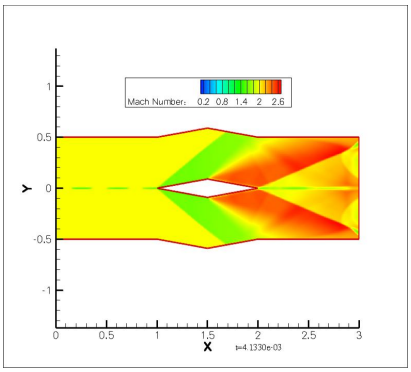

(e) in the 750 time steps

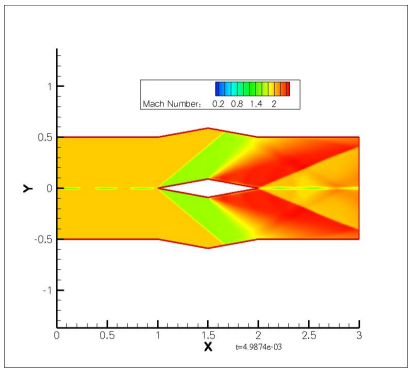

(f) in the 900 time steps

Figure 4.31: Six Mach number contours for the flow simulation with the symmetric pulsed filament ($\frac{d}{t} = 0.10$)

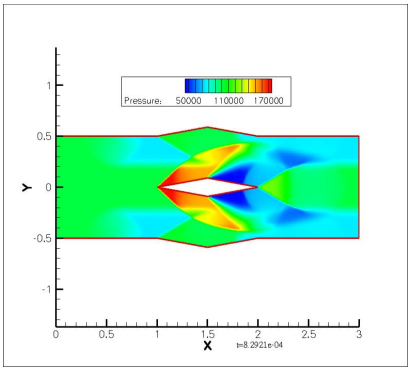

(a) in the 150 time steps

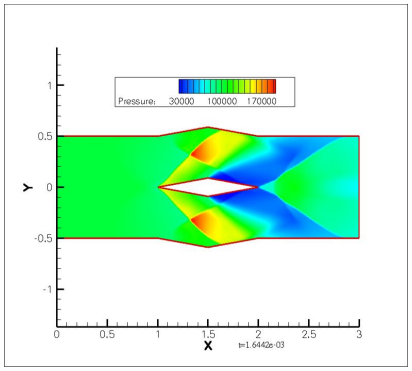

(b) in the 300 time steps

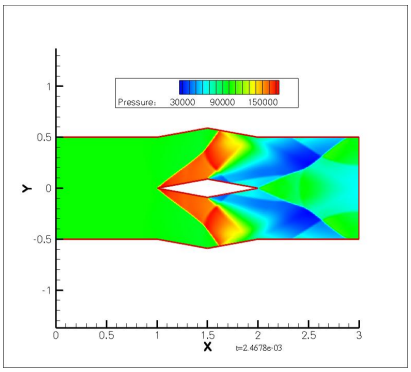

(c) in the 450 time steps

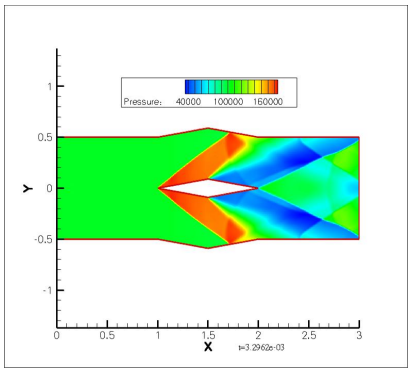

(d) in the 600 time steps

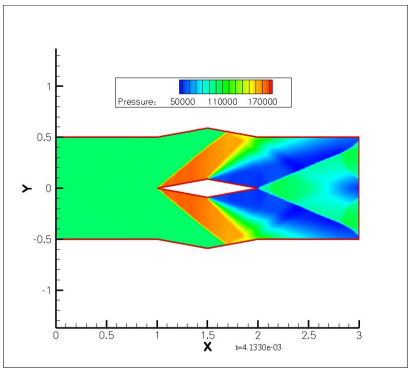

(e) in the 750 time steps

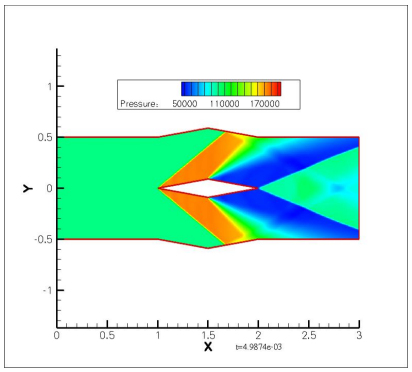

(f) in the 900 time steps

Figure 4.32: Six pressure contours for the flow simulation with the symmetric pulsed filament ($\frac{d}{t} = 0.10$)

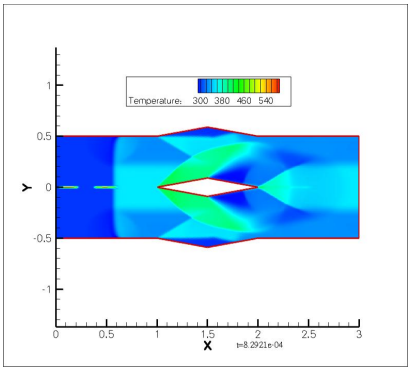

(a) in the 150 time steps

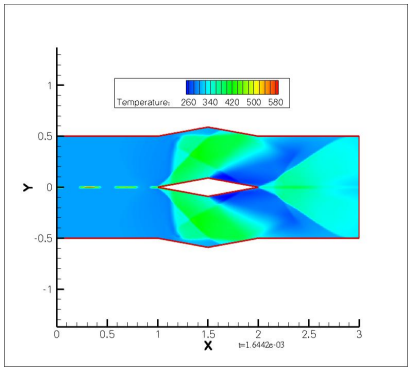

(b) in the 300 time steps

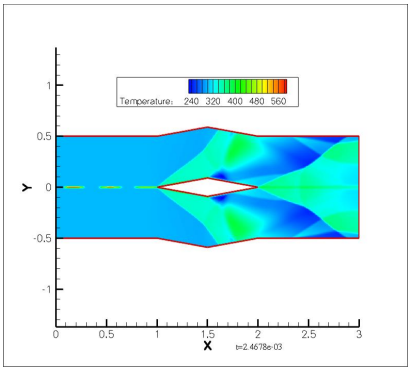

(c) in the 450 time steps

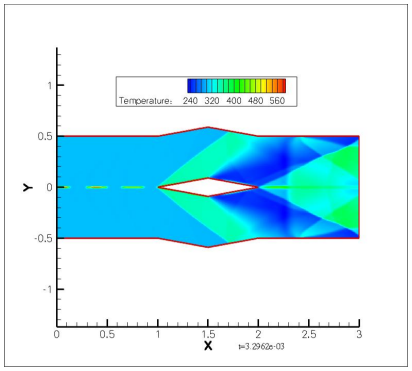

(d) in the 600 time steps

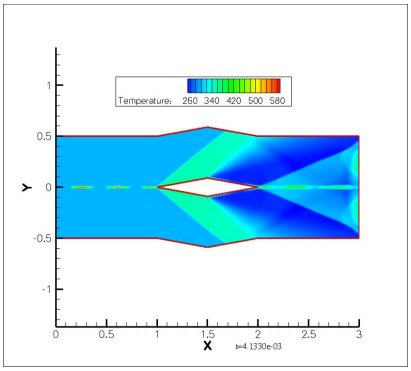

(e) in the 750 time steps

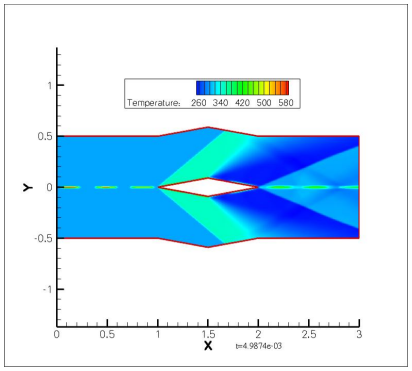

(f) in the 900 time steps

Figure 4.33: Six temperature contours for the flow simulation with the symmetric pulsed filament ($\frac{d}{t} = 0.10$)

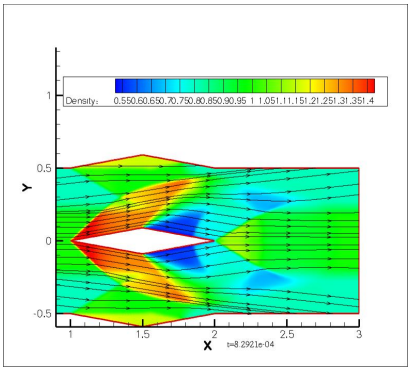

(a) in the 150 time steps

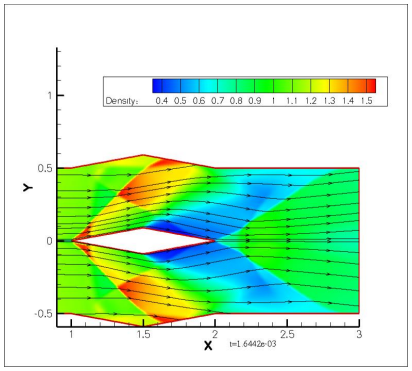

(b) in the 300 time steps

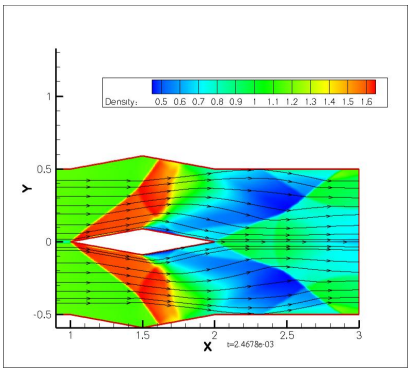

(c) in the 450 time steps

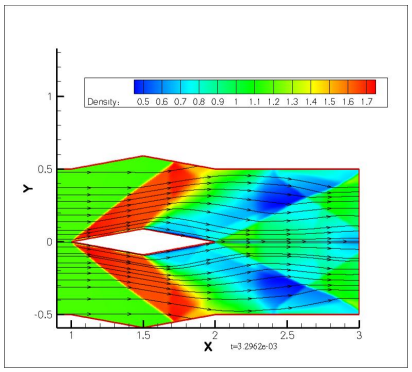

(d) in the 600 time steps

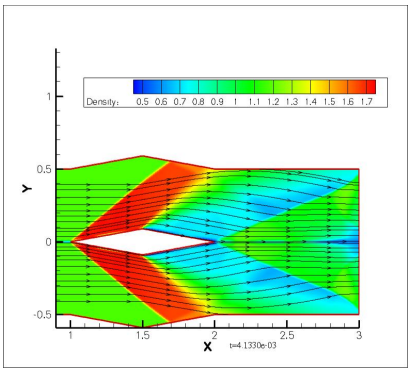

(e) in the 750 time steps

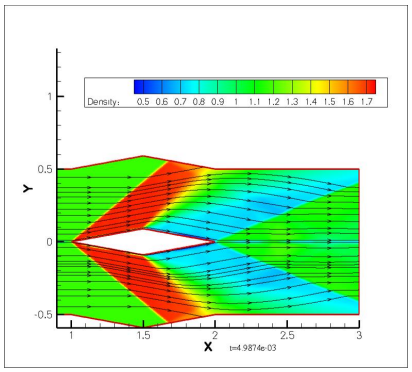

(f) in the 900 time steps

Figure 4.34: Six enlarged density contours for the flow simulation with the symmetric pulsed filament ($\frac{d}{t} = 0.10$)

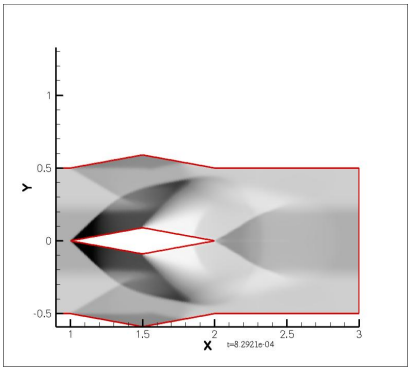

(a) in the 150 time steps

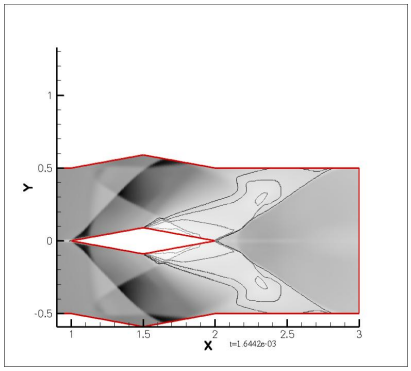

(b) in the 300 time steps

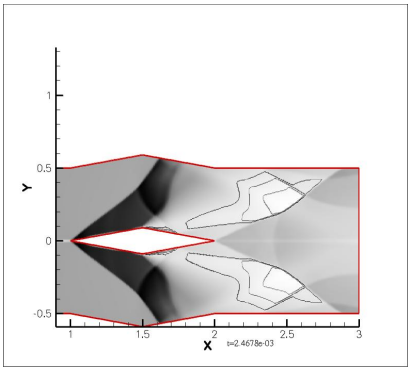

(c) in the 450 time steps

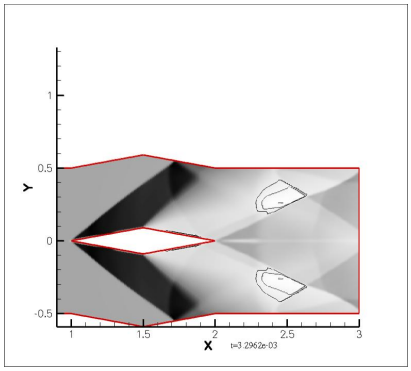

(d) in the 600 time steps

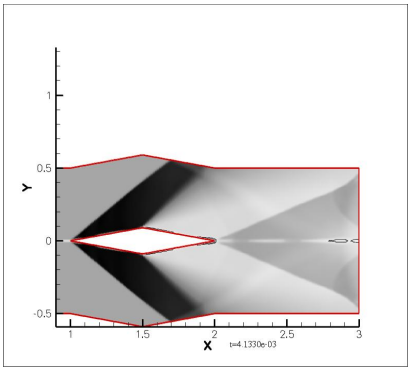

(e) in the 750 time steps

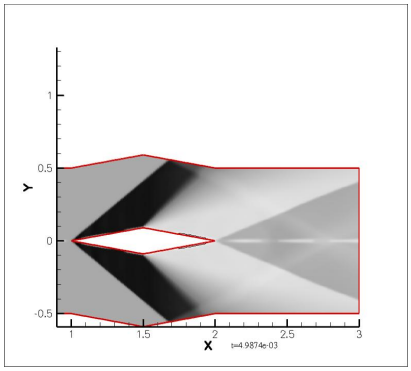

(f) in the 900 time steps

Figure 4.35: Six enlarged numerical schilieren contours for the flow simulation with the symmetric pulsed filament ($\frac{d}{t} = 0.10$)

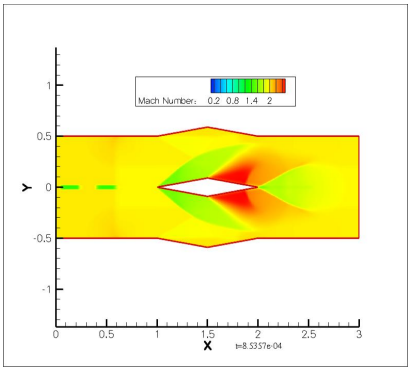

(a) in the 150 time steps

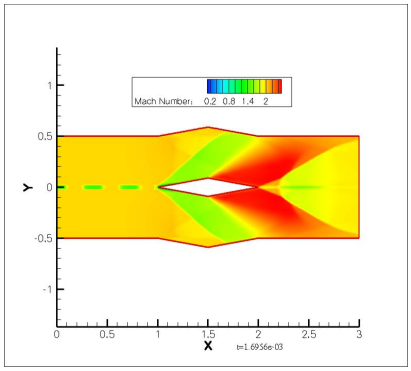

(b) in the 300 time steps

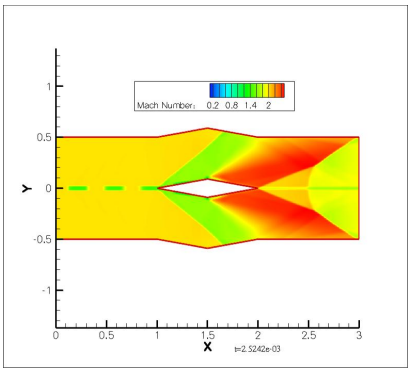

(c) in the 450 time steps

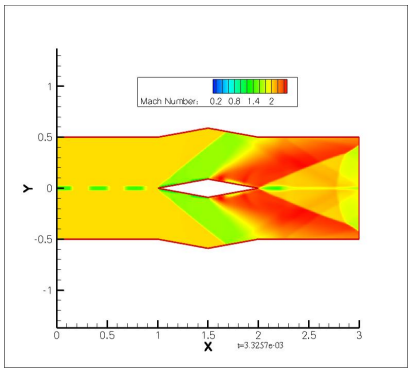

(d) in the 600 time steps

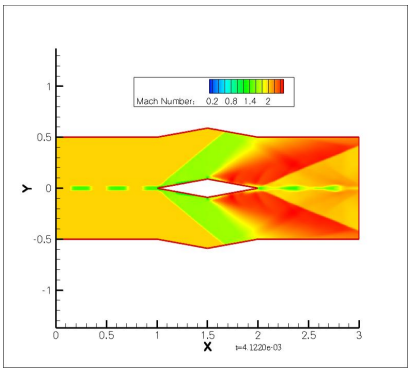

(e) in the 750 time steps

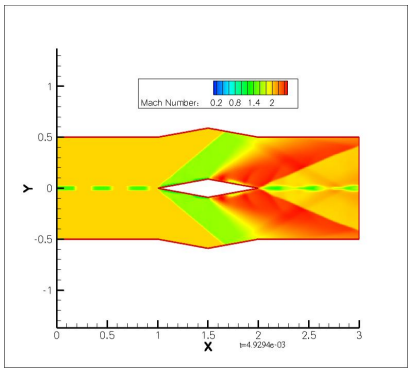

(f) in the 900 time steps

Figure 4.36: Six Mach number contours for the flow simulation with the symmetric pulsed filament ($\frac{d}{t} = 0.25$)

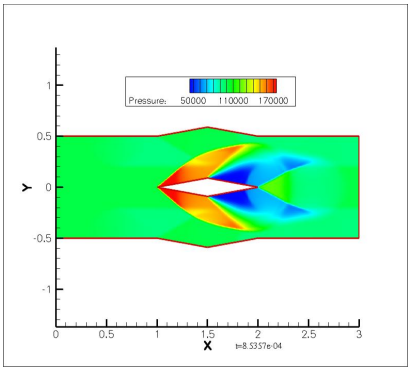

(a) in the 150 time steps

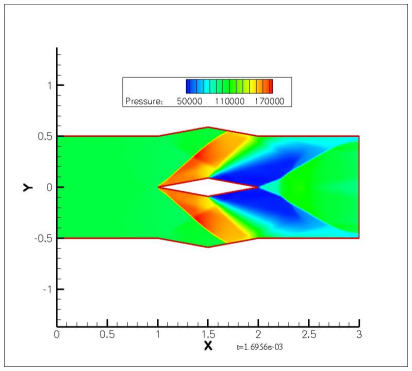

(b) in the 300 time steps

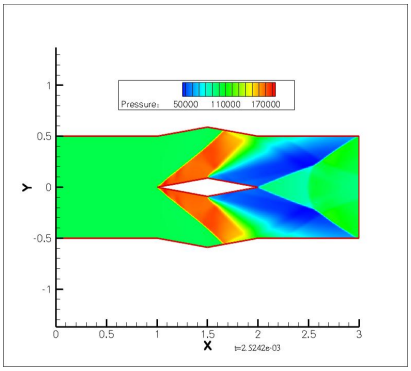

(c) in the 450 time steps

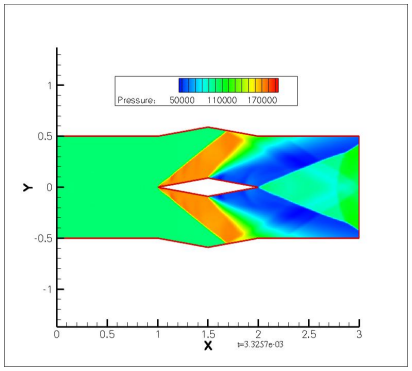

(d) in the 600 time steps

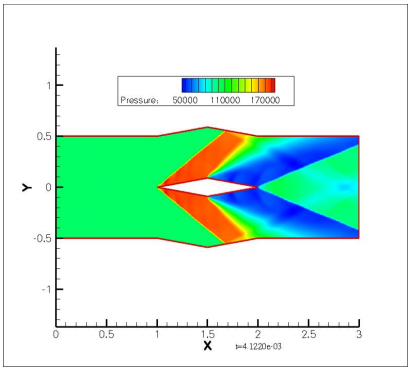

(e) in the 750 time steps

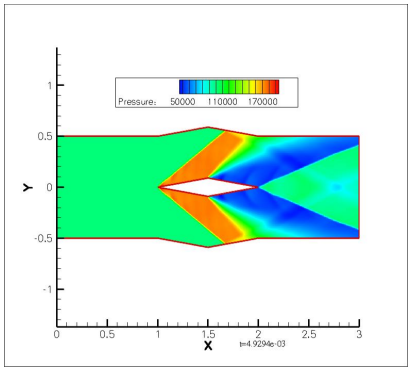

(f) in the 900 time steps

Figure 4.37: Six pressure contours for the flow simulation with the symmetric pulsed filament ($\frac{d}{t} = 0.25$)

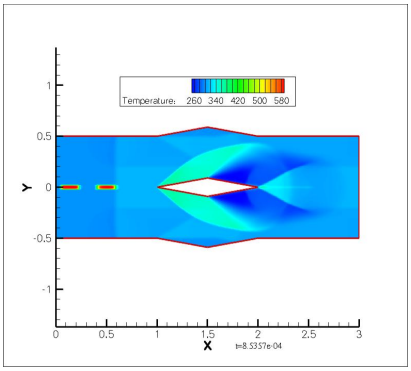

(a) in the 150 time steps

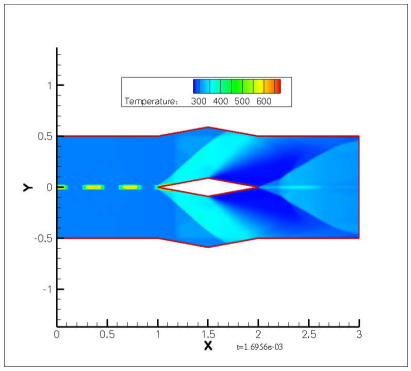

(b) in the 300 time steps

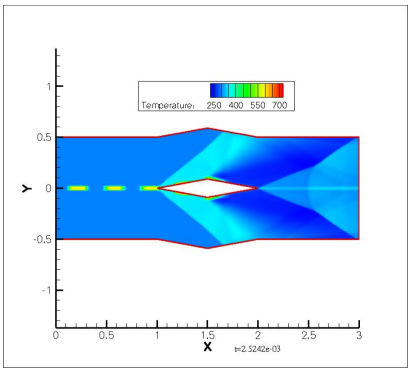

(c) in the 450 time steps

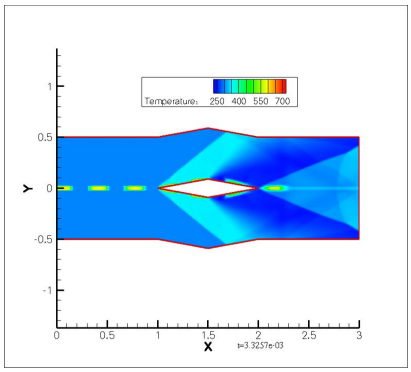

(d) in the 600 time steps

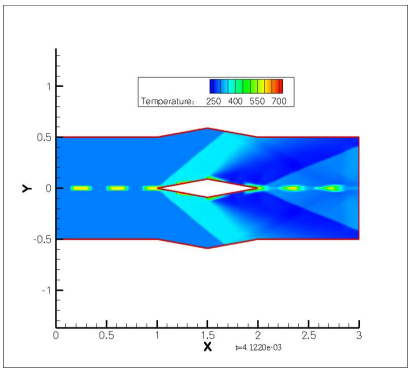

(e) in the 750 time steps

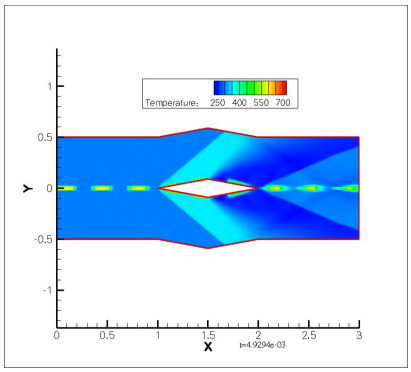

(f) in the 900 time steps

Figure 4.38: Six temperature contours for the flow simulation with the symmetric pulsed filament ($\frac{d}{t} = 0.25$)

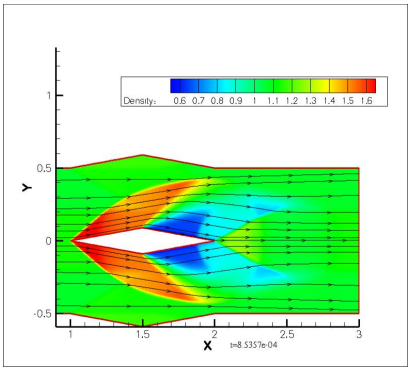

(a) in the 150 time steps

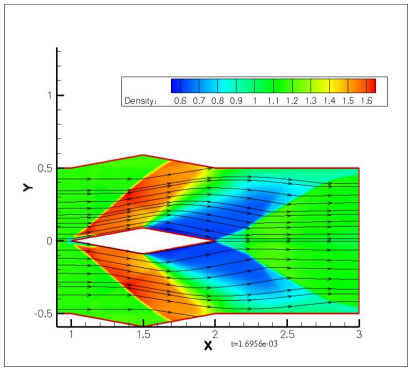

(b) in the 300 time steps

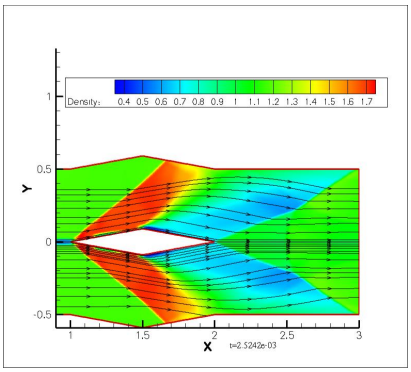

(c) in the 450 time steps

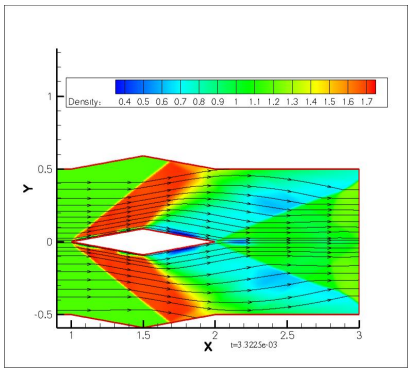

(d) in the 600 time steps

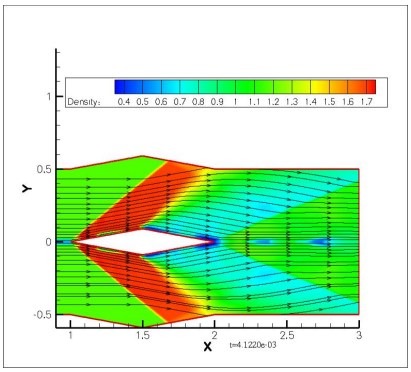

(e) in the 750 time steps

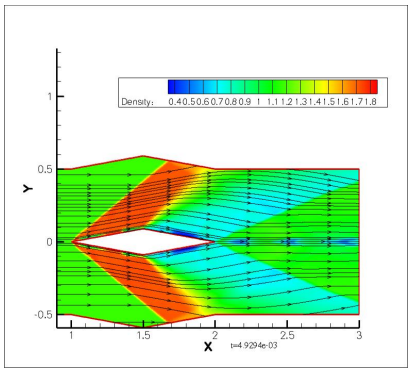

(f) in the 900 time steps

Figure 4.39: Six enlarged density contours for the flow simulation with the symmetric pulsed filament ($\frac{d}{t} = 0.25$)

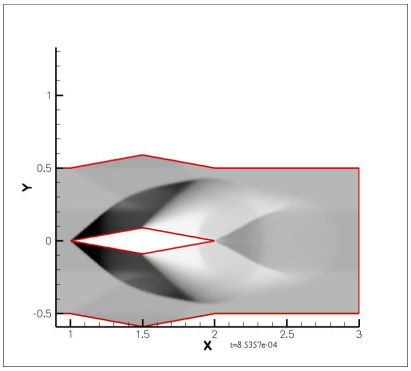

(a) in the 150 time steps

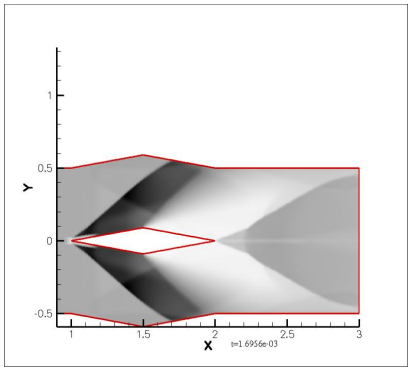

(b) in the 300 time steps

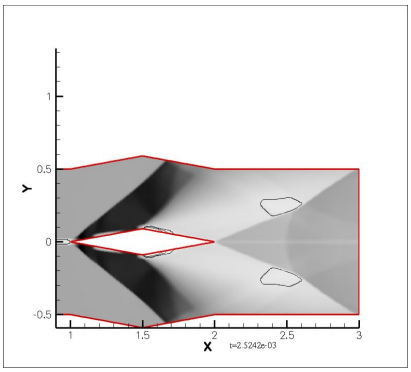

(c) in the 450 time steps

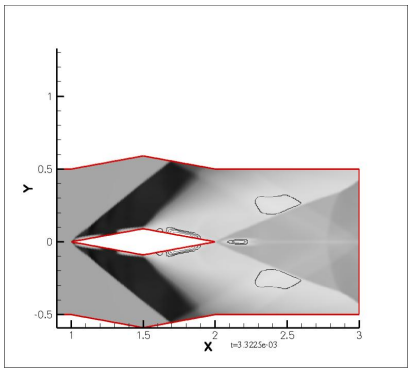

(d) in the 600 time steps

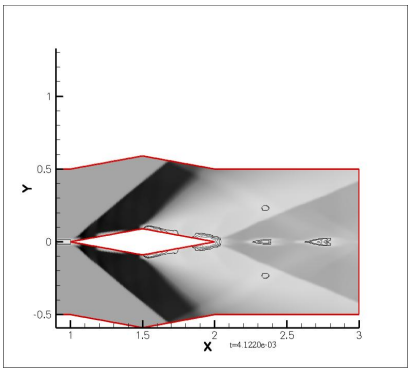

(e) in the 750 time steps

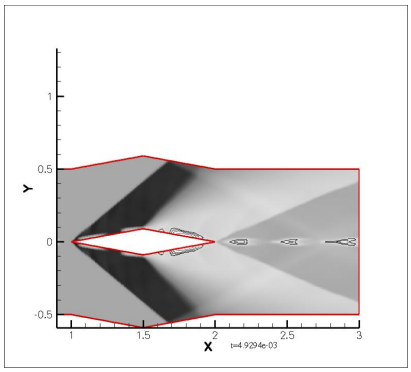

(f) in the 900 time steps

Figure 4.40: Six enlarged numerical schilieren contours for the flow simulation with the symmetric pulsed filament ($\frac{d}{t} = 0.25$)

4.3.4 Case 3 ($\frac{d}{t} = 0.50$)

In this section, except we can observe the conclusions observed in the sections above more clearly, and more features can be seen:

1. An almost "normal shock" has formed near the leading edge of the diamond-shaped airfoil (similar to Chapter 4.2.4).
2. The filament (higher temperature and lower density region) makes the angle of the expansion fan bigger.

4.3.5 Case 4 ($\frac{d}{t} = 1.00$)

All the features of the flow and filament can be observed, because all the figures in this section is most clear:

1. The first oblique shock is formed at the front point of the diamond-shaped airfoil body with the flow.
2. The expansion fan is formed over the corner of the diamond-shaped airfoil.
3. The second oblique shock is formed at the end point of the diamond-shaped airfoil.
4. The symmetric pulsed filament is formed.
5. The Mach number decreases after the shock wave and increases through the expansion both in the flow and filament region.
6. The pressure and temperature are just on the contrary, i.e., increasing after the shock, and then decreasing in the expansion both in the flow and filament region .
7. The progressional contact formed between the flow and the filament
8. An almost "normal shock" has formed near the leading edge of the diamond-shaped airfoil. This is true for all four cases, but is apparent in the contours plots for the thicker filament only (the normal shock in the case with $\frac{d}{t} = 1.00$ is most apparent). Actually, the "normal shock" would be a detached shock, but appears to be "attached" due to the finite size of the grid cells.

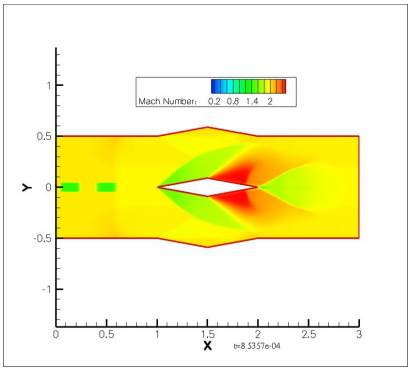

(a) in the 150 time steps

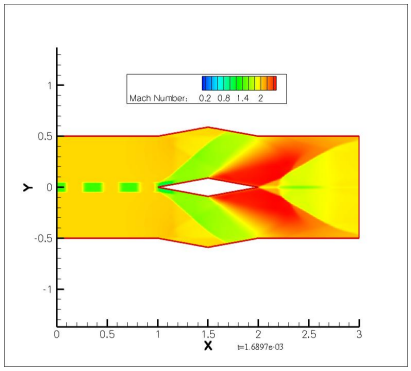

(b) in the 300 time steps

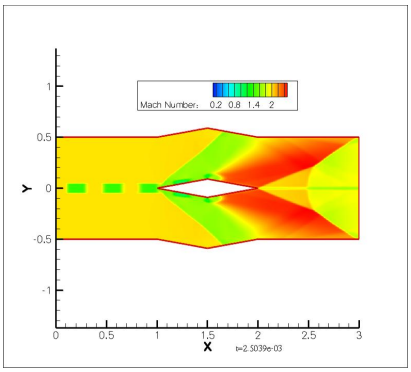

(c) in the 450 time steps

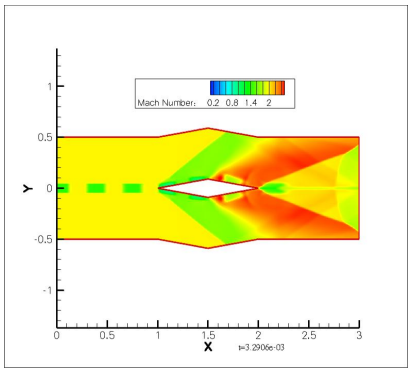

(d) in the 600 time steps

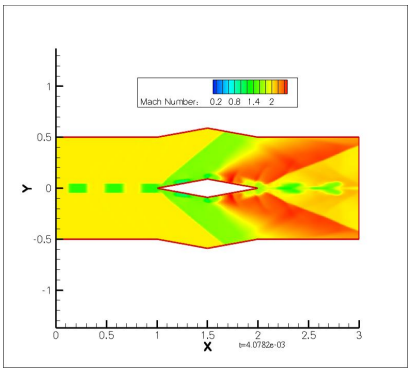

(e) in the 750 time steps

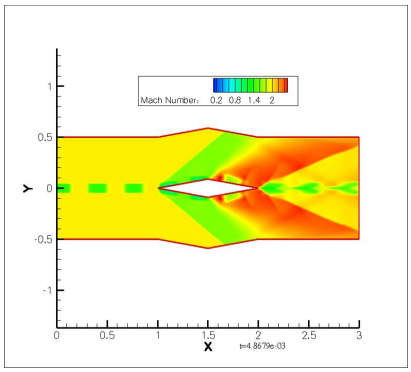

(f) in the 900 time steps

Figure 4.41: Six Mach number contours for the flow simulation with the symmetric pulsed filament ($\frac{d}{t} = 0.50$)

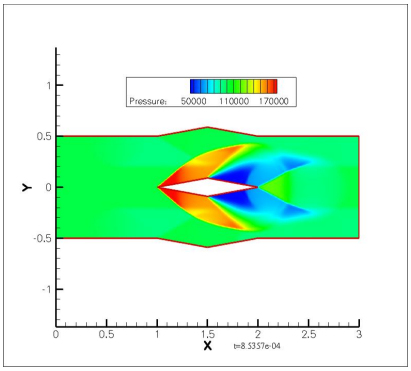

(a) in the 150 time steps

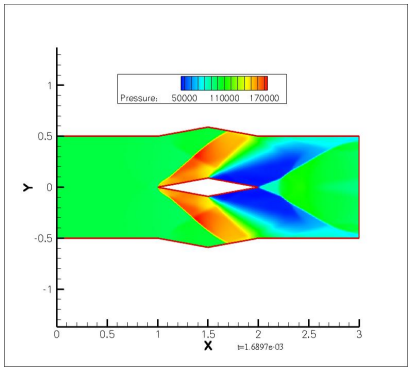

(b) in the 300 time steps

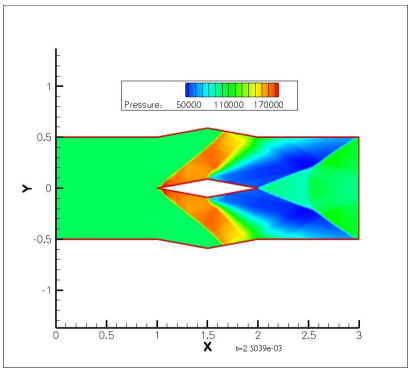

(c) in the 450 time steps

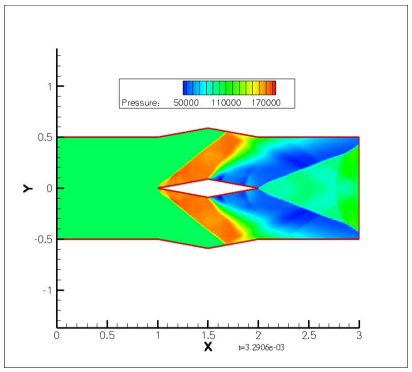

(d) in the 600 time steps

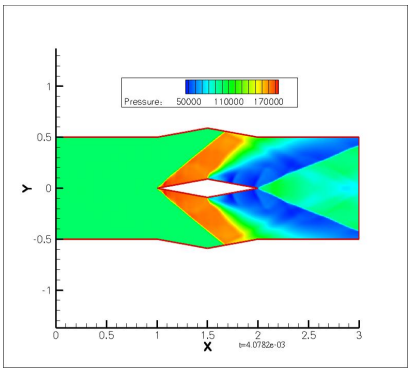

(e) in the 750 time steps

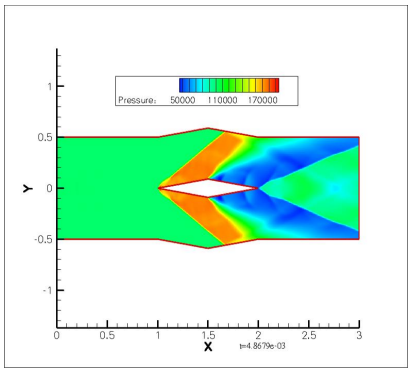

(f) in the 900 time steps

Figure 4.42: Six pressure contours for the flow simulation with the symmetric pulsed filament ($\frac{d}{t} = 0.50$)

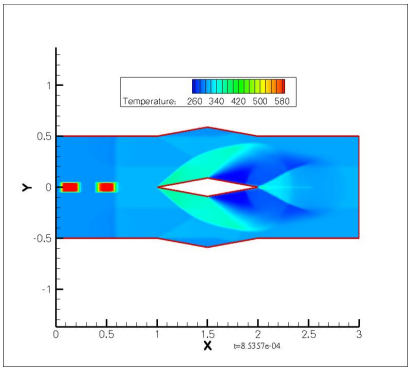

(a) in the 150 time steps

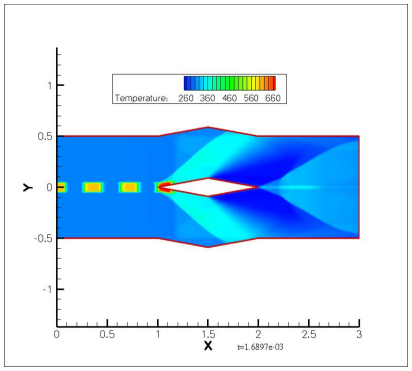

(b) in the 300 time steps

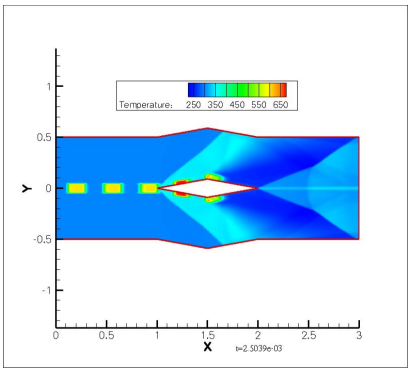

(c) in the 450 time steps

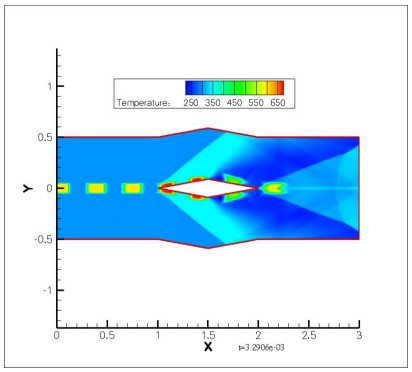

(d) in the 600 time steps

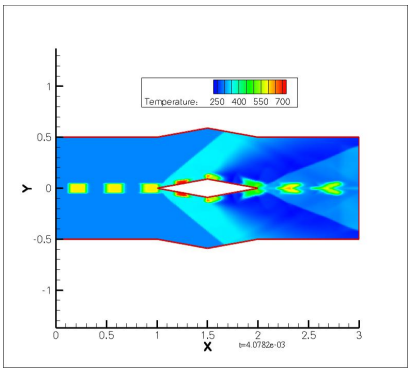

(e) in the 750 time steps

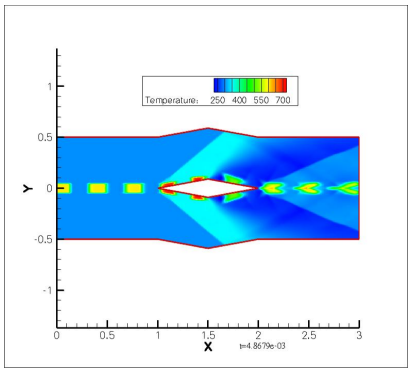

(f) in the 900 time steps

Figure 4.43: Six temperature contours for the flow simulation with the symmetric pulsed filament ($\frac{d}{t} = 0.50$)

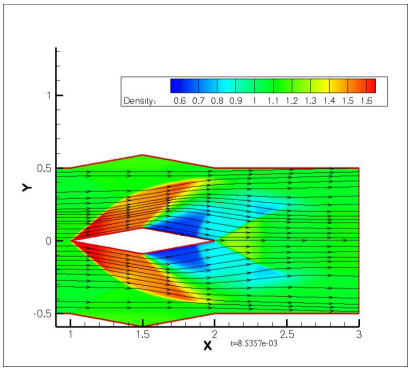

(a) in the 150 time steps

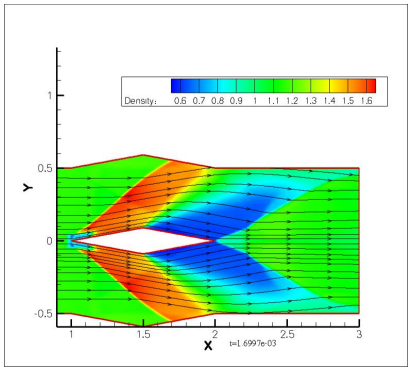

(b) in the 300 time steps

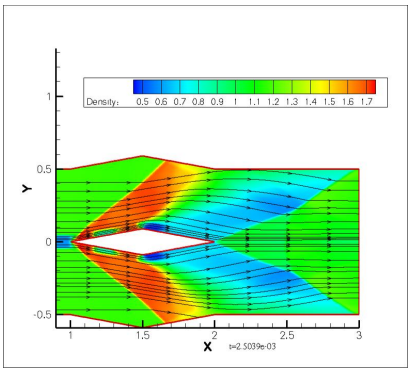

(c) in the 450 time steps

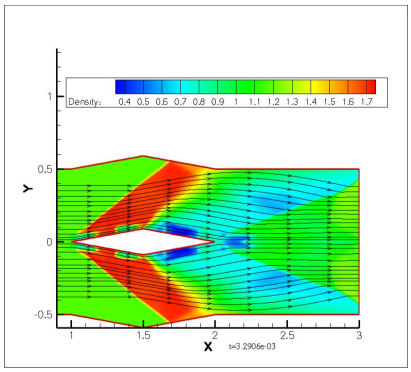

(d) in the 600 time steps

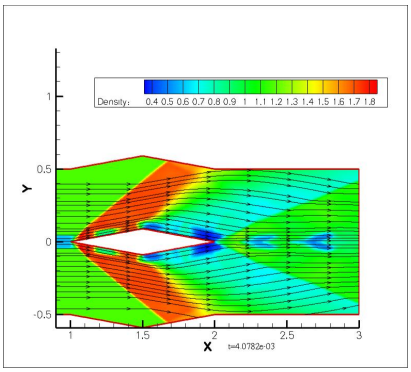

(e) in the 750 time steps

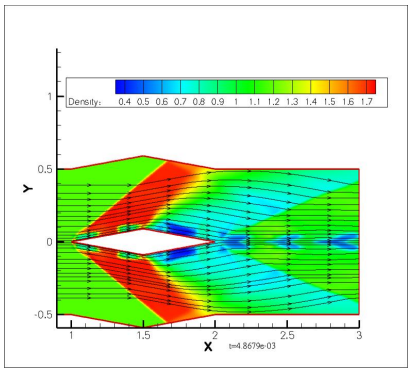

(f) in the 900 time steps

Figure 4.44: Six enlarged density contours for the flow simulation with the symmetric pulsed filament ($\frac{d}{t} = 0.50$)

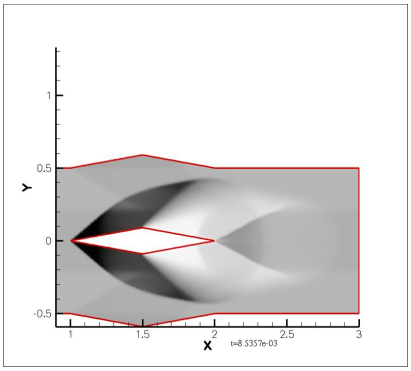

(a) in the 150 time steps

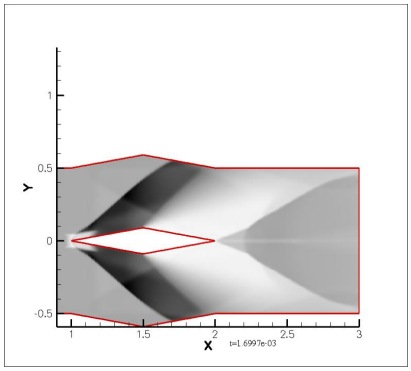

(b) in the 300 time steps

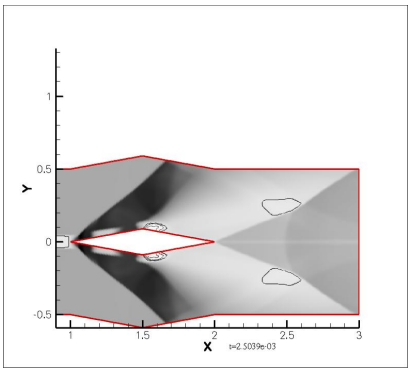

(c) in the 450 time steps

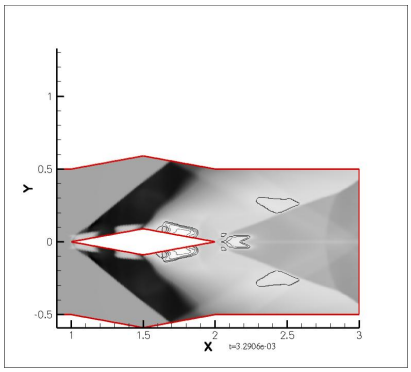

(d) in the 600 time steps

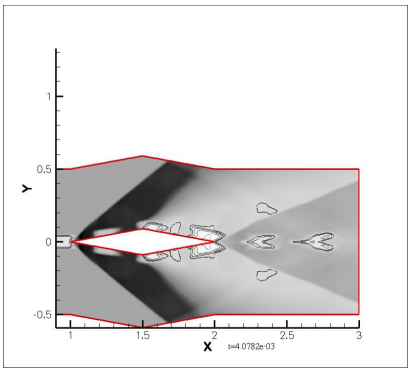

(e) in the 750 time steps

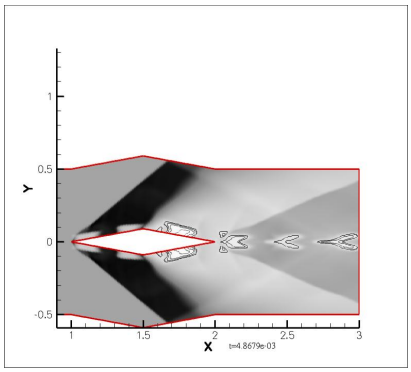

(f) in the 900 time steps

Figure 4.45: Six enlarged numerical schilieren contours for the flow simulation with the symmetric pulsed filament ($\frac{d}{t} = 0.50$)

9. The filament (higher temperature and lower density region) makes the angle of the expansion fan bigger.

10. The streamwise distortion of the filament following the second shock is quite apparent. This is due to the variation in arrival time of the front face of the filament at the shocks.

4.3.6 Drag Coefficient Analysis for Symmetric Pulsed Filament Added

Figure 4.52 shows the numerical values of the drag coefficient with time flow in four different types of heights of filaments by the flow time. The values of the drag coefficient calculated for the symmetric pulsed filament cases using FLUENT coding are instantaneous. The flow field is unsteady due to the pulsed filament. Thus, the results of the drag coefficient vary in time in Figures 4.52 and 4.53. Actually, it is observed that the curve varied more when the height of the filament is larger. Table 4.5 and Figure 4.51 shows the average values of calculated drag coefficients (Average drag coefficient after the time steps 750). It is concluded that drag coefficient decreases slightly with $\frac{d}{t}$ increasing, i.e., the height of the filament increasing. The difference in average drag coefficient between the $\frac{d}{t} = 0.10$ and $\frac{d}{t} = 1.00$ cases is 5.8%

Table 4.5: Average results of drag coefficient in the simulation with symmetric pulsed filament

$\frac{d}{t}$	drag coefficient
0.10	0.0753
0.25	0.0748
0.50	0.0731
1.00	0.0709

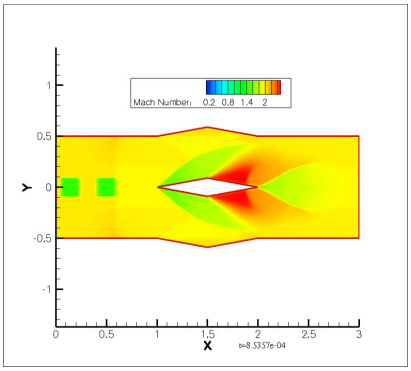

(a) in the 150 time steps

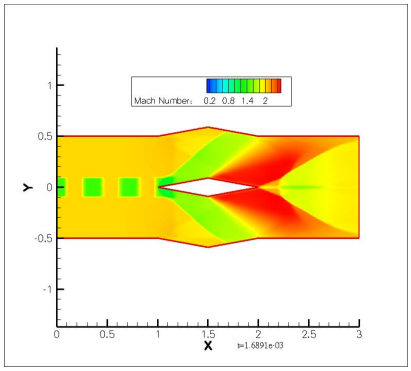

(b) in the 300 time steps

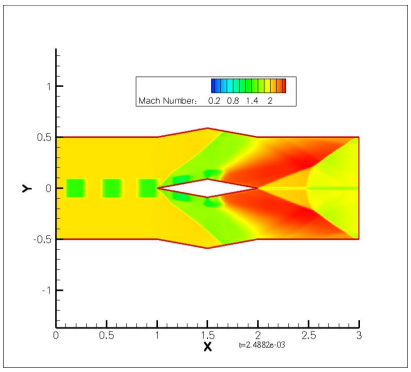

(c) in the 450 time steps

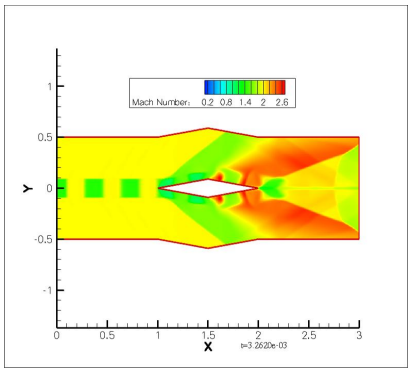

(d) in the 600 time steps

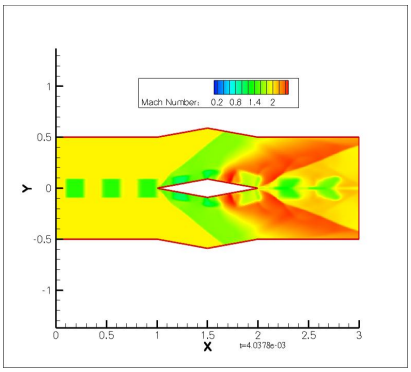

(e) in the 750 time steps

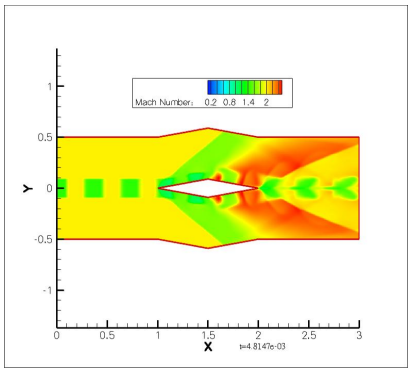

(f) in the 900 time steps

Figure 4.46: Six Mach number contours for the flow simulation with the symmetric pulsed filament ($\frac{d}{t} = 1.00$)

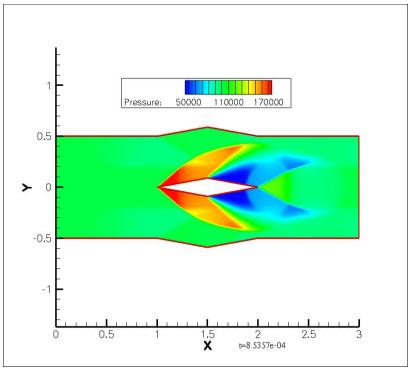

(a) in the 150 time steps

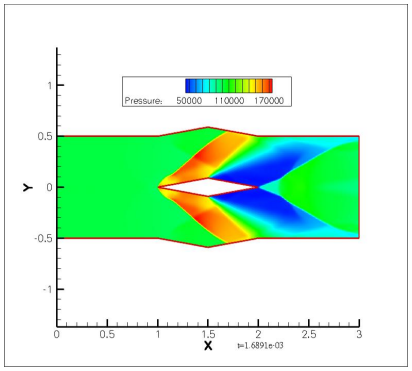

(b) in the 300 time steps

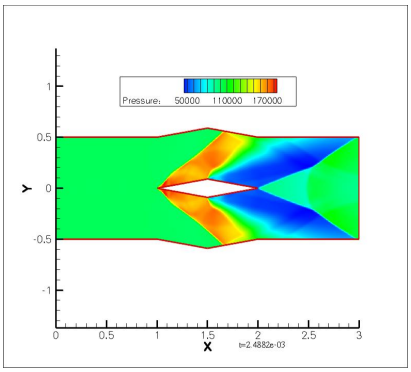

(c) in the 450 time steps

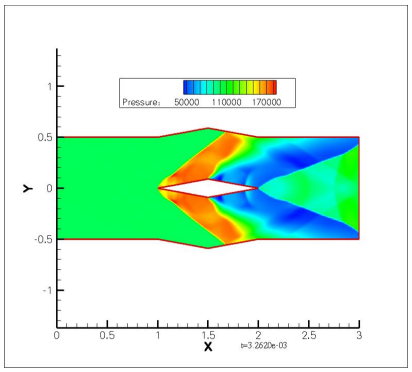

(d) in the 600 time steps

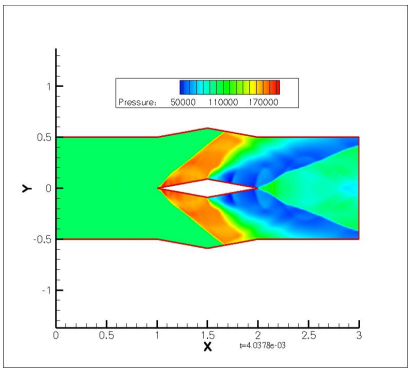

(e) in the 750 time steps

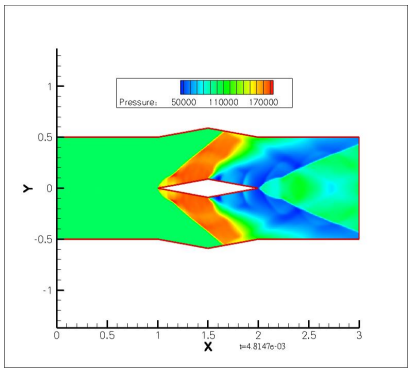

(f) in the 900 time steps

Figure 4.47: Six pressure contours for the flow simulation with the symmetric pulsed filament ($\frac{d}{t} = 1.00$)

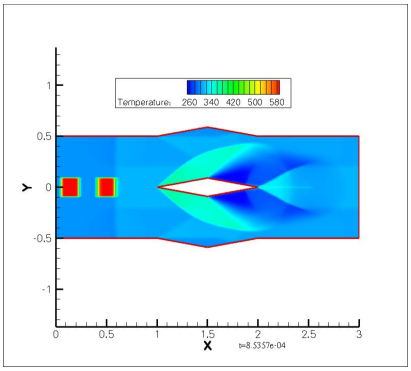

(a) in the 150 time steps

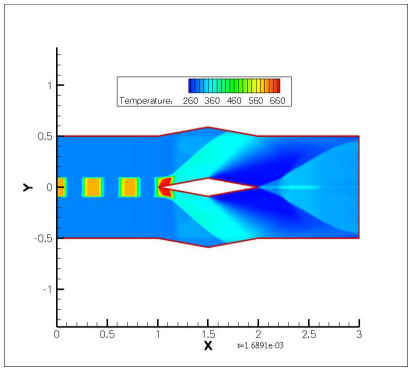

(b) in the 300 time steps

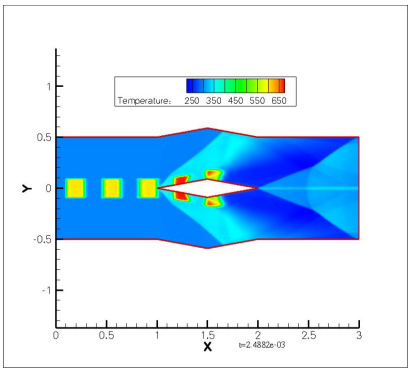

(c) in the 450 time steps

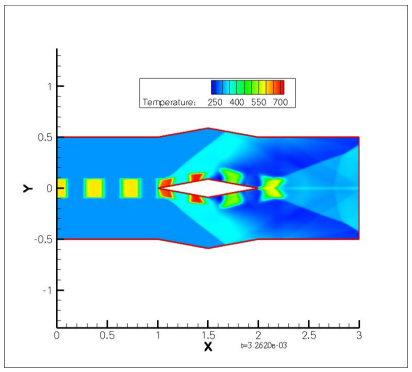

(d) in the 600 time steps

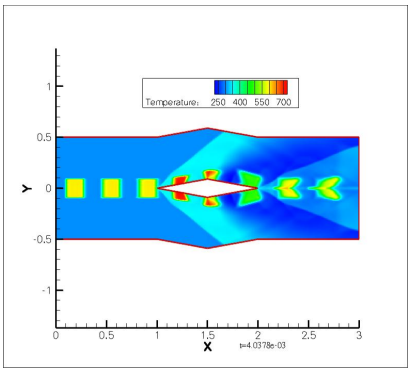

(e) in the 750 time steps

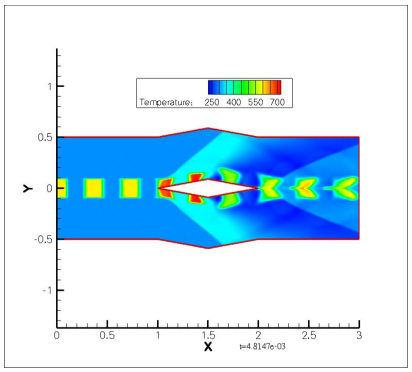

(f) in the 900 time steps

Figure 4.48: Six temperature contours for the flow simulation with the symmetric pulsed filament ($\frac{d}{t} = 1.00$)

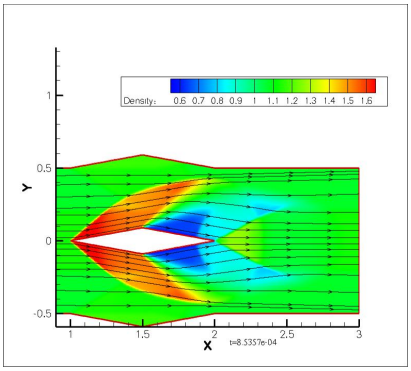

(a) in the 150 time steps

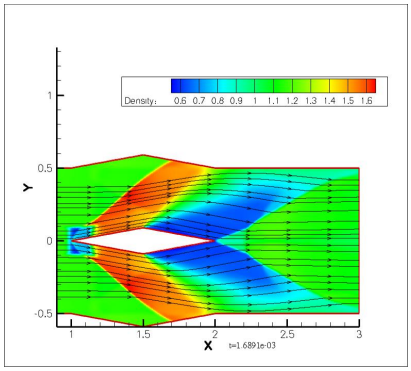

(b) in the 300 time steps

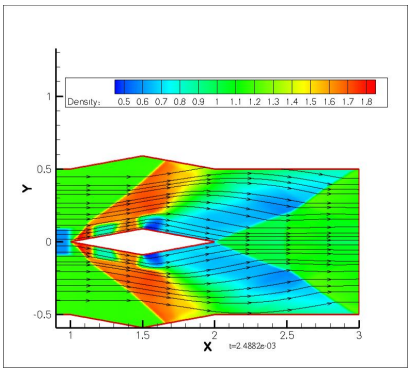

(c) in the 450 time steps

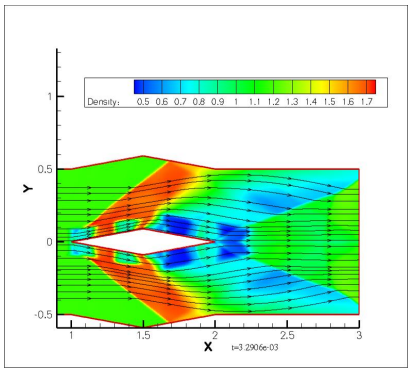

(d) in the 600 time steps

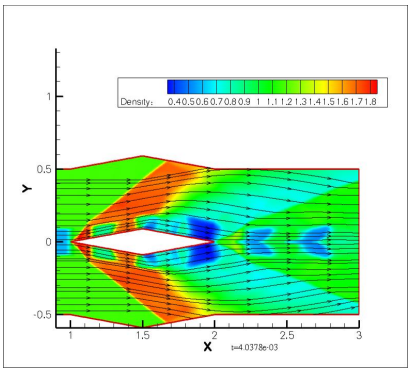

(e) in the 750 time steps

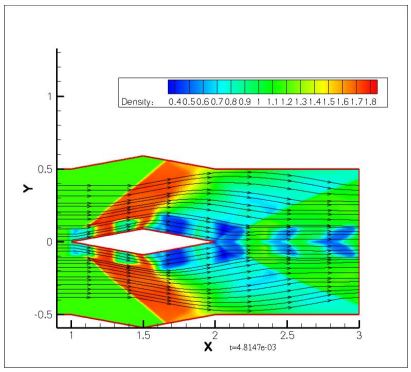

(f) in the 900 time steps

Figure 4.49: Six enlarged density contours for the flow simulation with the symmetric pulsed filament ($\frac{d}{t} = 1.00$)

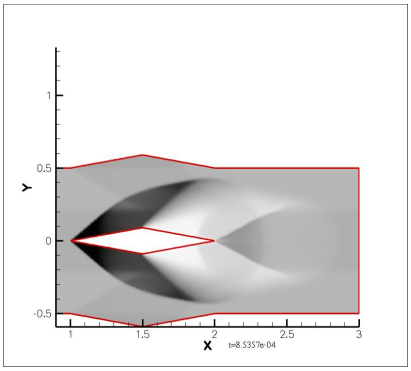

(a) in the 150 time steps

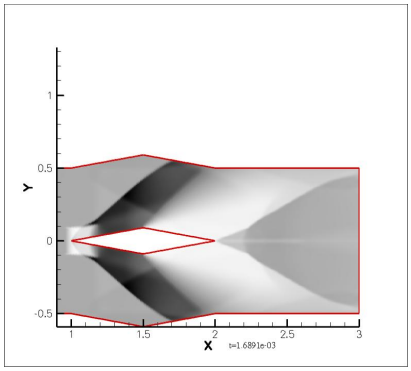

(b) in the 300 time steps

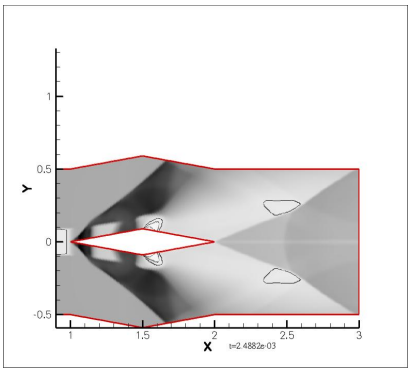

(c) in the 450 time steps

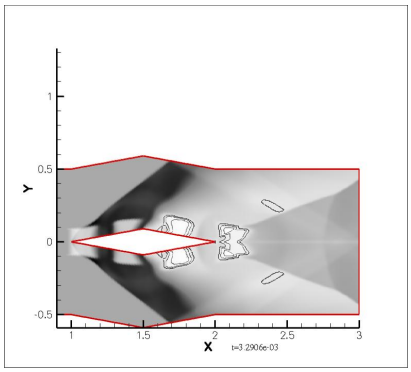

(d) in the 600 time steps

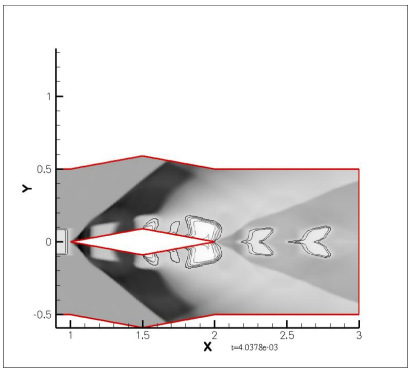

(e) in the 750 time steps

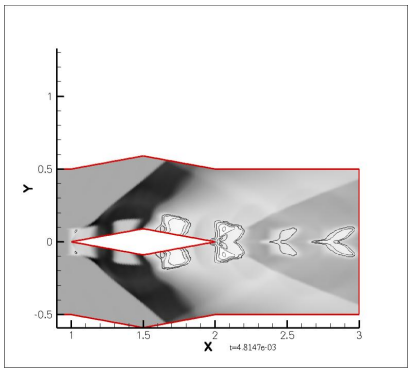

(f) in the 900 time steps

Figure 4.50: Six enlarged numerical schilieren contours for the flow simulation with the symmetric pulsed filament ($\frac{d}{t} = 1.00$)

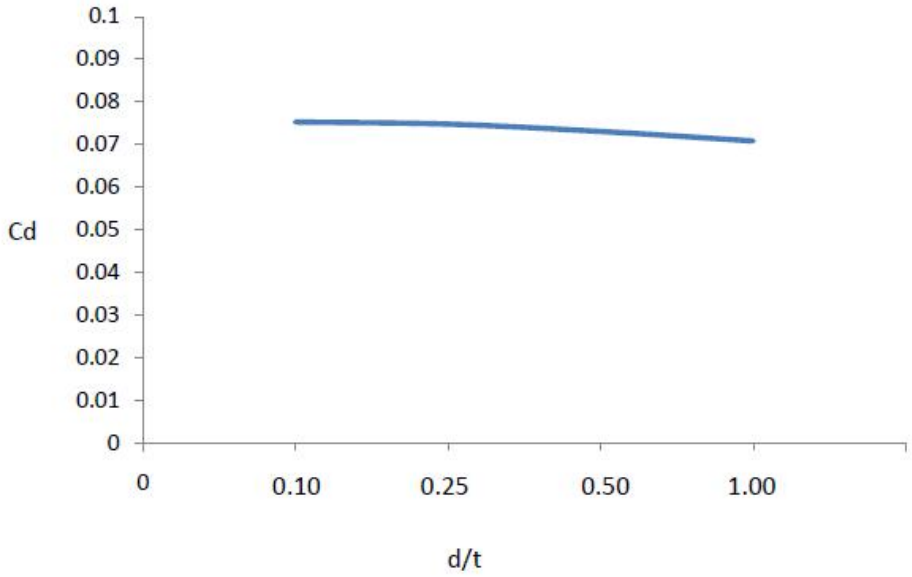

Figure 4.51: Computed average values of drag coefficient in the simulation with symmetric pulsed filament

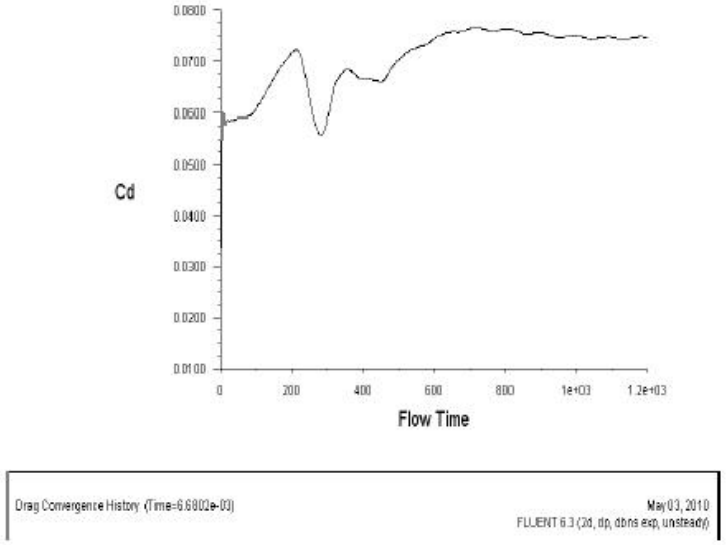

(a) $\frac{d}{t} = 0.10$

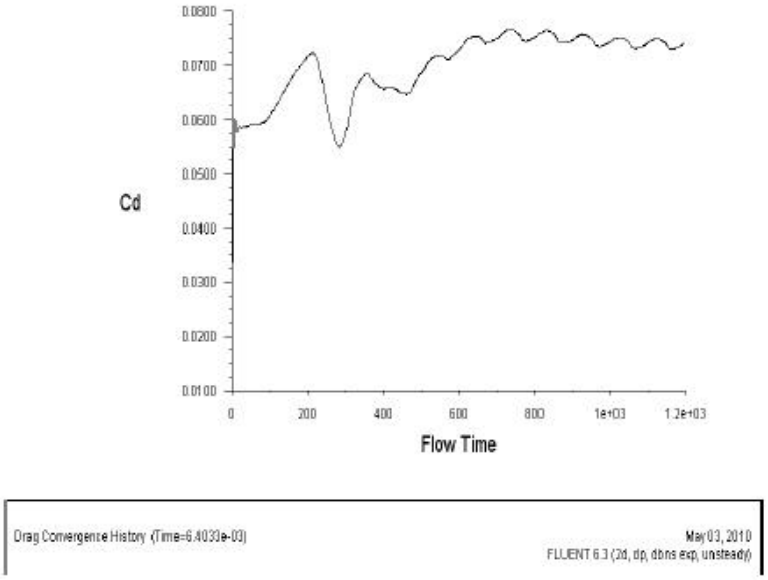

(b) $\frac{d}{t} = 0.25$

Figure 4.52: Computed drag coefficient with flow time (symmetric pulsed filament) 1

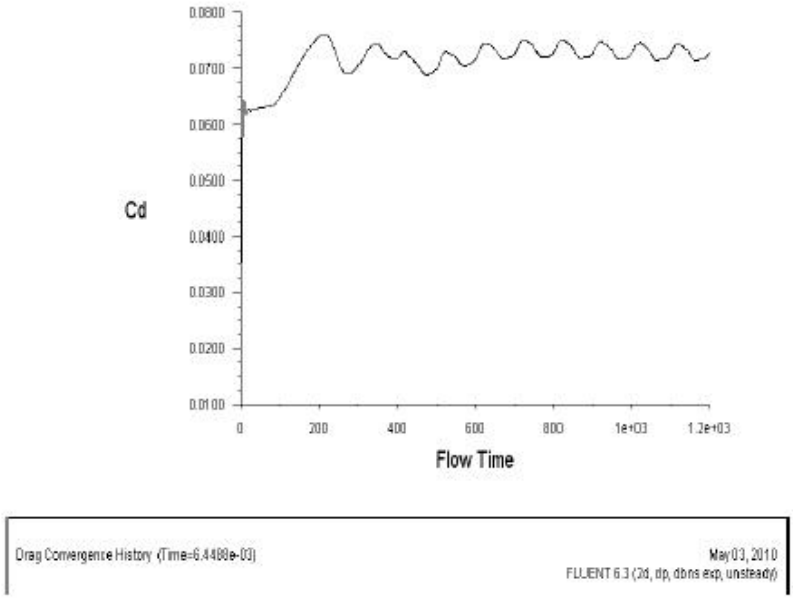

(a) $\frac{d}{t} = 0.50$

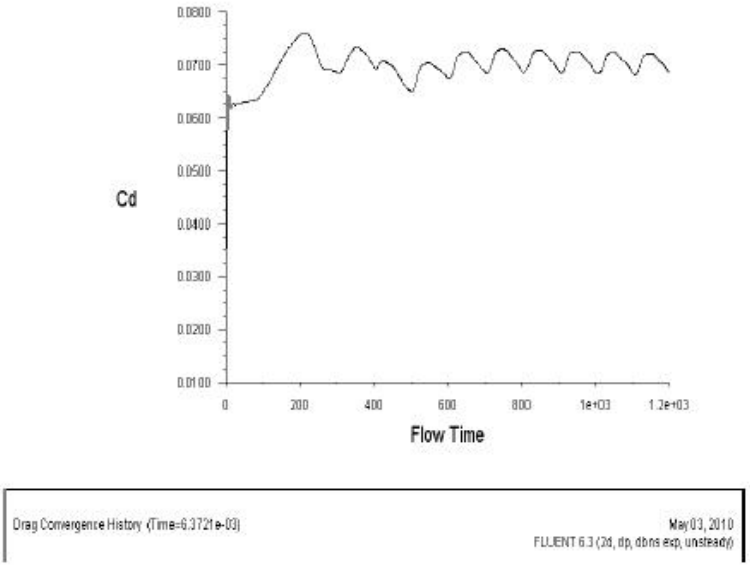

(b) $\frac{d}{t} = 1.00$

Figure 4.53: Computed drag coefficient with flow time (symmetric pulsed filament) 2

4.4 Asymmetric Pulsed Filament

4.4.1 Parameters of Flow Field Analysis

Table 4.6: Asymmetric Pulsed Filament

Type Description	$\frac{d}{t}$	$\frac{l}{t}$	$\frac{L}{t}$	$\frac{h}{t}$
pulsed filament (symmetric)	0.10 0.25 0.50 1.00	1	2	0.25

The length of each filament and the distance between consecutive filaments are constant. The position of the filament relative to airfoil is asymmetric. In the conditions of $\frac{d}{t} = 0.10$, $\frac{d}{t} = 0.25$, and $\frac{d}{t} = 0.50$, the filament would pass over the airfoil in upper region. Furthermore, there are some distance between filament and airfoil when $\frac{d}{t} = 0.10$ and $\frac{d}{t} = 0.25$.

Figures 4.54 to 4.73 are the Mach number, pressure, temperature and enlarged density contours with numerical schlieren images for these four different diameter pulsed filament cases.

4.4.2 Case 1 ($\frac{d}{t} = 0.10$)

From Figures 4.54 to 4.58, the asymmetric pulsed filament is added into the flow region. Figures 4.54 and 4.56 show the series of filaments without deformed are above the stripping-shaped numerical error in the second weak shock, which point to the the influence of stripping-shaped numerical error mentioned in Chapters 4.2 and 4.3.

4.4.3 Case 2 ($\frac{d}{t} = 0.25$)

It points out that the filaments deformed after expansion in Figures 4.59 to 4.63. In Figure 4.63, there are curves formed in the filament after the expansion fan.

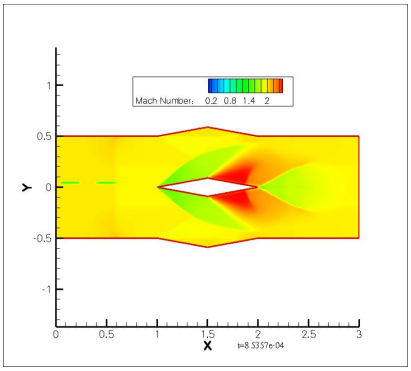

(a) in the 150 time steps

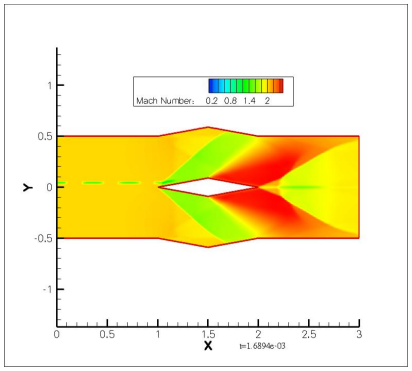

(b) in the 300 time steps

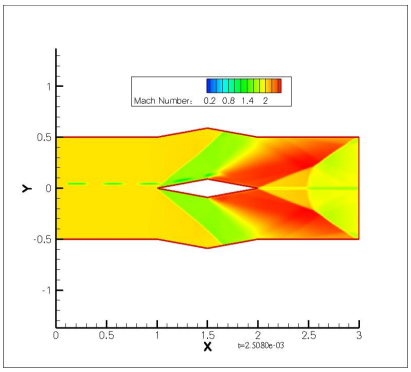

(c) in the 450 time steps

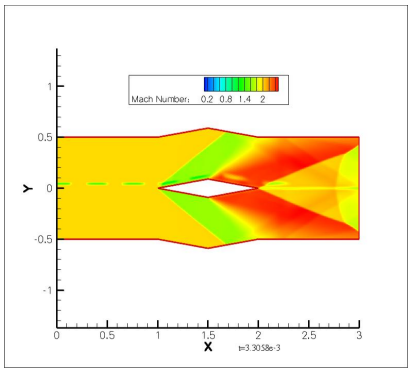

(d) in the 600 time steps

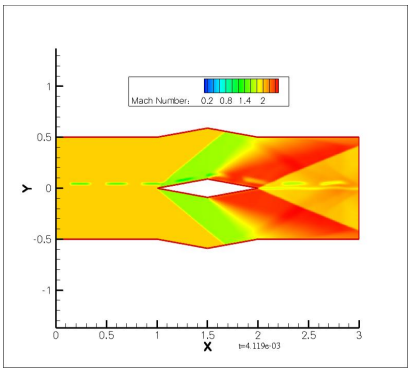

(e) in the 750 time steps

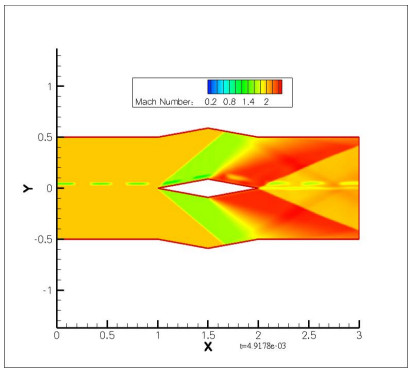

(f) in the 900 time steps

Figure 4.54: Six Mach number contours for the flow simulation with the asymmetric pulsed filament ($\frac{d}{t} = 0.10$)

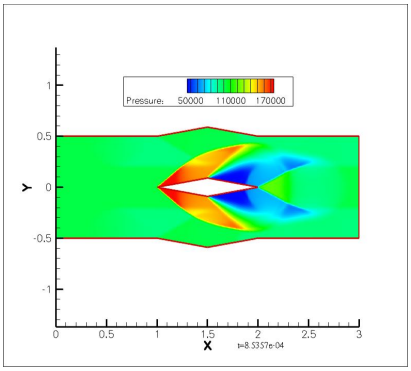

(a) in the 150 time steps

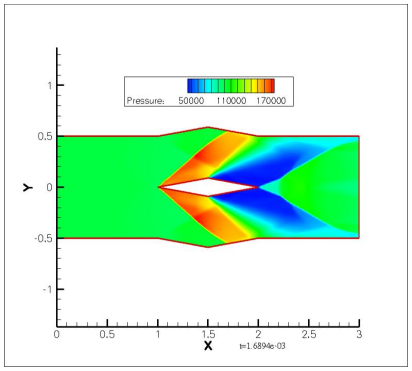

(b) in the 300 time steps

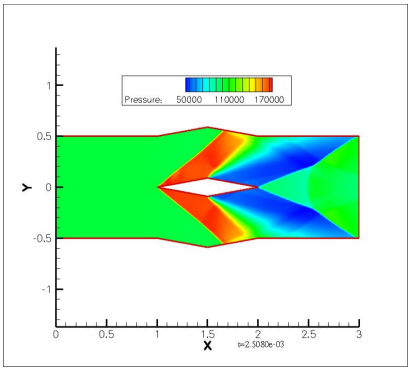

(c) in the 450 time steps

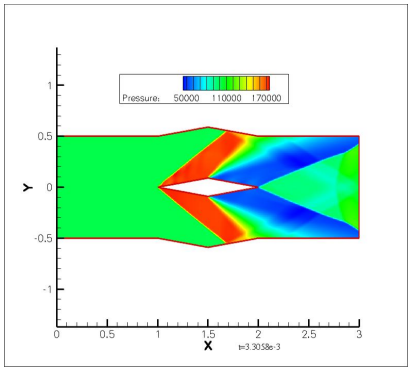

(d) in the 600 time steps

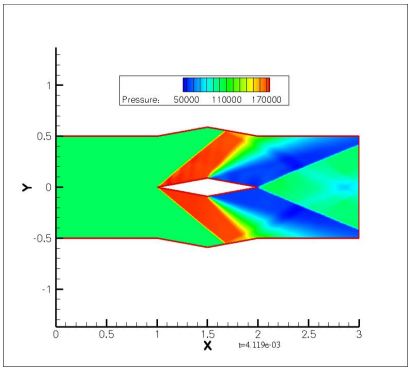

(e) in the 750 time steps

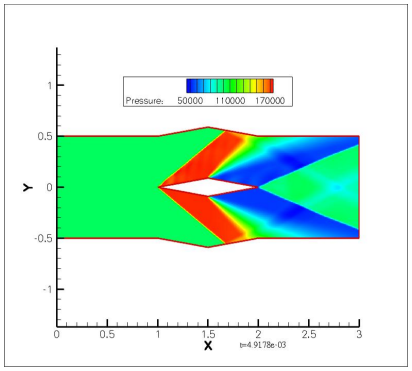

(f) in the 900 time steps

Figure 4.55: Six pressure contours for the flow simulation with the asymmetric pulsed filament ($\frac{d}{t} = 0.10$)

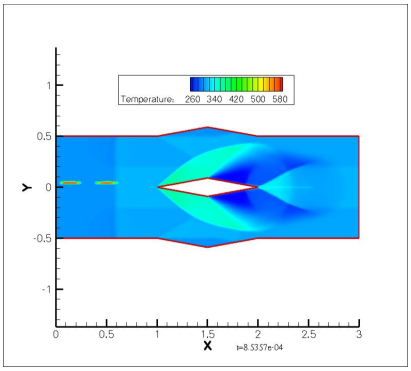

(a) in the 150 time steps

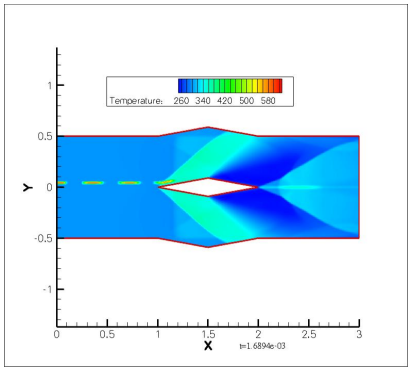

(b) in the 300 time steps

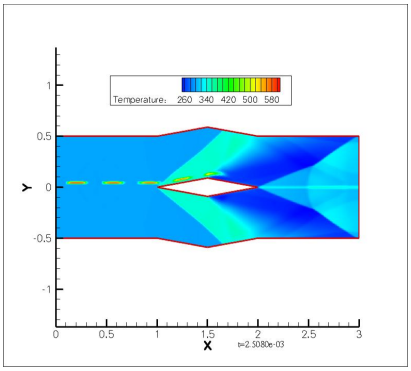

(c) in the 450 time steps

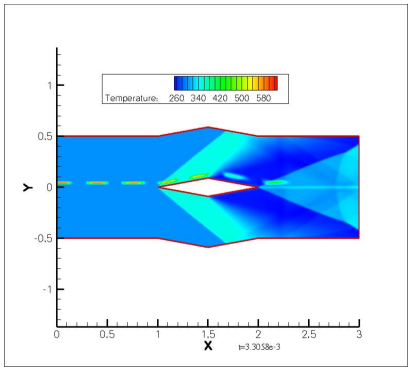

(d) in the 600 time steps

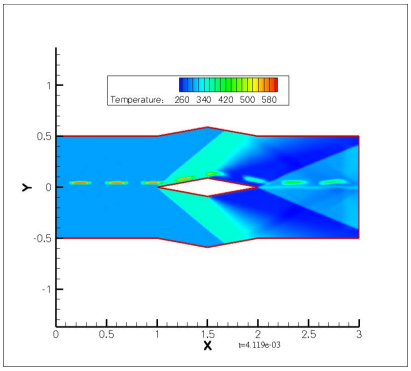

(e) in the 750 time steps

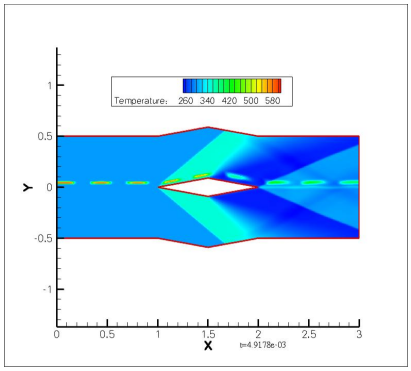

(f) in the 900 time steps

Figure 4.56: Six temperature contours for the flow simulation with the asymmetric pulsed filament ($\frac{d}{t} = 0.10$)

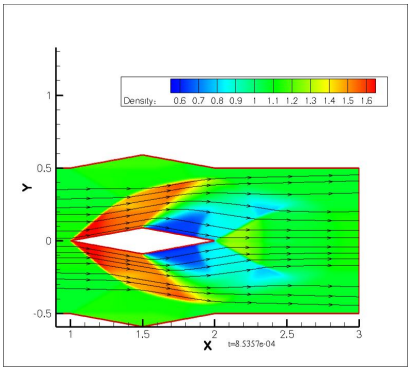

(a) in the 150 time steps

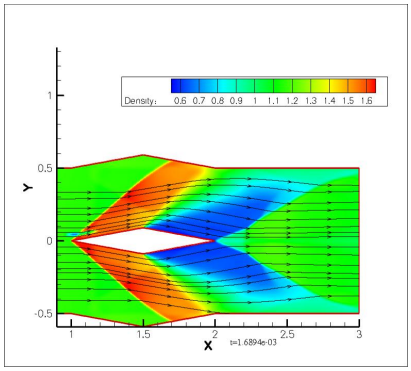

(b) in the 300 time steps

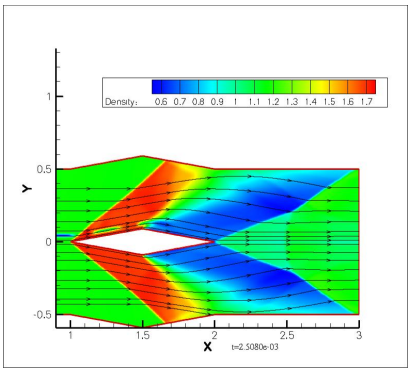

(c) in the 450 time steps

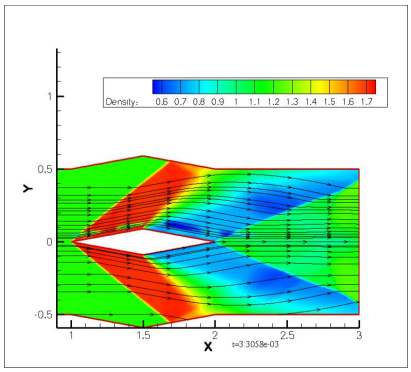

(d) in the 600 time steps

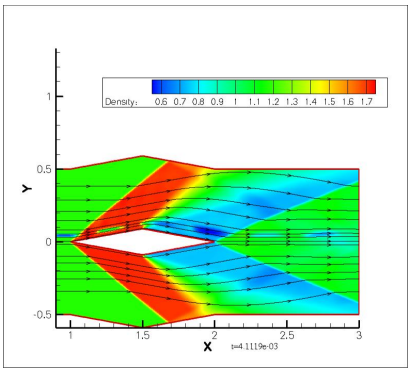

(e) in the 750 time steps

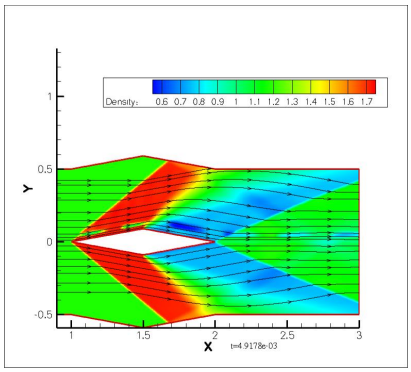

(f) in the 900 time steps

Figure 4.57: Six enlarged density contours for the flow simulation with the asymmetric pulsed filament ($\frac{d}{t} = 0.10$)

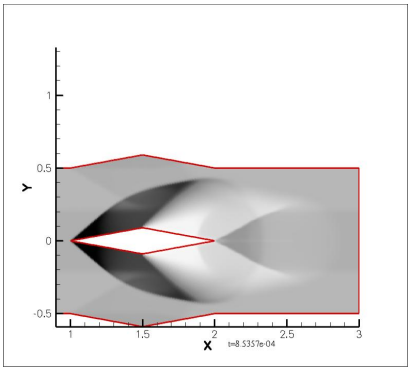

(a) in the 150 time steps

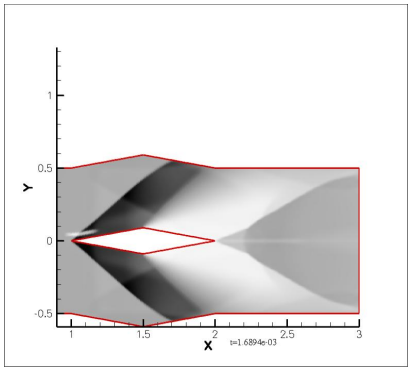

(b) in the 300 time steps

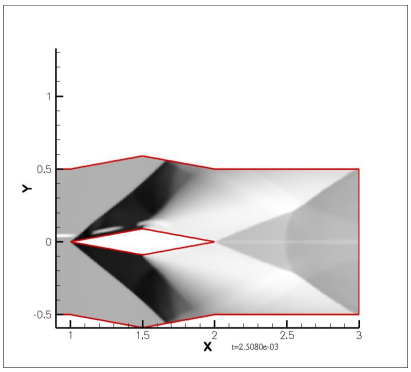

(c) in the 450 time steps

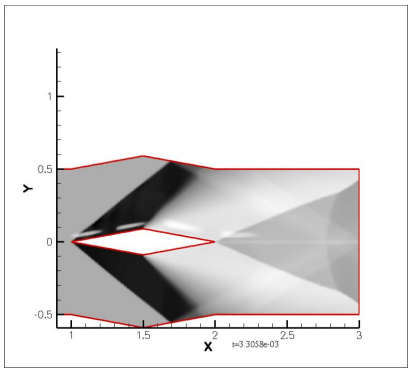

(d) in the 600 time steps

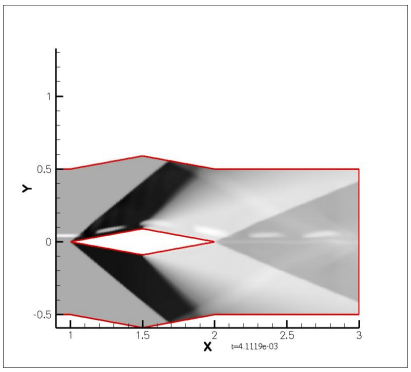

(e) in the 750 time steps

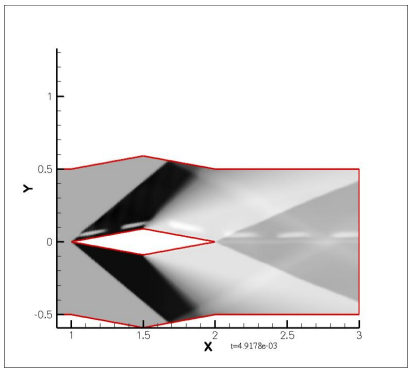

(f) in the 900 time steps

Figure 4.58: Six enlarged numerical schilieren contours for the flow simulation with the asymmetric pulsed filament ($\frac{d}{t} = 0.10$)

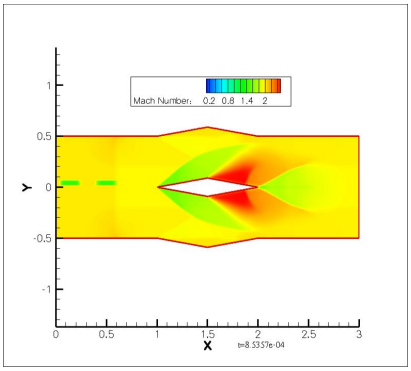

(a) in the 150 time steps

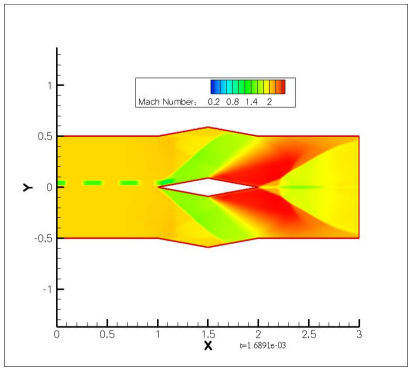

(b) in the 300 time steps

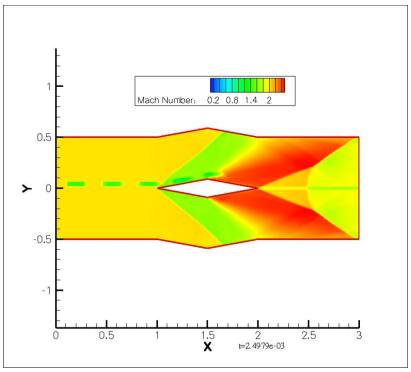

(c) in the 450 time steps

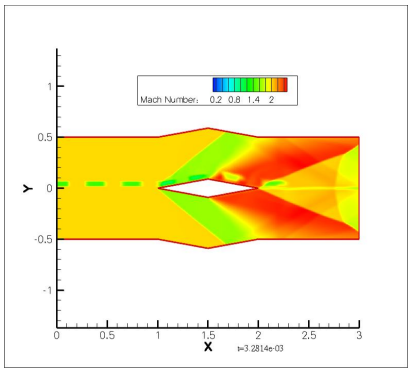

(d) in the 600 time steps

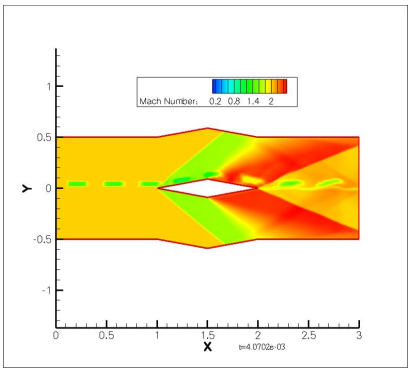

(e) in the 750 time steps

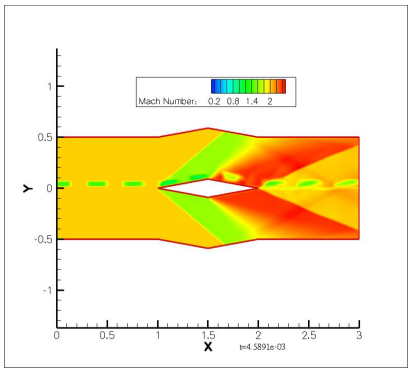

(f) in the 900 time steps

Figure 4.59: Six Mach number contours for the flow simulation with the asymmetric pulsed filament ($\frac{d}{t} = 0.25$)

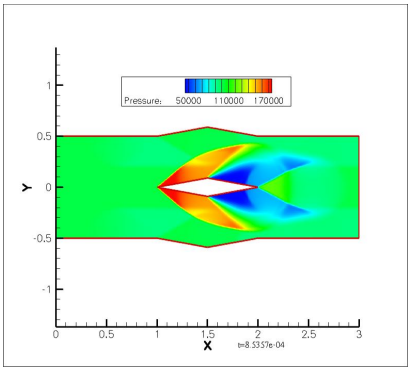

(a) in the 150 time steps

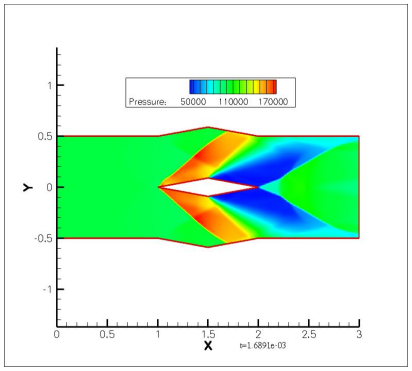

(b) in the 300 time steps

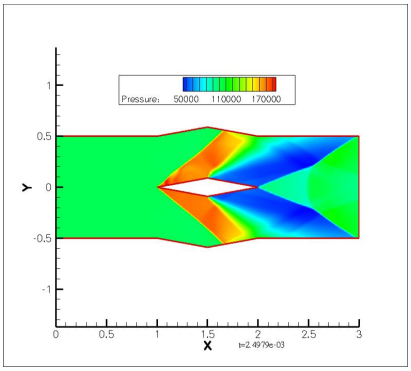

(c) in the 450 time steps

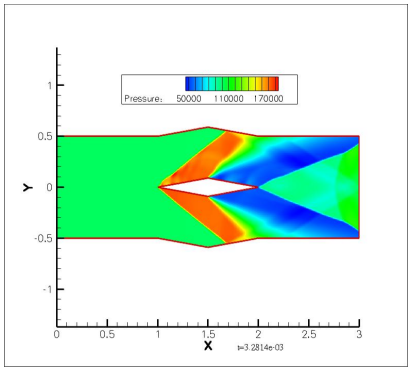

(d) in the 600 time steps

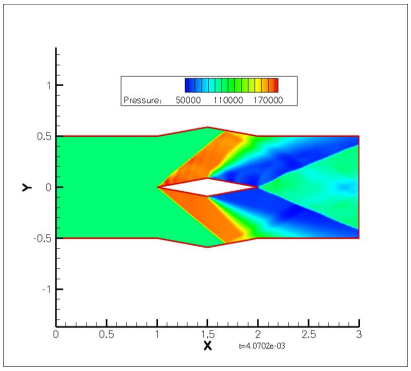

(e) in the 750 time steps

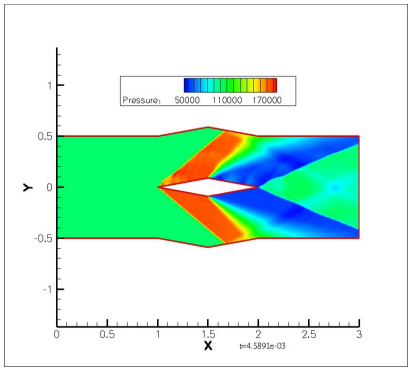

(f) in the 900 time steps

Figure 4.60: Six pressure contours for the flow simulation with the asymmetric pulsed filament ($\frac{d}{t} = 0.25$)

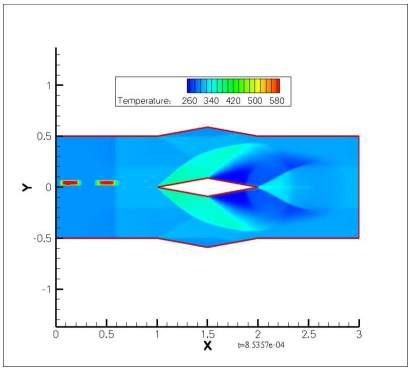

(a) in the 150 time steps

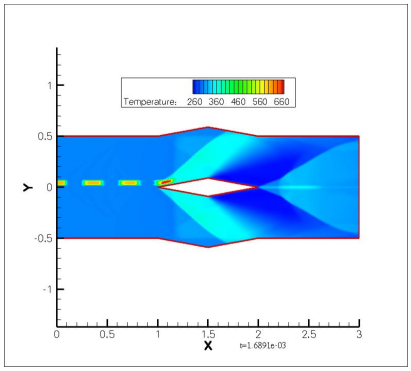

(b) in the 300 time steps

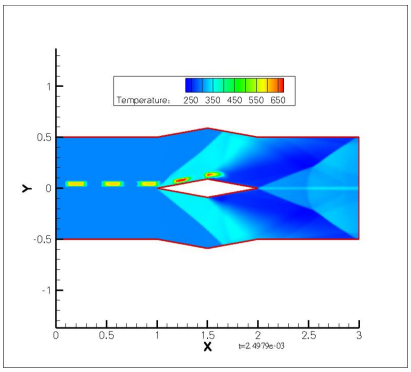

(c) in the 450 time steps

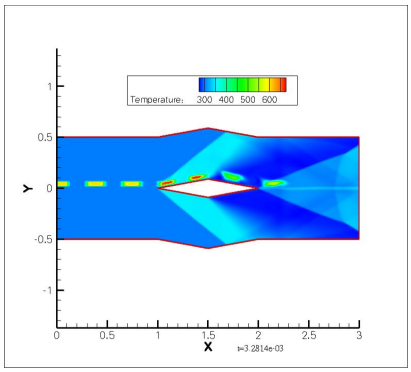

(d) in the 600 time steps

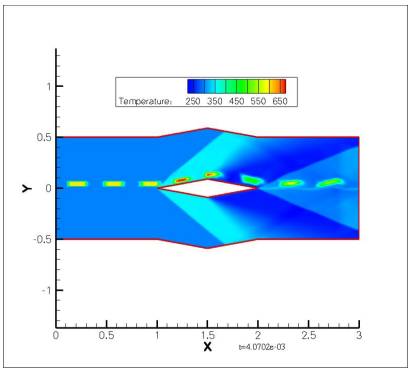

(e) in the 750 time steps

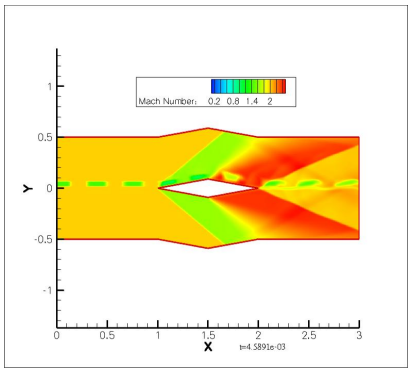

(f) in the 900 time steps

Figure 4.61: Six temperature contours for the flow simulation with the asymmetric pulsed filament ($\frac{d}{t} = 0.25$)

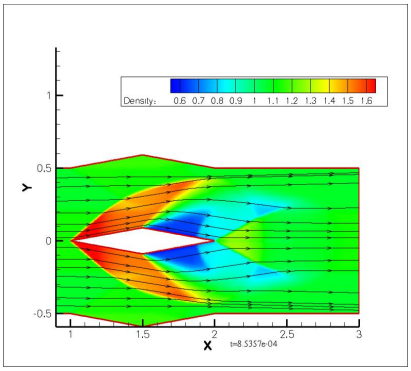

(a) in the 150 time steps

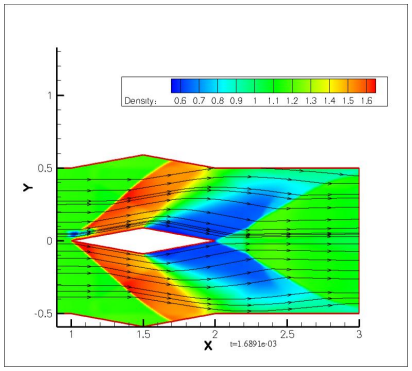

(b) in the 300 time steps

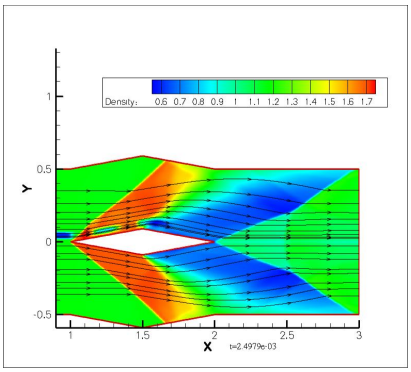

(c) in the 450 time steps

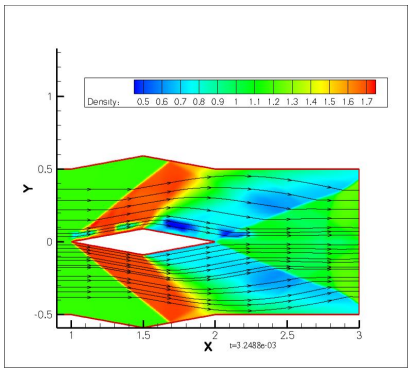

(d) in the 600 time steps

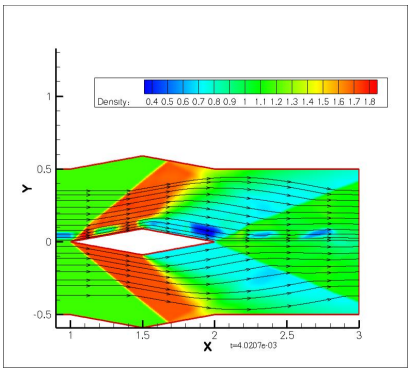

(e) in the 750 time steps

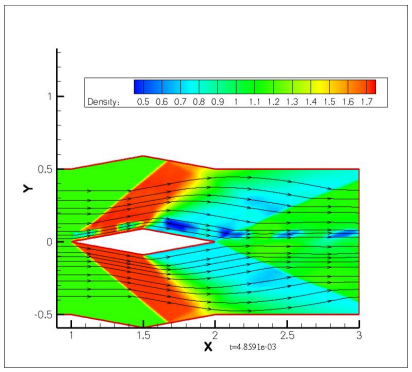

(f) in the 900 time steps

Figure 4.62: Six enlarged density contours for the flow simulation with the asymmetric pulsed filament ($\frac{d}{t} = 0.25$)

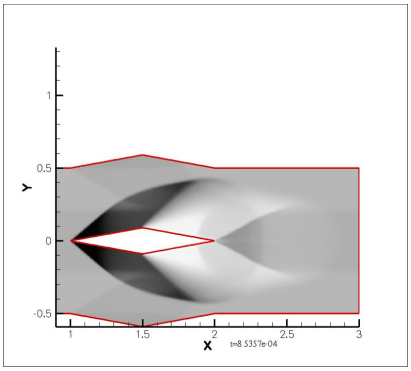

(a) in the 150 time steps

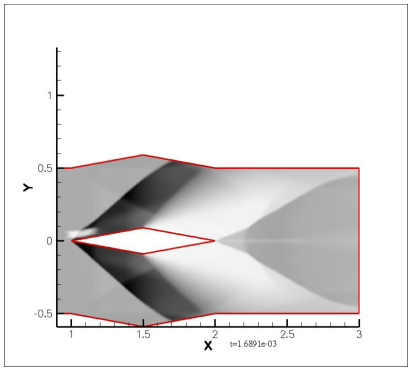

(b) in the 300 time steps

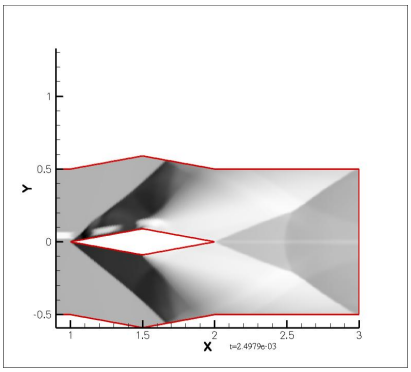

(c) in the 450 time steps

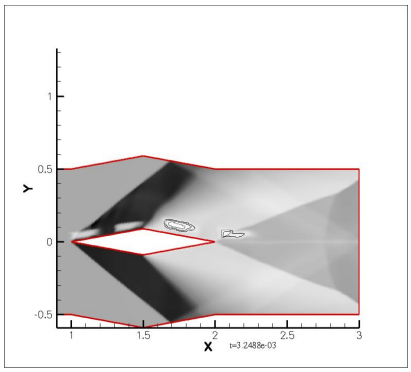

(d) in the 600 time steps

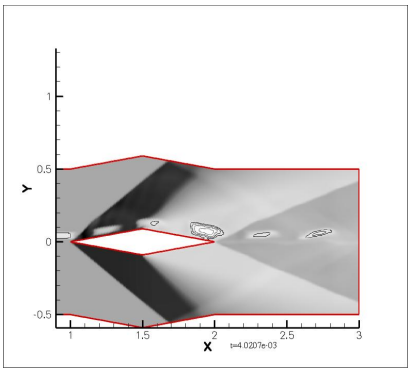

(e) in the 750 time steps

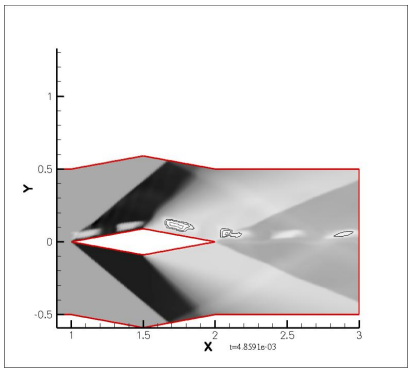

(f) in the 900 time steps

Figure 4.63: Six enlarged numerical schilieren contours for the flow simulation with the asymmetric pulsed filament ($\frac{d}{t} = 0.25$)

4.4.4 Case 3 ($\frac{d}{t} = 0.50$)

Figures 4.66 and 4.66 shows the influence of the stripping numerical error on the filaments very clear. Figures 4.67 and 4.68 shows the bigger deformation and larger cueves of filaments.

4.4.5 Case 4 ($\frac{d}{t} = 1.00$)

Because $\frac{d}{t} = 1.00$, the series of pulsed filaments would pass over the airfoil in this case. Interesting deformed irregular "bullet"-shaped filaments can be seen in Figures 4.69 to 4.73.

Some common features can be observed during the interaction:

1. The first shock is formed at the front point of the diamond-shaped airfoil body with the flow.
2. The expansion fan is formed over the corner of the diamond-shaped airfoil.
3. The second shock is formed at the end point of the diamond-shaped airfoil.
4. Asymmetric pulsed filament is formed.
5. Mach number will decrease after the shock wave and increases through the expansion both in the flow and filament region.
6. Pressure and temperature are just on the contrary, increasing after the shock, and then decreasing in the expansion both in the flow and filament region .
7. The progressional contact formed between the flow and the filament
8. In the Figures 4.69 to 4.73, the "almost normal shock" is observed in the leading edge of the airfoil. Like analysis in the sections above, the "normal shock" should be the detached shock, but appears to be "attached" due to the finite size of the cells.
9. The filament (higher temperature and lower density region) makes the angle of the expansion fan bigger.

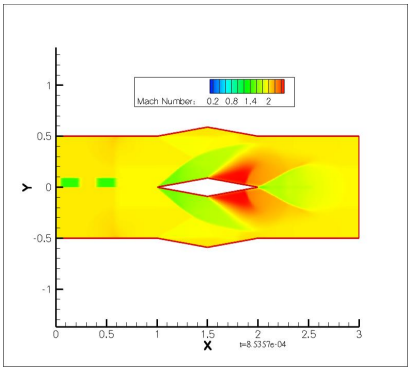

(a) in the 150 time steps

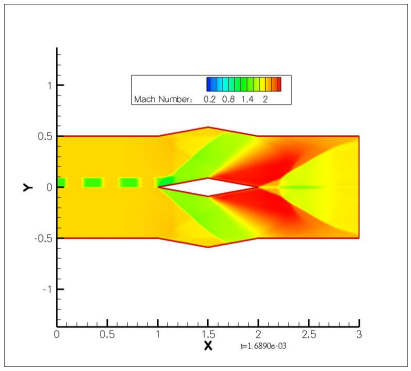

(b) in the 300 time steps

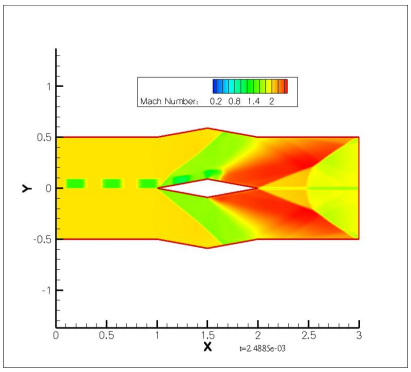

(c) in the 450 time steps

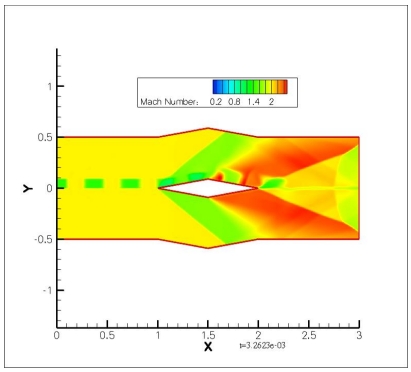

(d) in the 600 time steps

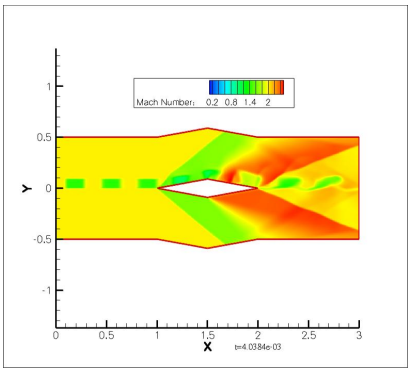

(e) in the 750 time steps

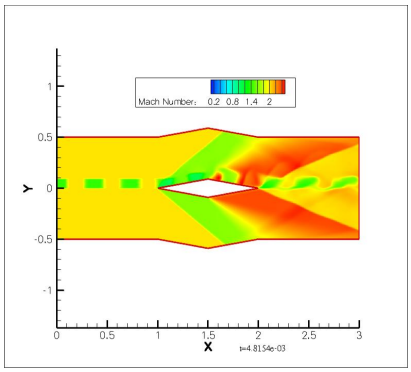

(f) in the 900 time steps

Figure 4.64: Six Mach number contours for the flow simulation with the asymmetric pulsed filament ($\frac{d}{t} = 0.50$)

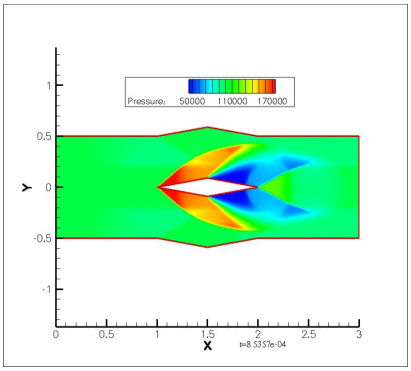

(a) in the 150 time steps

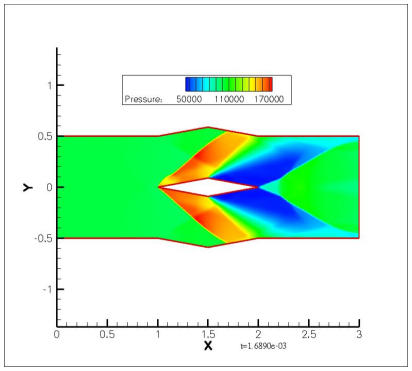

(b) in the 300 time steps

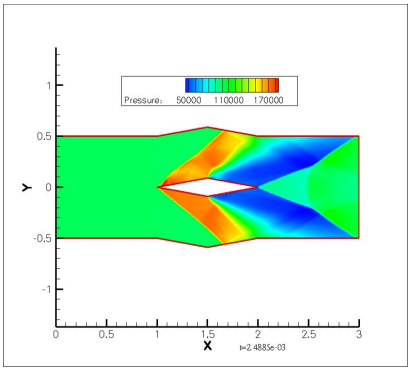

(c) in the 450 time steps

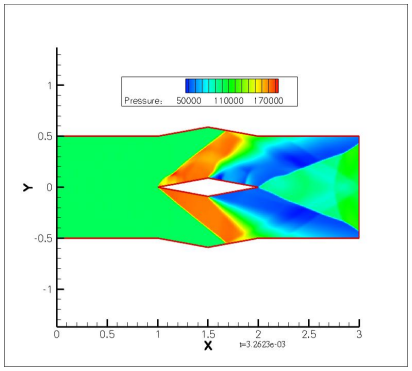

(d) in the 600 time steps

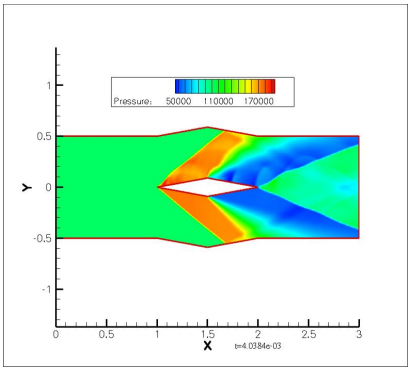

(e) in the 750 time steps

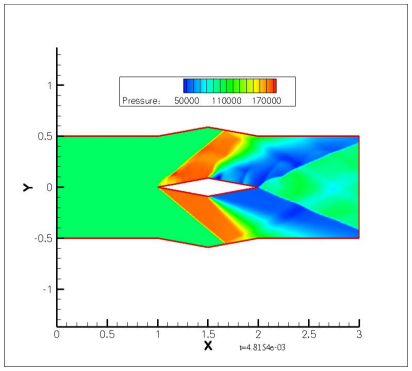

(f) in the 900 time steps

Figure 4.65: Six pressure contours for the flow simulation with the asymmetric pulsed filament ($\frac{d}{t} = 0.50$)

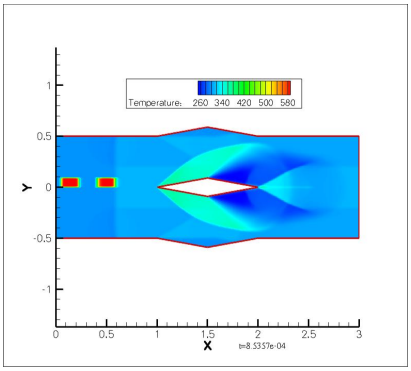

(a) in the 150 time steps

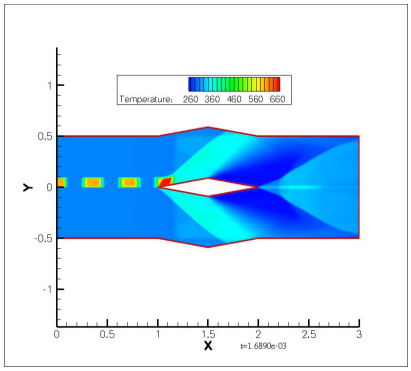

(b) in the 300 time steps

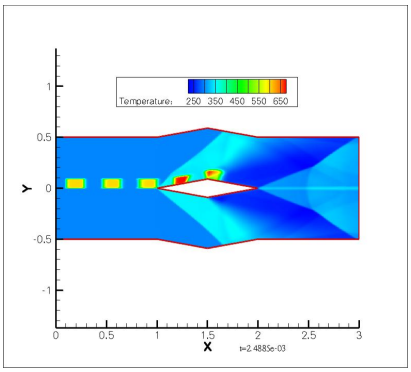

(c) in the 450 time steps

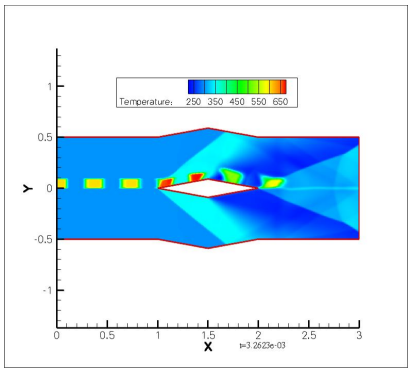

(d) in the 600 time steps

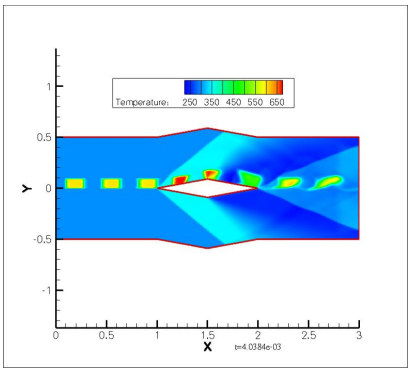

(e) in the 750 time steps

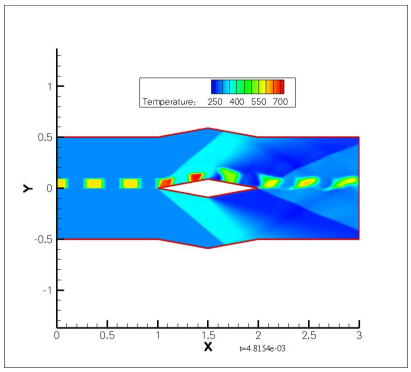

(f) in the 900 time steps

Figure 4.66: Six temperature contours for the flow simulation with the asymmetric pulsed filament ($\frac{d}{t} = 0.50$)

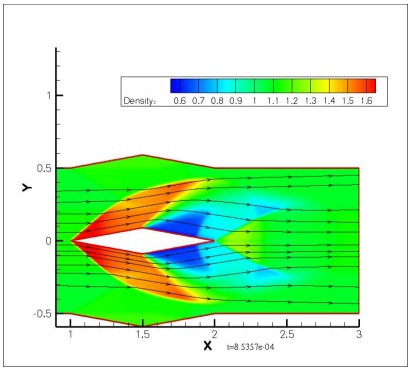

(a) in the 150 time steps

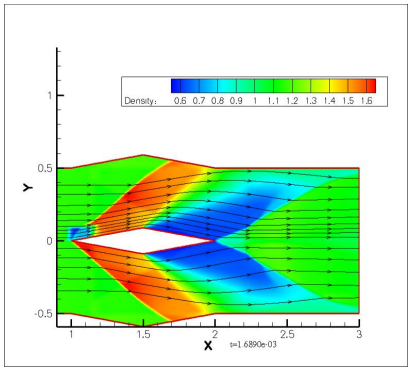

(b) in the 300 time steps

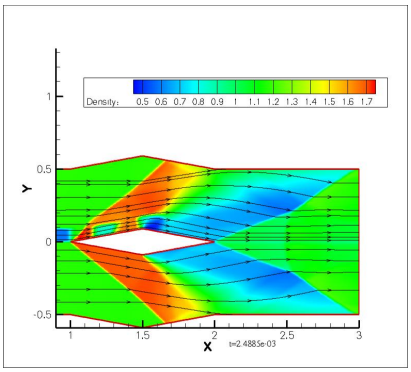

(c) in the 450 time steps

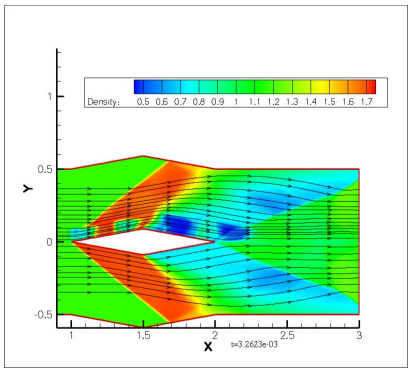

(d) in the 600 time steps

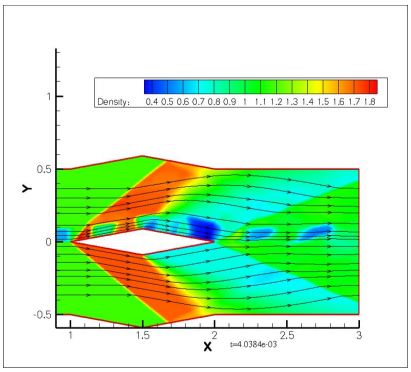

(e) in the 750 time steps

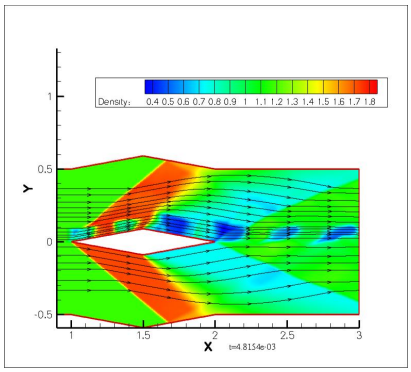

(f) in the 900 time steps

Figure 4.67: Six enlarged density contours for the flow simulation with the asymmetric pulsed filament ($\frac{d}{t} = 0.50$)

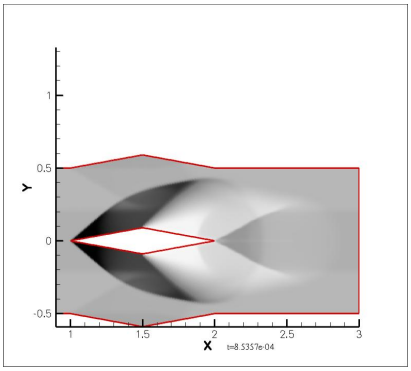

(a) in the 150 time steps

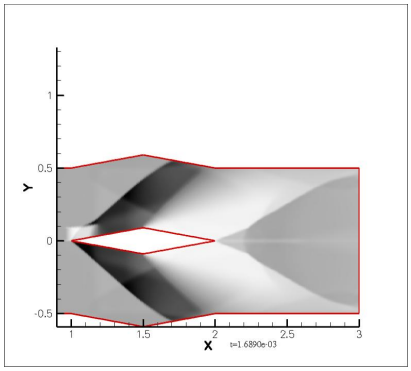

(b) in the 300 time steps

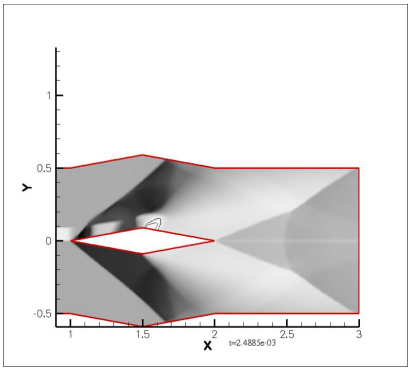

(c) in the 450 time steps

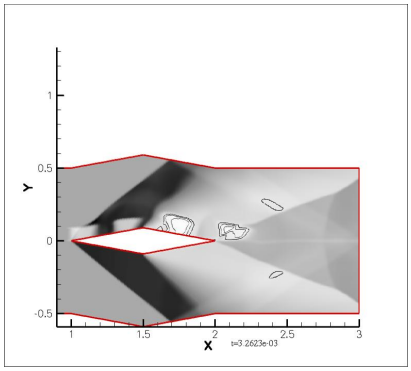

(d) in the 600 time steps

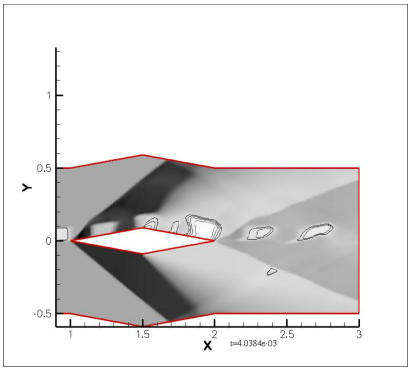

(e) in the 750 time steps

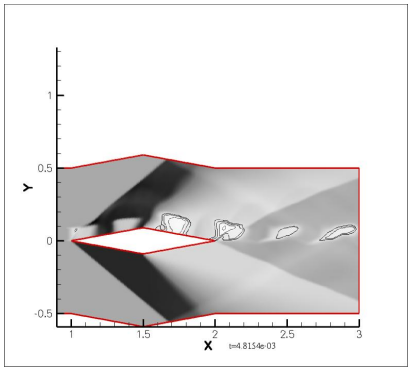

(f) in the 900 time steps

Figure 4.68: Six enlarged numerical schilieren contours for the flow simulation with the asymmetric pulsed filament ($\frac{d}{t} = 0.50$)

10. The streamwise distortion of the filament following the second shock is quite apparent. This is due to the variation in arrival time of the front face of the filament at the shocks.

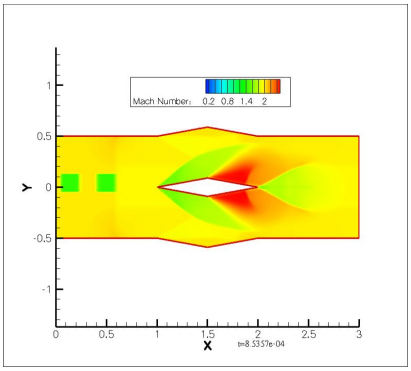

(a) in the 150 time steps

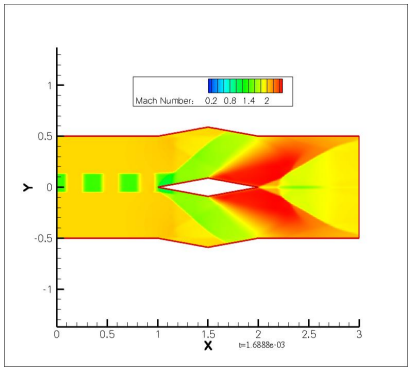

(b) in the 300 time steps

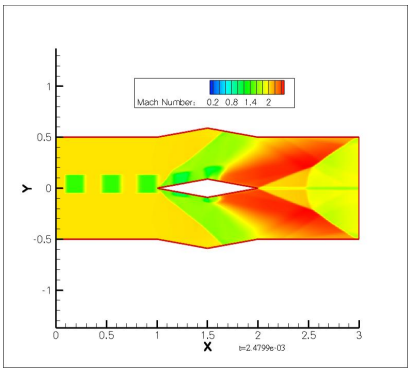

(c) in the 450 time steps

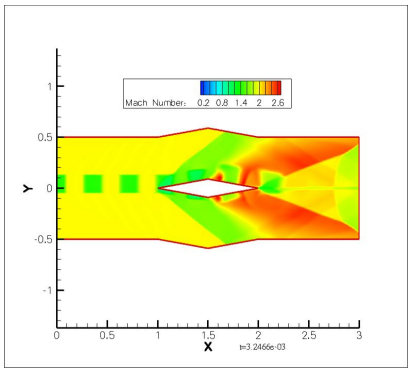

(d) in the 600 time steps

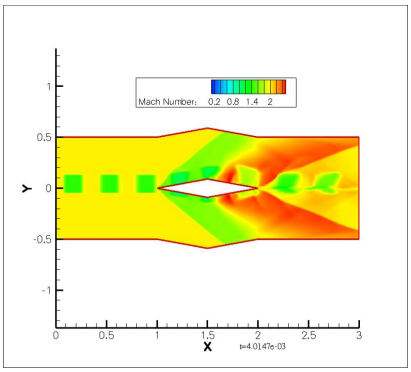

(e) in the 750 time steps

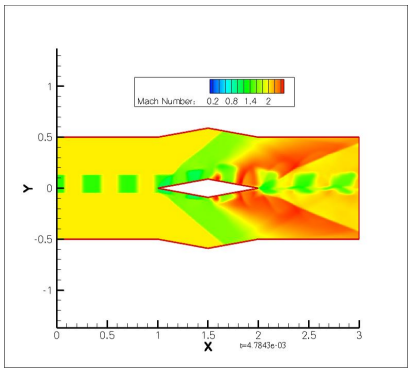

(f) in the 900 time steps

Figure 4.69: Six Mach number contours for the flow simulation with the asymmetric pulsed filament ($\frac{d}{t} = 1.00$)

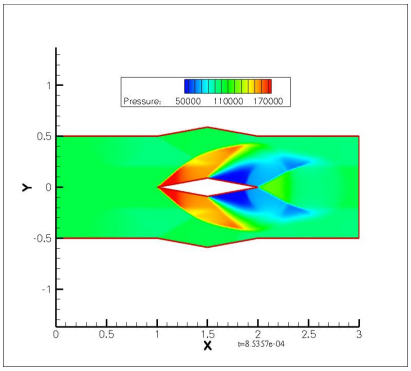

(a) in the 150 time steps

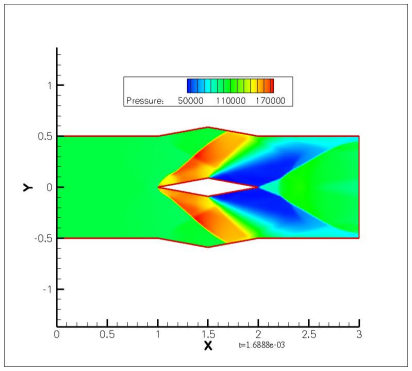

(b) in the 300 time steps

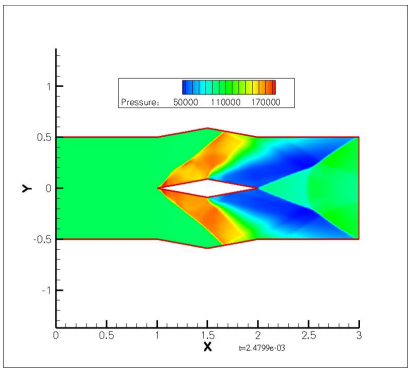

(c) in the 450 time steps

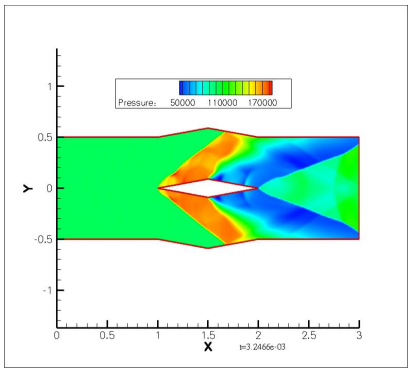

(d) in the 600 time steps

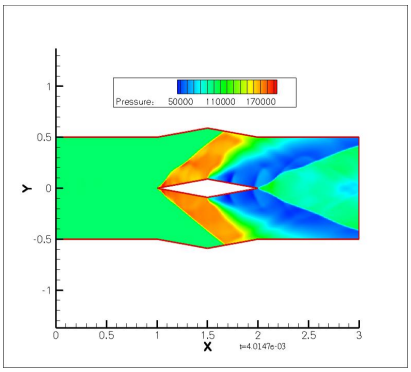

(e) in the 750 time steps

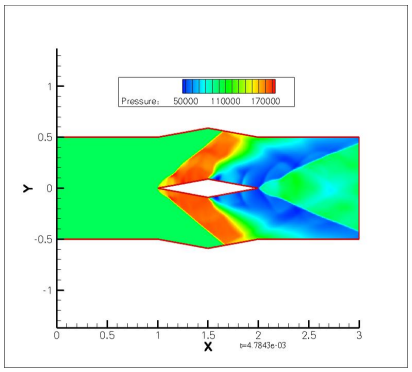

(f) in the 900 time steps

Figure 4.70: Six pressure contours for the flow simulation with the asymmetric pulsed filament ($\frac{d}{t} = 1.00$)

4.4.6 Drag Coefficient Analysis for Asymmetric Pulsed Filament Added

The computed drag coefficient of four different types of the asymmetric filaments with flow time are shown in Figures 4.75 and 4.76. It also can be observed the regular curved lines in the figure, i.e, the value computed in the FLUENT coding for asymmetric pulsed filament is instantaneous. But the curved diffrences among the diffirent types of the filament are not so evident like the symmetric pulsed filament. Table 4.7 and Figure 4.74 show the average values of the calculated results of the drag coefficient for all four cases (Average drag coefficient after the time steps 750). The drag coefficient will decrease as the height of the filaments increases. The difference in average drag coefficient between the $\frac{d}{t} = 0.10$ and $\frac{d}{t} = 1.00$ cases is 4.0%.

Table 4.7: Average results of drag coefficient in the simulation with asymmetric pulsed filament

$\frac{d}{t}$	drag coefficient
0.10	0.0741
0.25	0.0736
0.50	0.0727
1.00	0.0711

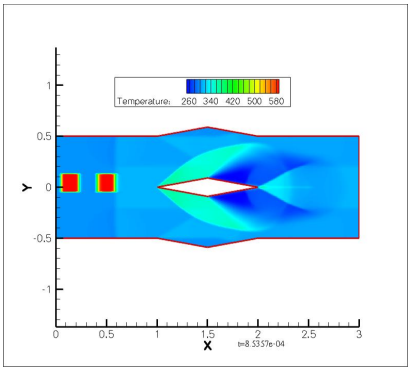

(a) in the 150 time steps

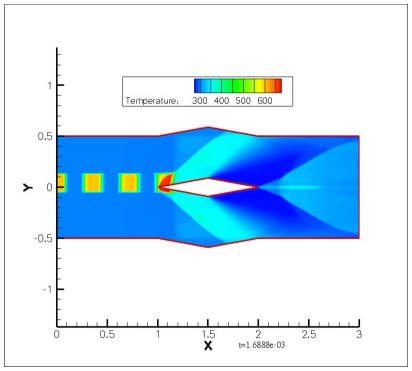

(b) in the 300 time steps

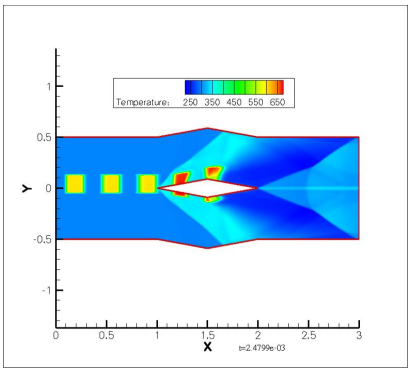

(c) in the 450 time steps

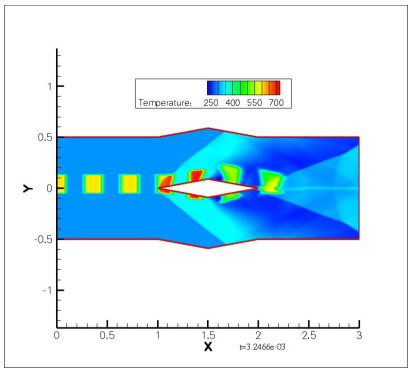

(d) in the 600 time steps

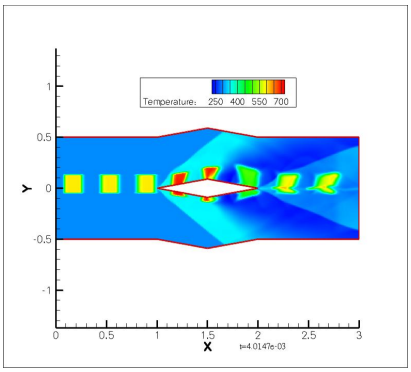

(e) in the 1 = 750 time steps

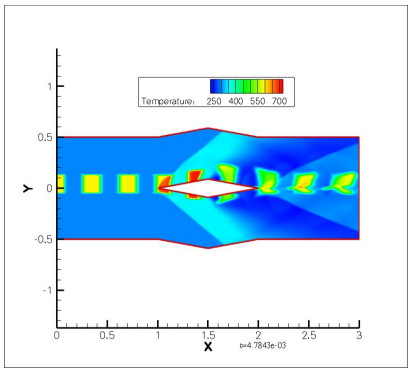

(f) in the 900 time steps

Figure 4.71: Six temperature contours for the flow simulation with the asymmetric pulsed filament ($\frac{d}{t} = 1.00$)

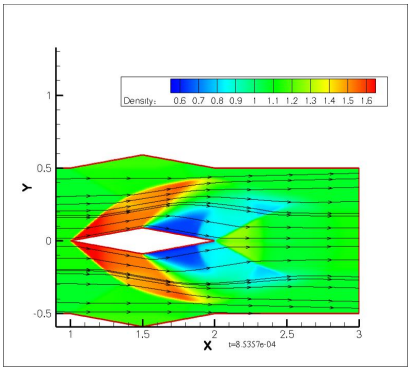

(a) in the 150 time steps

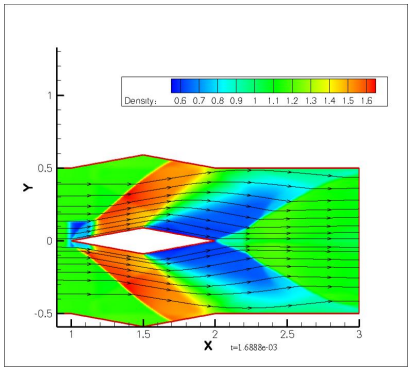

(b) in the 300 time steps

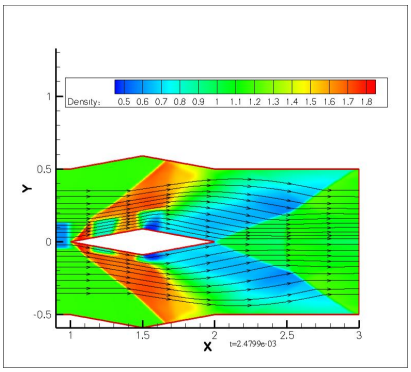

(c) in the 450 time steps

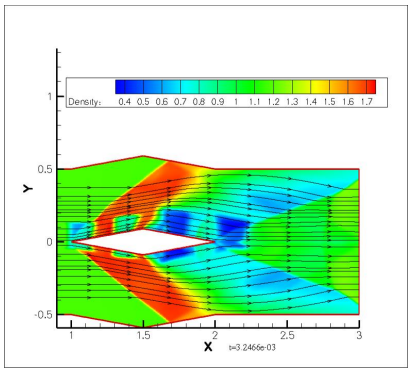

(d) in the 600 time steps

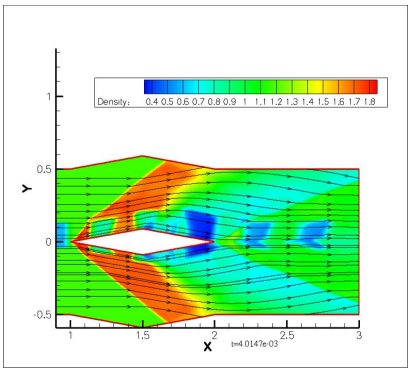

(e) in the 750 time steps

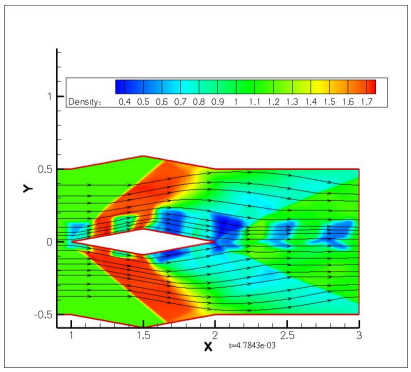

(f) in the 900 time steps

Figure 4.72: Six enlarged density contours for the flow simulation with the asymmetric pulsed filament ($\frac{d}{t} = 1.00$)

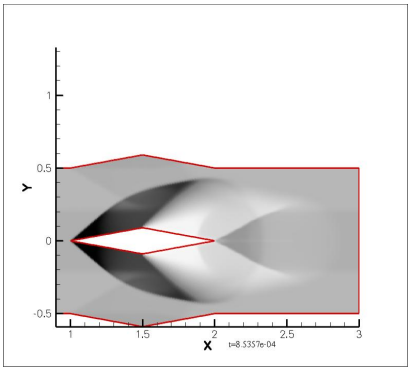

(a) in the 150 time steps

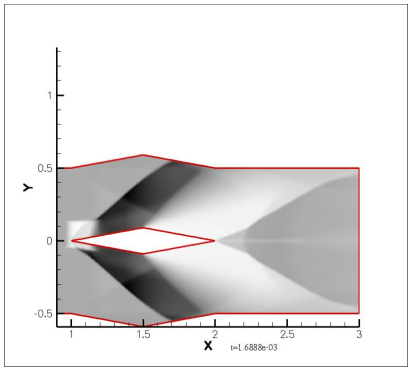

(b) in the 300 time steps

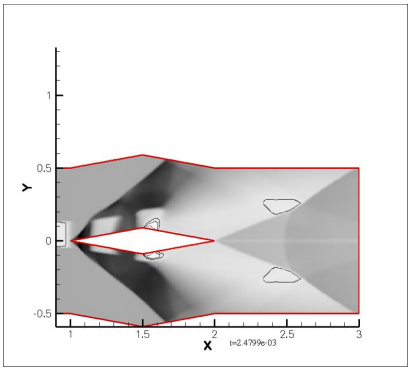

(c) in the 450 time steps

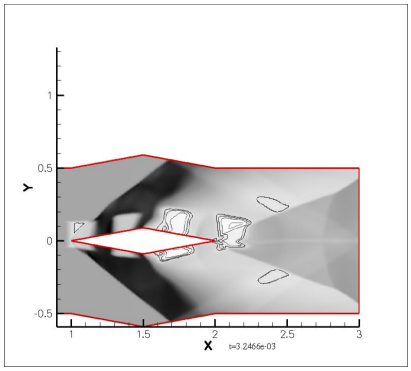

(d) in the 600 time steps

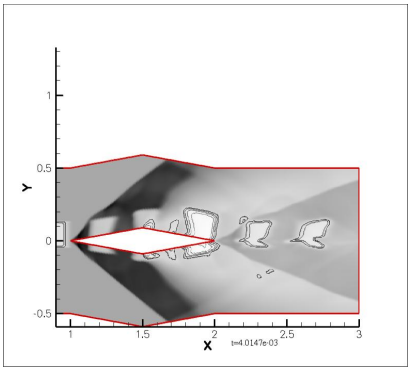

(e) in the 750 time steps

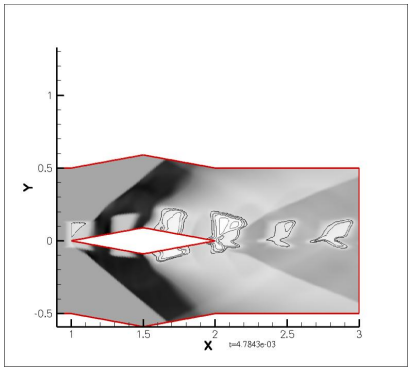

(f) in the 900 time steps

Figure 4.73: Six enlarged numerical schilieren contours for the flow simulation with the asymmetric pulsed filament ($\frac{d}{t} = 1.00$)

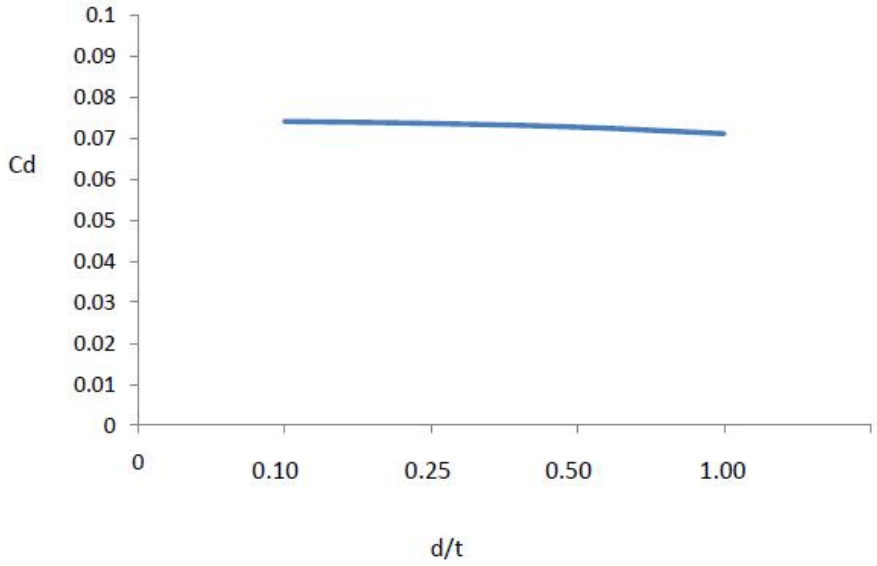

Figure 4.74: Computed average values of drag coefficient in the simulation with asymmetric pulsed filament

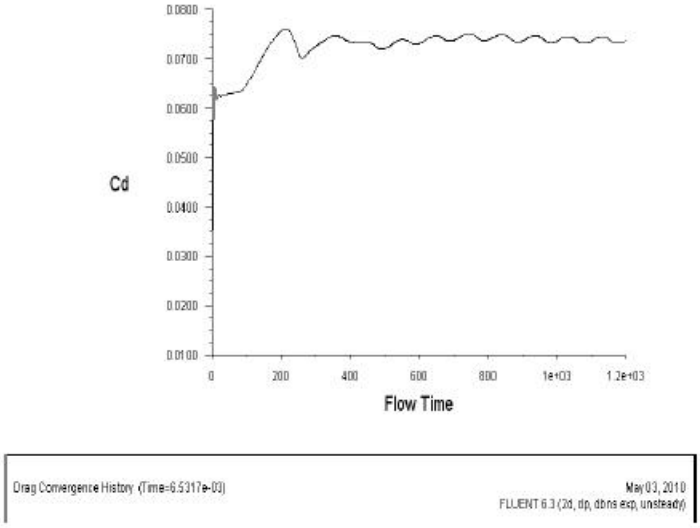

(a) $\frac{d}{t} = 0.10$

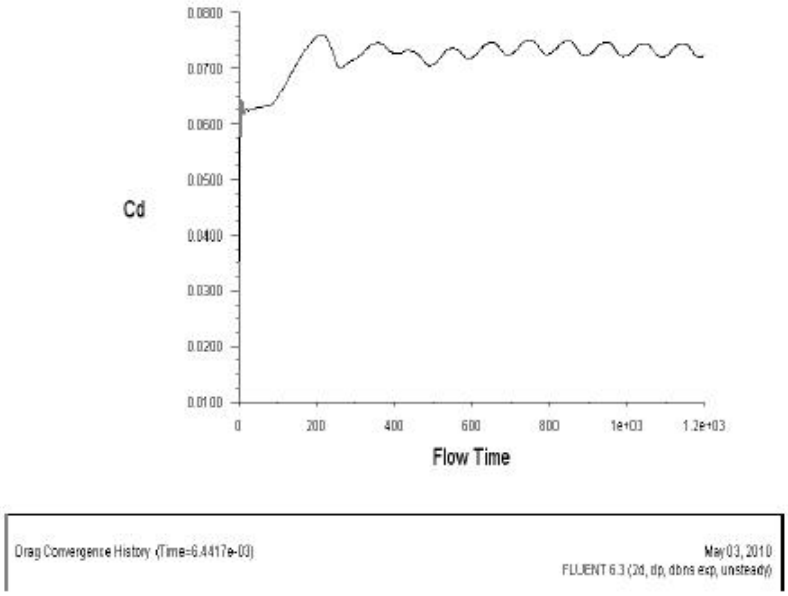

(b) $\frac{d}{t} = 0.25$

Figure 4.75: Computed drag coefficient with flow time (asymmetric plused filament) 1

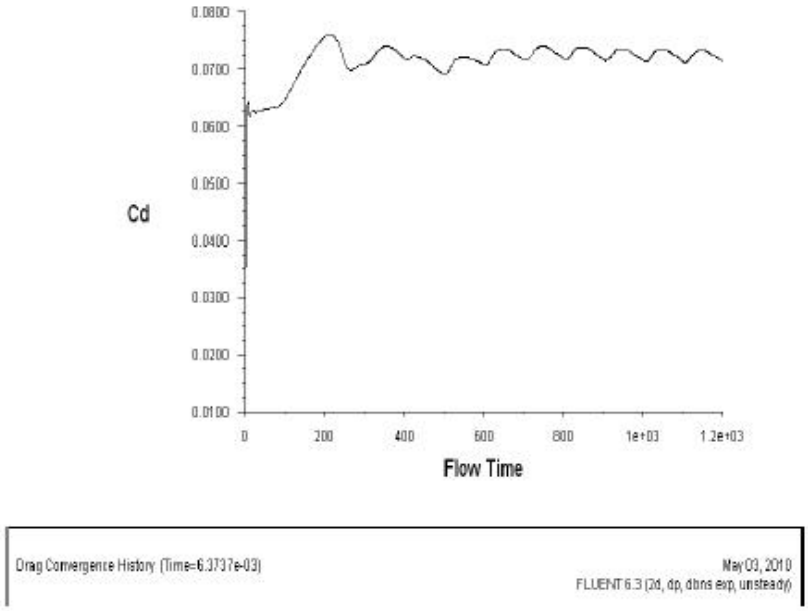

(a) $\frac{d}{t} = 0.50$

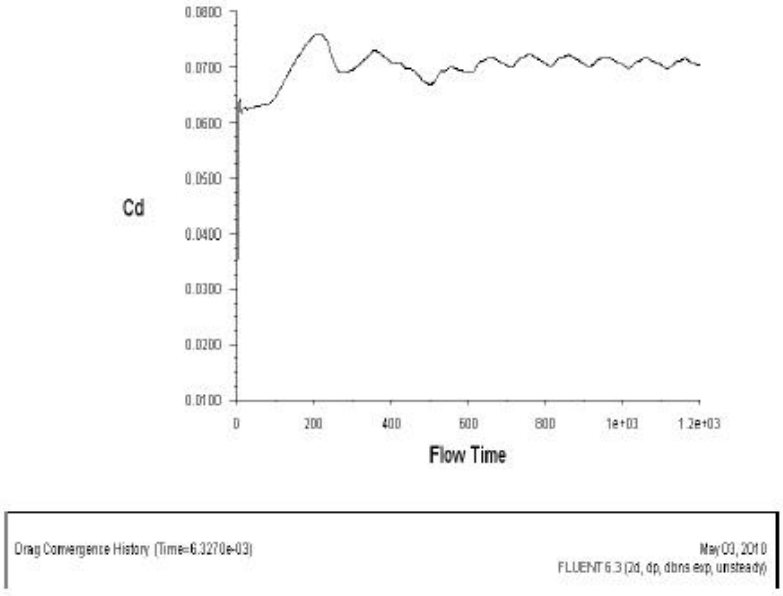

(b) $\frac{d}{t} = 1.00$

Figure 4.76: Computed drag coefficient with flow time (asymmetric plused filament) 2

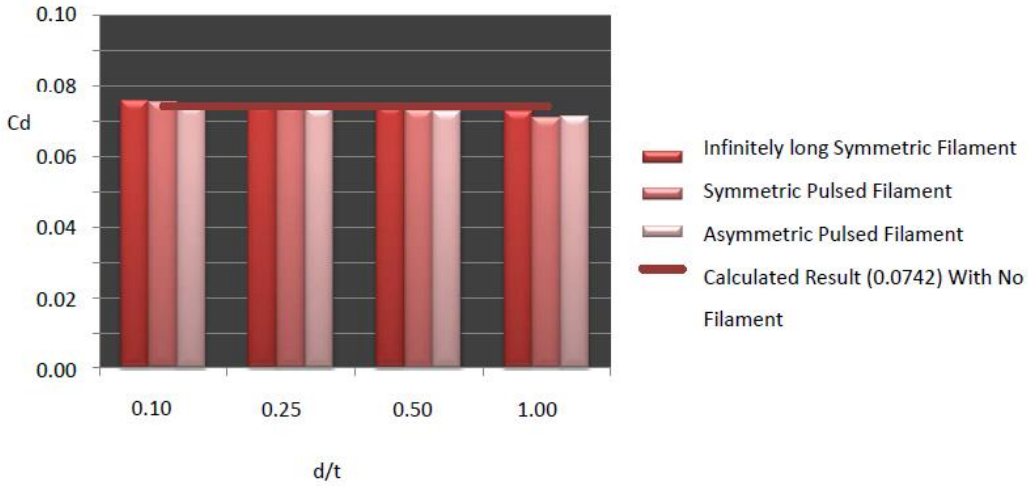

Figure 4.77: Comparisons of the computed average values of drag coefficient in the same $\frac{d}{t}$ cases with three different types of filaments (infinitely long symmetric, symmetric pulsed, asymmetric pulsed)

4.5 Results among infinitely long Filament, Symmetric Pulsed Filament and Asymmetric Pulsed Filament

Figure 4.77 compares the average values of the drag coefficient in the same $\frac{d}{t}$ cases with different types of the filaments (infinitely long symmetric, symmetric pulsed and asymmetric pulsed).

The conclusions may be summarized for all the results analysis in the above sections:

1. In the infinitely long filament cases, the value of the drag coefficient calculated in FLUENT coding is constant. However, for the pulsed filament cases, the computed results of the drag coefficient are unsteady and periodic.

2. All types of the filaments reduce the drag coefficient slightly with the $\frac{d}{t}$ increasing.

3. The percentage of the reduction for the drag coefficient with $\frac{d}{t} = 1.00$, which is compared to the no filament case, are 2.3%, 4.6% and 4.2% for the infinitely long symmetric filament, symmetric pulsed filament and asymmetric pulsed filament, respectively. For symmetric pulsed and asymmetric pulsed cases, the results are effectively identical since the accuracy is $\pm 2\%$.

Chapter 5

Conclusions and Future Work

5.1 Conclusions

Inviscid compressible supersonic flow over a two dimensional symmetric diamond-shape airfoil is studied in this research. Energy deposition is added at the inflow boundary in the simulation. The Mach number, pressure, temperature are obtained in both theoretical and numerical methods. The drag coefficient is also calculated.

In the simulation, the first oblique shock wave is formed at the left beginning point of the airfoil; the Prandtl-Meyer Expansion is formed at the two center convex points; and the second oblique shock wave is formed at the right end point of airfoil. Pressure and temperature increase after the shock wave and decrease after the expansion. Mach number is opposite.

Energy deposition added at the inflow boundary can be divided into three different types of filaments: infinitely long symmetric, symmetric pulsed, and asymmetric pulsed. In every type filament condition, there are four types of diameters for filament: $\frac{d}{t} = 0.10$, $\frac{d}{t} = 0.25$, $\frac{d}{t} = 0.50$, $\frac{d}{t} = 1.00$. The temperature of filament is higher than the upstream; Mach number is lower and pressure is the same. The filament can change the angle of shock wave and expansion; and the filament in the condition of the larger $\frac{d}{t}$ makes the more apparent of the angle change. For $M_f = 1.414$ (Mach number of the filament) and $\delta = 10^\circ$ (the half angle of the airfoil), an almost "normal shock" has formed near the leading edge of the diamond-shaped airfoil in the filament region. This is true for all four cases, but is apparent in the contours plots for the thicker filament only (the normal shock in the case with $\frac{d}{t} = 1.00$ is most apparent). Actually, the "normal shock" would be a detached shock, but appears to be "attached" shock due to the finite size of the grid cells. The streamwise distortion of the filament following the second shock is quite apparent. This is due to the variation in

arrival time of the front face of the filament at the shocks.

All types of the filaments (infinitely long symmetric, symmetric pulsed, asymmetric pulsed) would reduce the drag coefficient with the height of the filament increasing.

5.2 Future Work

Inviscid flow analysis neglects the effect of viscosity on the flow. The example for which an inviscid flow calculation is appropriate is an aerodynamic analysis of some high-speed projectile. In a case like this, the pressure forces (drag force) on the airfoil will dominate the viscous forces (like research work of Farzan [37] and Norton [38] [39]). Hence, an inviscid analysis will give a quick estimate of the primary forces acting on the body. So in the future work, a viscous analysis may be performed to include the effects of the fluid viscosity and turbulent viscosity on the lift and drag forces.

References

[1] Kremeyer, K., "Lines of Pulsed Energy for Supersonic/Hypersonic Drag Reduction: Generation and Implementation," *AIAA Paper No. 2004-984*, 2004.

[2] Georgievsky, P. Y. and Levin, V. A., "Bow Shock Wave Structures Control By Pulse-Periodic Energy Input," *AIAA Paper No. 2004-1019*, 2004.

[3] Lashkov, V. A., Mashek, I. C., Anisimov, Y. I., Ivanov, V. I., Kolesnichenko, Y. F., and Azarova, O. A., "Gas-dynamic Effects Around the Body Under Energy Deposition in Supersonic Flow," *AIAA Paper No. 2007-1231*, 2007.

[4] Lashkov, V. A., Mashek, I. C., Anisimov, Y. I., Ivanov V.I., Kolesnichenko, Y. F., and Rivkin, M. I., "Gas-dynamic peculiarities of microwave discharge interaction with shock wave near the body," *AIAA Paper No. 2008-1410*, 2008.

[5] Schülein, E., Zheltovodov, A. A., Loginov, M. S., and Pimonov, E. A., "Experimental and Numerical Study of Shock Wave Transformation by Laser-Induced Energy Deposition," *International Conference on Methods of Aerophysical Research*, ICMAR 2008.

[6] Knight, D., Lashko, V., and Mashek, I., "Interaction of Microwave-Generated Plasma with a Hemisphere Cylinder at Mach 2.1," *AIAA Journal*, Vol. 47, No. 12, December 2009.

[7] Mahapatra, D., Sriram, R., and Jagadeesh, G., "Shock Tunnel Studies on Drag Reduction of a Blunt Body Using Argon Plasmajet," *AIAA Paper No. 2009-1536*, 2009.

[8] Sasoh, A., Sekiya, Y., Sakai, T., Kim, J., and Matsuda, A., "Drag Reduction of Blunt Body in a Supersonic Flow with Laser Energy Depositions," *AIAA Paper No. 2009-1533*, 2009.

[9] Lazar, E., Elliott, G., and Glumac, N., "Microwave Generated Plasma for Active Flow Control in Aerodynamic Applications," *AIAA Paper No. 2008-1387*, 2008.

[10] Bletzinger, P., N, G. B., Wie, D. V., and Garscadden, A., "Plasmas in high speed aerodynamics," *Journal of Physics D: Applied Physics*, , No. 38, 2007, pp. R38–57.

[11] Wang, J., Y, L., Cheng, B., Su, C., Song, H., and Wu, Y., "Effects of plasma aerodynamic actuation on oblique shock wave in a cold supersonic flow," *Journal of Physics D: Applied Physics*, , No. 165503, 2009.

[12] Bushnell, D. M., "Shock Wave Drag Reduction," *Annu. Rev. Fluid Mech.*, 2004.

[13] Knight, D., Kolesnichenko, Y. F., Brovkin, V., and Khmara, D., "High Speed Flow Control Using Microwave Energy Deposition," *16th Australasian Fluid Mechanics Conference*, December 2007.

[14] Miles, R. B., "Flow Control by Energy Addition into High-Speed Air," *AIAA Paper No. 2000-2324*, 2000.

[15] Aradag, S., Yan, H., and Knight, D., "The Effects of Laser Energy Deposition on Supersonic Cavity Flow," *J. of Thermal Science and Technology*, 2009, pp. 67–73.

[16] Tretyakov, P. K., Kraynev, V. I., Yakovlev, V. I., Grachev, G. N., Ivanchenko, A. I., Ponomarenko, A. G., and Tischenko, V. N., "A Powerful Optical Pulsating Discharge as the Source of Energy Release in a Supersonic Flow," *Proc. International Conference on the Methods of Aerophysical Research*, , No. 2, August 1994, pp. 224–228.

[17] Brovkin, V. G., Kolesnichenko, Y. F., and Leonov, Y. F., "Study of Microwave Plasma-Body Interaction in Supersonic Airflow," *AIAA Paper No. 1999-3740*, 1999.

[18] Kolesnichenko, Y. and Brovkin, V., "Investigation of AD - Body Interaction with Microwave Discharge Region in Supersonic Flows," *AIAA Paper No. 2001-0345*, 2001.

[19] Adelgren, R., Elliott, G., Knight, D., Zheltovodov, A., and Beutner, T. J., "Energy Deposition in Supersonic Flows," *AIAA Paper No. 2001-0885*, 2001.

[20] Kolesnichenko, Y., Brovkin, V., Azarova, O., Grudnitsky, V., Lashkov, V., and Mashek, I., "Microwave Energy Release Regimes for Drag Reduction in Supersonic Flows," *AIAA Paper No. 2002-0353*, 2002.

[21] Kolesnichenko, Y., Azarova, O., Brovkin, V., Khmara, D., Lashkov, V. A., Mashek, I. C., and Rivkin, M., "Basics in Beamed MW Energy Deposition for Flow/Flight Control," *AIAA Paper No. 2004-0669*, 2004.

[22] Glumac, N., Elliott, G., and Boguszko, M., "Temporal and Spatial Evolution of the Thermal Structure of a Laser Spark in Air," *AIAA Paper No. 2005-204*, 2005.

[23] Mashek, I. C., Anisimov, Y. I., Lashkov, V. A., and Kolesnichenko, F. Y., "MW Discharge Initiated by Laser Spark," *AIAA Paper No. 2004-0358*, 2004.

[24] Satheesh, K. and Jagadeesh, G., "Effect of concentrated energy deposition on the aerodynamic drag of a blunt body in hypersonic flow," *Physics of Fluids 19*, 2007.

[25] Kremeyer, K., Sebastian, K., and Shu, C., "Computational Study of Shock Mitigation and Drag Reduction by Pulsed Energy Lines," *AIAA Journal*, Vol. 44, No. 8, August 2006.

[26] Zheltovodov, A. A., Pimonov, E. A., and Knight, D. D., "Energy Deposition Influence on Supersonic Flow over Axisymmetric Bodies," *AIAA Paper No. 2007-1230*, 2007.

[27] Georgievsky, P. Y. and Levin, V. A., "Stability Problem for Front Separation Regions Control Realized by Energy Deposition," *AIAA Paper No. 2006-402*, 2006.

[28] Georgievsky, Y. P. and Levin, V. A., "Instability of Front Separation Regions Initiated by Energy Deposition of Various Geometrical Configurations," *AIAA Paper No. 2009-1223*, 2009.

[29] Ardelyan, N. V., Bychkov, V. L., Kosmachevskii, K. V., and Malmuth, N. D., "Hot filaments for plasma aerodynamic applications," *AIAA Paper No. 2007-1233*, 2007.

[30] Yan, H. and Gaitonde, D., "Control of Edney IV Interaction by Energy Pulse," *AIAA Paper No. 2006-562*, 2006.

[31] Bityurin, V. A., Bocharov, A. N., and Popov, N. A., "Direct Current Discharge in Supersonic Flow," *AIAA Paper No. 2008-1385*, 2008.

[32] Knight, D., Azarova, O., and Kolesnichenko, Y., "On Details of Flow Control via Characteristics and Location of Microwave Filament During Its Interaction with Supersonic Blunt Body," *AIAA Paper No. 2009-847*, 2009.

[33] Knight, D. D., *Elements of Numerical Methods for Compressible Flows*, Cambridge University Press, 2006.

[34] *FLUENT help 6.3 Documentation (file:///usr/local/Fluent.Inc/fluent6.3.26/help/index.htm)*.

[35] Knight, D. D., *Inviscid Compressible Flow*, CRC Press, 1998.

[36] John, J., *Gas Dynamics Physics*, Allyn and Bacon, Inc, 2nd ed., 1984.

[37] Farzan, F. and Knight, D., "Interaction of Microwave Filament and Blunt Body in Supersonic Flows," *AIAA Paper No. 2008-1356*, 2008.

[38] Norton, K. and Knight, D., "Thermal Effects of Microwave Energy Deposition In Supersonic Flow," *AIAA Paper No. 2009-1224*, 2009.

[39] Anderson, K. and Knight, D., "Interaction of Heated Filaments with a Blunt Cylinder in Supersonic Flow," *AIAA Paper No. 2010-1381*, 2010.